Lagrangian Methods for Inviscid Barotropic Flow

Higher-Order Mimetic Discretization on a Space-Time Grid

Mukthesh Mahadev

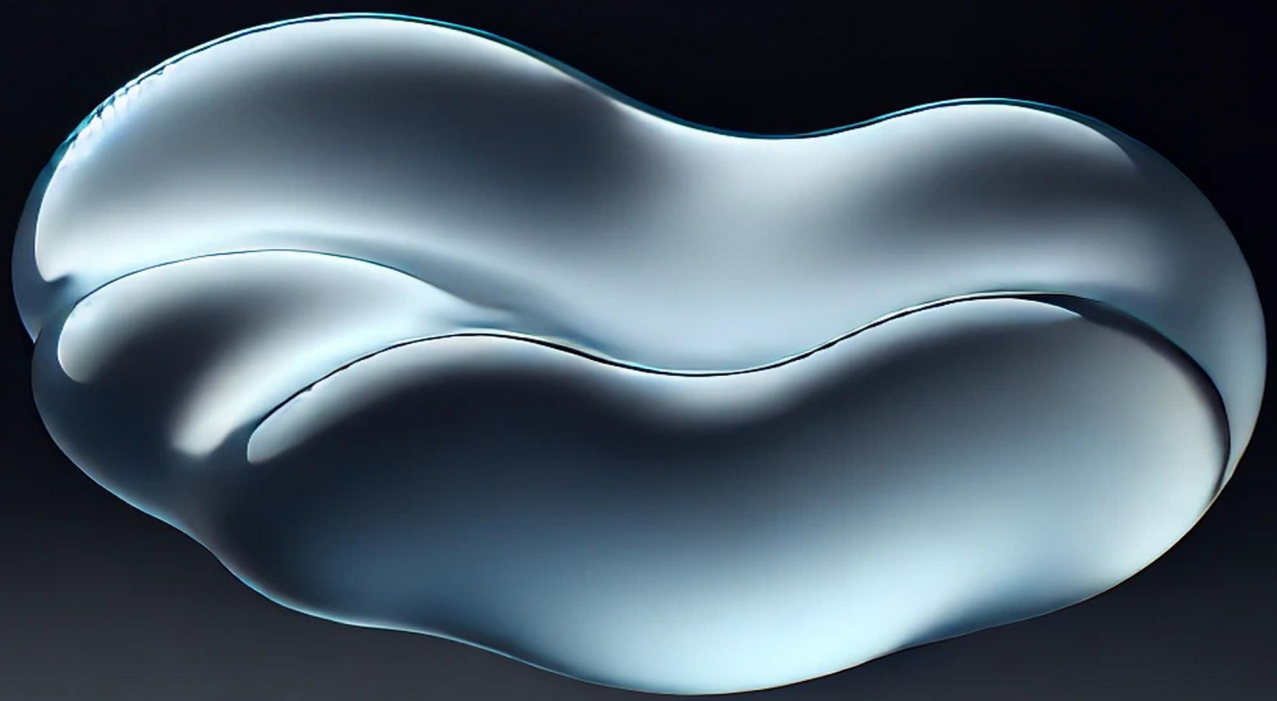

TU Delft

Lagrangian Methods for Inviscid Barotropic Flow

Higher-Order Mimetic Discretization on a Space-Time Grid

by

Mukthesh Mahadev

to obtain the degree of Master of Science

in Aerospace Engineering at the Delft University of Technology,

to be defended publicly on Monday the 31st of March, 2025 at 11:00 AM.

Student number: 5805120

Project duration: 1st May 2024 - 4th March 2025

Thesis committee:

Dr.ir. M.I. Gerritsma	Supervisor	TU Delft-Faculty of Aerospace Engineering
Ir. S. Shreshta	Supervisor	TU Delft-Faculty of Aerospace Engineering
Dr.ir. A.H. (Alexander) van Zuijlen	Chair	TU Delft-Faculty of Aerospace Engineering
Dr. A. (Artur) Palha da Silva Clérigo	Examiner	TU Delft-EEMCS, Applied Mathematics
Dr. N. Valle Marchante	Additional	TU Delft-Faculty of Mechanical Engineering

cover: Created with the assistance of DALL·E 2

TU Delft

Preface

Before I begin my exposition on the work I have been conducting over the past nine months, I would like to express my heartfelt gratitude to those who have guided, supported, and encouraged me during this journey. First and foremost, I want to thank my supervisor, Dr.ir. M.I.Gerritsma, for his unwavering support and guidance throughout my research. He generously made time to meet with me, and our discussions were both intellectually stimulating and lighthearted, featured by his witty jokes that never failed to brighten our meetings. I am also deeply appreciative of my co-supervisor, Suyash Shrestha, whose insightful feedback and suggestions were invaluable in helping me refine my research. Finally, to my family and friends: your unwavering support kept me fueled throughout this demanding journey. Thank you for being my sounding board and occasional reality-checkers. This work wouldn't have been possible without you.

Mukthesh Mahadev
Delft, March 2025

Abstract

This study proposes a novel approach, developing and analyzing a higher-order, structure-preserving discretization method for inviscid barotropic flows from a Lagrangian perspective. The discretization encodes flow variables as discrete differential forms on a space-time mesh, using principles from differential geometry and algebraic topology.

Unlike standard Lagrangian methods, which are prone to mesh distortion, this framework computes fluid deformations in a reference configuration and systematically maps them to the physical domain. This structure-preserving design ensures that fundamental conservation laws for mass, momentum, and energy hold up to machine precision. It also efficiently handles low-Mach number flows without specialized fixes for stiff pressure waves.

Numerical experiments on expansion and compression flows confirm the discretization's accuracy, stability, and conservation properties. The formulation naturally couples with structural solvers, enabling fluid-structure interaction and other multi-physics applications. By uniting spectral accuracy with a geometry-aware design, this approach serves as a first step toward a complete Lagrangian spectral element solver.

Contents

Nomenclature

Abbreviations

Abbreviation	Definition
FE	Finite Element
PDE	Partial Differential Equation
Hodge $\star$	Hodge Star Operator
TM	Tangent Bundle
T*M	Cotangent Bundle
SEM	Spectral Element Method
GLL	Gauss-Lobatto-Legendre
DOF	Degrees of Freedom
LBM	Lagrangian Barotropic Model

Symbols

Symbol	Definition	Unit
M	Manifold	-
T_pM	Tangent Space at point p	-
T_p^*M	Cotangent Space at point p	-
X_p	Tangent Vector at point p	-
d	Exterior Derivative	-
ω	Differential Form	-
$\star$	Hodge Star Operator	-
$\wedge$	Wedge Product	-
∇	Gradient Operator	-
$\nabla\times$	Curl Operator	-
$\nabla\cdot$	Divergence Operator	-
$\mathbb{E}$	Incidence Matrix for Discrete Exterior Derivative	-
$\mathbb{M}$ / $\mathbb{H}$	Discrete Hodge (Mass Matrix)	-
$\mathbb{N}$	Boundary Inclusion Matrix	-
ξ	Gauss-Lobatto-Legendre Nodes	-
$h_i(\xi)$	Nodal Lagrange Basis Function	-
$e_i(\xi)$	Edge Basis Function	-
$\tilde{h}(\xi)$	Dual Nodal Basis Function	-
$\tilde{e}(\xi)$	Dual Edge Basis Function	-
φ	Flow Map	-
$\boldsymbol{F}$	Deformation Gradient Tensor	-
J	Jacobian Determinant of Flow Configuration	-
P_W	Material Pressure	bar
Π	Potential Energy	kJ
$\boldsymbol{P}$	First Piola-Kirchhoff Stress Tensor	-
U	Internal Energy	-
ρ_o	Reference Density	[kg/m^3]
ρ	Fluid Density	[kg/m^3]
$\boldsymbol{T}$	Cauchy Stress Tensor	-
$\boldsymbol{\pi}$	Canonical Momentum Density	-
$\mathcal{L}$	Lagrangian Density	kJ/m^3
$\mathcal{H}$	Hamiltonian Density	kJ/m^3
$\mathcal{A}$	Action Functional	-
$\mathbb{E}^{1,0}$	Gradient Operator Matrix	-
$\mathbb{H}_{P_w}$	Pressure Hodge Matrix	-
$\mathbb{H}_{\rho_o}$	Density Hodge Matrix	-
$\mathbb{N}_\pi$	Connectivity Matrix for Momentum	-

1

Introduction

In modern computational fluid dynamics (CFD), significant effort has been devoted to the development of numerical methods that accurately represent the underlying physics of fluid flow while preserving crucial conservation properties. Many approaches excel at matching experimental data for specific test cases yet may struggle to conserve invariants such as energy, momentum, or mass when integrated over long time intervals. Consequently, there is a growing interest in *structure-preserving* numerical frameworks that capture both the geometric and variational foundations of fluid behavior. These frameworks are particularly relevant for flows governed by variational or Hamiltonian principles, where numerical errors can accumulate and degrade the fidelity of simulations if the discrete scheme fails to respect the inherent symplectic or multisymplectic nature of the governing equations.

One class of flows that benefits substantially from structure-preserving approaches is *inviscid barotropic flow*, where pressure depends solely on fluid density. This type of flow arises in many geophysical, aerospace, and industrial contexts, often involving compressible fluids under conditions in which thermal gradients have a reduced or secondary influence. By describing the flow in a *Lagrangian viewpoint/perspective* , it becomes possible to track individual fluid parcels through space and time, rather than examining velocities at fixed points in a spatial domain. The Lagrangian formulation offers several advantages:

1. **Natural Material Tracking.** Tracking fluid particles makes it straightforward to account for moving interfaces, free surfaces, or deforming fluid domains.
2. **Variational Clarity.** The Lagrangian description defined through a variational formulation simplifies the presentation of symplectic or multisymplectic structures, ensuring that physical invariants can be identified and systematically preserved in the discrete formulation.
3. **Streamlined Coupling with Other Physics.** Many structural and solid mechanics solvers use a Lagrangian description to follow material points. As a result, a Lagrangian fluid solver naturally facilitates *fluid–structure interaction (FSI)* by aligning coordinate systems, thereby simplifying the interface treatment and promoting consistent momentum and energy exchange. This property also benefits more general *multi-physics* scenarios, including magnetohydrodynamics or reactive flows, in which a unified variational foundation can enhance numerical stability and physical fidelity.

Despite these advantages, purely Lagrangian methods typically involve a computational mesh that deforms with the fluid parcels in physical space, leading to potential mesh distortion and numerical instability. In contrast, the approach presented in this work employs a novel strategy: fluid variables are associated with the physical (deformed) configuration are evaluated in the *reference configuration* thus avoiding mesh deformations. Central to this strategy is the *first Piola–Kirchhoff tensor*, which describes how fluid stresses or fluxes computed in the reference space map to the current physical space. This technique mitigates some of the issues encountered by standard moving-mesh approaches in CFD and draws inspiration from solid mechanics, where a similar mapping has been used to connect reference and deformed domains.

Another significant challenge addressed in this work relates to the behavior of *Low-Mach-number* compressible flows (where $M \ll 1$) pose significant computational challenges because the governing equations become stiff and ill-conditioned as the flow speed is much smaller than the speed of sound [6, 11]. Physically, acoustic waves travel at

high speeds relative to the low flow velocity, forcing very small time steps when explicit time-integration methods are used [10]. At the same time, density variations are weak, making the system nearly incompressible and prone to numerical inaccuracies [3]. These difficulties can cause either excessive numerical dissipation or very high computational cost due to the disparity in characteristic speeds. By leveraging the Lagrangian formulation in a variational setting, the approach introduced here handles low-Mach regimes *naturally*, without the need to incorporate additional preconditioning or sound-speed modifications. This characteristic further underscores the versatility and robustness of the proposed scheme.

Recent progress in *multisymplectic* and *mimetic* (also known as *compatible*) numerical methods suggests that long-standing issues of instability can be mitigated [38, 41]. Multisymplectic formulations extend symplectic integrators originally designed for time integration into the space-time domain, ensuring that essential phase-space structures are respected throughout both temporal and spatial dimensions. Meanwhile, mimetic approaches leverage concepts from differential geometry and algebraic topology to replicate the fundamental identities of vector calculus on discrete grids. These techniques provide discrete analogs of divergence, curl, and gradient operators that rigorously satisfy their associated identities, thereby yielding conservation properties that mirror those in the continuous theory.

The present study constitutes a *first step* toward a full fledged *spectral element solver* designed for barotropic flows under a Lagrangian, multisymplectic framework. Higher-order spectral frameworks are known for superior convergence and accuracy when the solution is sufficiently smooth, while mimetic principles ensure that essential geometric and topological features of the flow are preserved. In addition to laying the theoretical groundwork, this investigation demonstrates that the methodology can be extended to incorporate *pressure boundary or free boundary conditions*. The resulting solver not only maintains discrete analogs of key conservation laws such as linear momentum, angular momentum, energy, and mass but also holds potential for unification with Lagrangian solid mechanics or related physics modules. This unified viewpoint simplifies *fluid–structure interaction (FSI)* by sharing a common Lagrangian description, reducing interface complexity, and improving the consistency of momentum and energy transfer across the fluid-solid boundary.

1.1. Research Question

Against this backdrop, a central question emerges:

> ***Can the inviscid barotropic flow, formulated in the Lagrangian framework via a multisymplectic variational principle, be discretized with a space-time numerical method in a higher-order mimetic setting?***

To investigate the main question, several more specific points are addressed:

1. Does the proposed method correctly handle pressure and free boundary conditions, and does it converge to a limit deformation as the polynomial order is increased?
2. Does the discrete scheme preserve the symmetries associated with the multisymplectic formulation specifically the conservation of linear momentum, angular momentum, energy, and mass?

These sub-questions provide a clear roadmap for assessing whether the methodology lives up to the theoretical promise of unified structure preservation and high accuracy.

1.2. Thesis Outline

The remainder of this thesis is structured as follows:

Chapter 2 – Introduction to Mimetic Discretisation: Presents the theoretical foundation of mimetic or compatible methods, focusing on how physical variables can be assigned to different geometric entities. Emphasis is placed on preserving topological relationships in the discrete context and ensuring that discrete versions of divergence, curl, and gradient remain exact.

Chapter 3 – Mathematical Framework into Mimetic Methods: Introduces the relevant concepts from differential geometry and algebraic topology. Manifolds, differential forms, exterior derivatives, and the Hodge $*$ operator are explained, with attention to how these ideas underpin the structure-preserving goals of the numerical formulation.

Chapter 4 – Discrete Setting and Spectral Implementation: Describes how to translate continuous geometric and topological concepts into a fully discrete environment using higher-order spectral elements. Topics include Gauss–Lobatto–Legendre (GLL) nodes, nodal and edge polynomial basis functions, primal and dual variables, incidence matrices, and discrete Hodge star operators.

Chapter 5 – Lagrangian Formulation of Barotropic Flow: Details the derivation of the governing equations under a Lagrangian perspective via a Lagrangian variational formulation , including the barotropic assumption and the fundamental multisymplectic structure. The influence of Noether's theorem on discrete conservation laws is addressed.

Chapter 6 – Weak Formulation and the Full Discrete System: Develops a weak (variational) form of the equations, treating both spatial and temporal discretizations in an integrated manner. This chapter also covers the discrete enforcement of pressure boundary conditions, as well as the computational implementation of the nonlinear pressure term.

Chapter 7 – Numerical Experiments and Results: Presents numerical experiments designed to assess performance under different pressure boundary conditions. Convergence behavior is examined as the polynomial order increases, and key conservation properties (mass, momentum, and energy) are evaluated to determine whether the discrete scheme preserves the multisymplectic symmetries introduced in earlier chapters.

Chapter 8 – Conclusion and Future Work: Summarizes the principal findings regarding convergence, boundary-condition handling, and discrete symmetry preservation. Further applications are proposed, including *fluid–structure interaction (FSI)* and other multi-physics extensions, highlighting how the Lagrangian perspective naturally aligns with standard structural mechanics codes and can unify diverse physical phenomena within a single computational framework.

1.3.Contributions

The contributions of this research can be summarized as follows:

1. **Framework Definition:** Establishment of a higher-order mimetic scheme for inviscid barotropic flow in a Lagrangian, multisymplectic context, forming a solid foundation for a future full spectral element solver.
2. **Boundary Condition Treatment and Convergence:** Demonstration that pressure boundaries can be handled effectively while maintaining accuracy and stability, and verification of convergence behavior as polynomial order increases.
3. **Low-Mach-Number simulations:** Inclusion of a formulation that captures low-Mach-number compressible flows *naturally*, avoiding the need for specialized preconditioning, artificial sound-speed manipulation, or acoustic filtering, thus enhancing computational efficiency and numerical stability.
4. **Symmetry and Conservation:** Validation that the discrete system preserves important conservation properties — namely, linear momentum, angular momentum, energy, and mass—by leveraging multisymplectic and mimetic principles.
5. **Pathway to Multi-Physics:** Provision of a formulation that can integrate fluid flow with structural mechanics or other physics, facilitating fluid–structure interaction in a common Lagrangian framework and ensuring consistent conservation across coupled domains.

In summary, this investigation seeks to unify higher-order structure-preserving algorithms, and the advantages of a Lagrangian description, thereby laying groundwork for advanced CFD capabilities that can seamlessly interface with solid mechanics solvers and handle low mach number compressible flows. Such a cohesive methodology aims to address the rising demand for *geometry-aware* simulations of both single-physics and multi-physics processes in modern engineering and scientific research.

2

Introduction to Mimetic Discretisation

2.1.Geometric structure of Physics

Continuum physics revolves around observable quantities such as displacement, velocity, etc. We explore how these quantities interact over space and time to understand physical phenomena. In the framework of vector calculus, these variables are classified as scalars or vectors, but this classification can be misleadingly simple. Consider scalar quantities as an example. A scalar potential $\phi(x, y, z)$ is defined at each point in the space, which means it directly represents a value at that point. A similar distinction appears in vector fields; a velocity field $\mathbf{u}(x, y, z)$ may be traced along paths or contours, while a flux (i.e. $\boldsymbol{u}.\boldsymbol{n}\, dA$) is more naturally defined across an area or surface. These examples show that standard vector calculus does not always capture the subtle geometric contexts in which these quantities appear in continuum physics.

Tonti [34] argues that describing physical quantities as field variables often obscures their geometric nature, especially when using differential formulations derived through limiting processes. For instance as shown in [30], consider the example of conservation of mass, which states that the total mass within a fixed volume V is given by, $\int_V \rho\, dV$. Thus according to the conservation principle, any change in the total mass inside V results from the net flux of mass across its boundary ∂V:

$$\int_V \rho(t + \Delta t)\, dV - \int_V \rho(t)\, dV + \Delta t \int_{\partial V} \rho \mathbf{u} \cdot \mathbf{n}\, dS = 0.$$

Dividing by Δt and letting $\Delta t \to 0$, and then applying the divergence theorem converts the surface integral to a volume integral:

$$\int_V \frac{\partial \rho}{\partial t}\, dV + \int_V \nabla \cdot (\rho \mathbf{u})\, dV = 0.$$

Since this equation holds for any arbitrary volume V, the differential form of the mass conservation law becomes:

$$\frac{\partial \rho}{\partial t} + \nabla \cdot (\rho \mathbf{u}) = 0.$$

Now, the sense of volume associated to the density in it's integral formulation is lost when the differential formulation is obtained following the process of taking a limit. This example highlights that, original geometric interpretation can be lost in the process of transformation from, the integral to the differential form.

Continuing from Tonti's [34] discussion, it is evident that transitioning from integral to differential forms of physical laws involves an abstraction that can hide the original geometric meaning of the quantities involved. The process of taking limits, as seen in the derivation of differential forms of equations, is a mental construct that introduces a level of idealization beyond what can be achieved in practice. The notion of a limit is central to calculus, defining concepts like instantaneous velocity or point-wise density. However, in the physical world, quantities are measured with finite precision. Measurement tools record data in discrete steps and within specific error margins, so the precision suggested by mathematical limits is simply not achievable. By applying a limit, we smooth over the naturally steplike nature of real-world data, giving an illusion of continuity that does not reflect actual observations.

Computers, limited by finite arithmetic precision , cannot handle true infinitesimal quantities or exact limits, relying instead on approximations, which replace derivatives with discrete changes and integrals with summations over small elements. This reveals that computational physics is inherently discrete, making it more natural to formulate problems using global variables like total mass, or displacement, which relate to extended spatial or temporal regions and are directly measured in experiments without involving limits instead of field variables employed in conventional vector calculus. These global variables retain geometric and topological information that differential formulations often conceal. They also provide an algebraic structure well-suited for numerical methods, which align with the discrete nature of physical measurements by operating on finite regions such as mesh cells.

2.2.Global Variables and Their Geometric Association

The previous section highlighted while differential equations describe local, pointwise relationships, many physical quantities are naturally measured over finite domains of space and time. We call these global variables: total mass, flux through a surface, circulation along a path, etc. Such variables emphasize the geometry of the region or boundary under consideration, aligning with geometric construction of physical laws. Instead of deriving densities or rates by taking limits, we work directly with what is measured in practice: averages, totals, or net transfers over finite, oriented 'chunks' of space and time.

Each global variable naturally attaches to a geometric entity of specific dimension:

- A **0-dimensional** entity is a point P. Certain global scalars, such as position or temperature, are measured at points.
- A **1-dimensional** entity is a line L. Circulation of a velocity field and total displacement are typical examples.
- A **2-dimensional** entity is a surface S. Heat flux and mass flux are all measured *across* surfaces.
- A **3-dimensional** entity is a volume V. Quantities such as total mass and change in energy are measured over volumetric regions.

Similarly in time, measurement is over intervals T (1-dimensional time element) or at discrete instants I (0-dimensional time element).

2.2.1. Classification of Global Variables

A concise way to organize physical variables, following Tonti [34], is to classify them as *configuration*, *source*, or *intermediate*. Configuration variables describe the geometry or arrangement of the system (e.g., displacement fields, electromagnetic potentials), while source variables capture external stimuli (e.g., forces, charges). Intermediate variables bridge these two categories and often appear in tensorial pairs, such as stress–strain or electric–magnetic fields, reflecting how the system responds to external inputs.

From this classification emerge three key types of governing equations. **Definition equations** express intermediate variables as derivatives of configuration variables, for example strain defined by the gradient of displacement . **Balance equations** relate source variables to intermediate variables via fluxes or divergences, as in the continuity equation for mass. Finally, **constitutive equations** tie pairs of intermediate variables together or link them to source variables using material properties (e.g., stress–strain laws in elasticity or electric displacement–field relationships in electromagnetism).

This viewpoint preserves the geometric and causal structure of physical models, aligning naturally with integral (global) forms that measure finite regions or boundaries rather than relying solely on differential (pointwise) formulations.

2.3.Orientations and Its Necessity

A critical subtlety in describing many physical laws is the **orientation** of the geometric element on which a variable is measured. Each dimension—point (0D), line (1D), surface (2D), volume (3D)—can carry two distinct kinds of orientation:

1. *Inner orientation* :

   Inner orientation refers to orientation within the geometric element. For a 1D line element (edge) in space, an inner orientation indicates the 'forward' direction of the line. For a 2D surface element (face), an inner orientation selects a consistently oriented boundary direction according to the right-hand rule or similar. For a 3D volume element (cell), an inner orientation is typically the orientation that ensures a consistent boundary orientation for its enclosing faces. Physically, variables that require an *inner* orientation are often *configuration* variables.

2. *Outer orientation* :

   Outer orientation refers to orientation around the geometric element. A line with outer orientation may be used in measuring, for instance, a boundary trace of flux. A surface with an outer orientation is usually the standard flux orientation, where the vector normal points outward and a volume with outer orientation is used in measuring divergence within the volume. Variables that need an *outer* orientation are often *source* variables (like forces, fluxes, or intensities).

Though [34] recommends to follow these associations, there is no rule that relates configuration variables to inner orientation and the source variables to outer orientation as long as the made associations are consistently respected throughout the entire formulation. The geometric notion of orientation is what permits us to define consistent signs for physical quantities. If we were to ignore or mix up orientations, we would lose the ability to state the direction of flow, net in/out flux, and other essential physical details. Consider a simple flux balance in fluid mechanics $\int_{\partial V} \mathbf{f} \cdot \mathbf{n}\, dS$, where $\mathbf{f}$ is a flux vector (mass flux etc.) and $\mathbf{n}$ is the unit normal. The overall sign of this integral depends crucially on the *outer* orientation of the surface ∂V. Reversing the orientation (inward vs. outward) changes the sign of the result and hence changes the interpretation from *outflow* to *inflow*. All such fundamental constructs of continuum physics rely on orientation to define directionality unambiguously. Figure 2.1 shows the associated inner and outer orientation of geometric objects in $\mathbb{R}^3$.

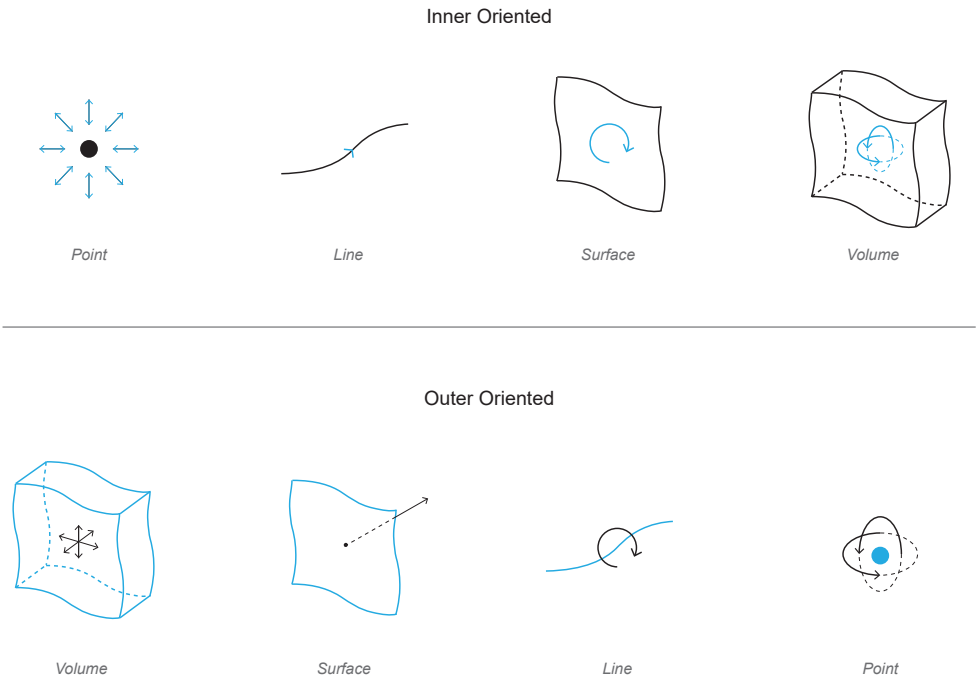

Figure 2.1: Inner and Outer orientations of geometric objects

2.4.Linking to Differential Geometry and Algebraic Topology

Differential geometry and algebraic topology offer powerful, coordinate-free tools to connect these global, integral perspectives with local, pointwise formulations. By emphasizing orientation, connectivity, and discrete cell complexes, they unify physical measurements with the underlying geometric and topological structure of space, ensuring that both integral and differential forms of the laws remain consistent and transparent.

2.4.1. From Global to Local: The Role of Differential Geometry

When finite regions shrink to infinitesimal size when the limiting process occurs in classical vector calculus, it is marked by the appearance of operators $\nabla\cdot$, $\nabla\times$, and ∇. In the language of differential geometry, the same process corresponds to taking the *exterior derivative* of differential forms. Concretely, a 0-form (function) (evaluated at points) becomes a 1-form upon applying d, thereby measuring variations along one-dimensional lines. Similarly, a 1-form (integrated along lines) produces a 2-form that can be integrated over surfaces, and so forth.

2.4.2. From Global to Discrete: The Role of Algebraic Topology

Numerical methods do not employ true differentials or infinitely refined partitions. Instead, space and time are discretized into cell complexes:

- A **primal** complex (points, edges, faces, volumes) with a particular orientation *inner* or *outer* depending on the choice of discretisation.
- A **dual** complex with a complementary orientation to the primal complex, offset so that each dual cell intersects the corresponding primal cell of complementary dimension.

In *algebraic topology*, these discrete elements (0-cells, 1-cells, 2-cells, 3-cells) are the basic building blocks for *global* variables. Approaches such as *mimetic* or *compatible* discretizations [20, 23] implement:

- **Chains**: formal sums of oriented cells.
- **Cochains**: assignments of values (the global quantities) to those oriented cells.

The *coboundary* operator is then the discrete analog of the exterior derivative, encoding how values on boundaries and interiors must relate—thus mirroring classical relations involving $\nabla\cdot$, $\nabla\times$, and ∇.

From this algebraic-topological perspective, one can:

1. Directly form a **discrete** (algebraic) system suitable for computations .
2. Recover the usual **differential** forms by letting the cells shrink to zero size and assuming sufficient smoothness in the underlying fields.

This chapter outlined the geometric and topological concepts that connect to continuum physics, stating the importance of global variables, orientations, and how they connect to local, differential representations. These insights form the motivation of *mimetic discretisation* techniques, which aim to preserve physical and geometric properties within numerical computations.

The next chapter will present a more formal introduction to differential geometry and algebraic topology. These mathematical frameworks offer a systematic way to handle orientations, boundaries, and connectivity, forming a foundation for the development of mimetic discretisation methods.

3

Mathematical Framework Into Mimetic Methods

This chapter presents foundational concepts from differential geometry and algebraic topology that serve as the skeleton for mimetic discretization methods. It begins by defining manifolds and discussing tangent and dual spaces, then introduces differential forms along with the principal metric-independent operators acting on them—the exterior derivative and the generalized Stokes theorem. The discussion continues with the inner product, the Hodge star operator, and the structure of de Rham complexes, concluding with an overview of how algebraic topology bridges these continuous concepts to discrete meshes in numerical methods

3.1.Manifolds

A *manifold* is a space that ”locally” looks like a subset of Euclidean space. Formally, as mentioned in [9] an n-dimensional manifold M consists of a topological space together with a collection of coordinate maps $\varphi_U : U \to \mathbb{R}^n$, each defined on an open neighbourhood $U \subset M$. These maps must cover M (i.e., every point in M is contained in at least one such neighbourhood), and their images in $\mathbb{R}^n$ are open sets.

This local resemblance allows one to define differentiability and integration in a manner analogous to that on $\mathbb{R}^n$ without necessitating a global metric. As [27] emphasizes, this ”coordinate-free” approach is particularly well-suited for formulating physical laws in a geometric framework where quantities are naturally associated with geometric objects rather than with a predefined co-ordinate system.

3.2.Tangent Vector Spaces and Dual Spaces

A fundamental concept in differential geometry is that each point p on a smooth manifold M admits a *tangent space* T_pM. Intuitively, T_pM captures all possible ”directions” in which one can move from p. Formally, a tangent vector is a *derivation* at p: a linear operator on the space of smooth real-valued functions near p that satisfies the Leibniz rule. In local coordinates $\{x^1, x^2, \ldots, x^n\}$, a tangent vector $X_p \in T_pM$ often appears as

$$X_p(f) \;=\; \sum_{j=1}^{n} X^j \left.\frac{\partial f}{\partial x^j}\right|_p , \tag{3.1}$$

where f is a smooth function defined at p, the coefficients X^j determine the vector’s components, and $\left.\frac{\partial}{\partial x^j}\right|_p$ form a basis of T_pM. In physical applications, such a vector can model a velocity, displacement, or any quantity that has a direction and magnitude.

The *dual space* at p, denoted T_p^*M, is the space of all linear functionals that act on T_pM. Elements of T_p^*M are

called *covectors* or *1-forms*. In local coordinates, a covector $\alpha \in T_p^*M$ can be expressed as

$$\alpha \;=\; \sum_{i=1}^{n} \alpha_i \, dx^i,$$

where $\{dx^i\}$ is the dual basis satisfying

$$dx^i\Big(\tfrac{\partial}{\partial x^j}\Big) \;=\; \delta^i_j.$$

Accordingly, when a covector α acts on a vector X,

$$\alpha(X) \;=\; \sum_{i=1}^{n} \alpha_i \, X^i, \tag{3.2}$$

giving a real number. Notably, vectors and covectors follow different transformation rules under a change of coordinates: vectors transform *contravariantly*, whereas covectors transform *covariantly*. This distinction underlies many physical interpretations, such as velocity (vector) versus gradient or force (covector), and ensures that their pairing remains a well-defined scalar.

3.2.1. Vector Bundles and Bundle-Valued Forms

From a global perspective, one collects all tangent spaces T_pM into the *tangent bundle* TM. Likewise, all dual spaces T_p^*M form the *cotangent bundle* T^*M. A *vector bundle* is, in general, any smooth family of vector spaces (one for each point $p \in M$) that "fit together" coherently over M. A *section* of a vector bundle picks out one vector from each fibre, so a classical *vector field* on M is precisely a section of TM.

When discretising a PDE it is advantageous to consider not just scalar-valued differential forms but also those taking values in a vector bundle (often the tangent or cotangent bundle). Such objects are known as *bundle-valued forms* [7, 27, 32]. Concretely, if ω is a k-form on M and $\mathcal{E}$ is a vector bundle over M, then a $\mathcal{E}$-valued k-form is a multilinear, antisymmetric map into $\mathcal{E}$ rather than into the real numbers.

Unified Representation. In two-dimensional (Cartesian) space, any vector- or covector-valued physical quantity has two components (one in the x-direction and another in the y-direction). Instead of treating these as separate scalar fields, a bundle-valued form stores both components together as a single mathematical entity, reflecting the intrinsic geometry.

Discrete Implementation. When discretizing vector or covector fields in finite element (FE) methods, one often places degrees of freedom (DoFs) on geometric entities (cells, edges, vertices) of a single mesh. Treating the field as a bundle-valued form naturally associates all vector components to the same mesh elements, simplifying both the assembly of system matrices and the enforcement of PDE constraints or boundary conditions.

3.3.Differential Forms: Concepts and Applications

Differential forms provide a robust framework for both the analysis and integration of functions on manifolds, extending classical calculus into a coordinate-free context. Formally a *differential k-form* on an n-dimensional manifold M is a multilinear, antisymmetric map that takes k tangent vectors and produces a real number $\omega : V^k \to \mathbb{R}$. In practical terms, a 0-form is simply a smooth function acting on real numbers, a 1-form is a linear functional on the tangent vector space, and higher-order forms can be expressed as the wedge (or exterior) product of 1-forms.

In local coordinates $(x^1, \ldots, x^n)$, a typical k-form ω is written as:

$$\omega = \sum_{i_1 < \cdots < i_k} f_{i_1 \ldots i_k}(x) \, dx^{i_1} \wedge \cdots \wedge dx^{i_k}, \tag{3.3}$$

where the functions $f_{i_1 \ldots i_k}$ are smooth on M. The wedge product $\wedge$ is central to the theory, it combines differential forms in a **bilinear**, **associative**, and **distributive** manner and if ω is a k-form and η is an l-form, then their product $\omega \wedge \eta$ is a $(k+l)$-form and satisfies the **skew-symmetry** property:

$$\omega \wedge \eta = (-1)^{kl}\, \eta \wedge \omega. \tag{3.4}$$

Extending these notions to *bundle-valued* differential forms allows one to handle objects whose components each behave like forms but collectively transform as sections of a vector bundle.

3.3.1. The Exterior Derivative

The *exterior derivative* extends the familiar concept of differentiation to differential forms. It is defined as a linear operator

$$d : \Lambda^k(M) \to \Lambda^{k+1}(M),$$

which increases the degree of a differential form by one. In local coordinates, the action of the exterior derivative is illustrated as follows:

- For a 0-form (a smooth function) f, the exterior derivative is given by

$$df = \sum_{j=1}^{n} \frac{\partial f}{\partial x^j}\, dx^j. \tag{3.5}$$

- For a 1-form $\alpha = \sum_i \alpha_i\, dx^i$, the exterior derivative is expressed as

$$d\alpha = \sum_{i,j} \frac{\partial \alpha_i}{\partial x^j}\, dx^j \wedge dx^i. \tag{3.6}$$

The operator d generalizes several well-known differential operators from vector calculus in Cartesian co-ordinates, when applied to a 0-form, d recovers the gradient, for a 1-form in three dimensions, d corresponds to the curl (or rotation in two dimensions) and when applied to a 2-form in three dimensions, d yields the divergence. A fundamental characteristic of the exterior derivative is its nilpotency:

$$d \circ d = 0. \tag{3.7}$$

This property underlies classical identities which are naturally encapsulated within the framework of differential forms, such as $\nabla \times (\nabla f) = 0$ and $\nabla \cdot (\nabla \times \mathbf{A}) = 0$.

3.3.2. Integration and Stokes' Theorem

Differential forms are ideally suited for integration over manifolds. If ω is an n-form defined on an n-dimensional oriented manifold M, then the integral

$$\int_M \omega \tag{3.8}$$

is well-defined and independent of the chosen coordinate system. This setting naturally leads to the *generalized Stokes theorem*:

$$\int_M d\omega = \int_{\partial M} \omega, \tag{3.9}$$

which unifies several classical results, including the Fundamental Theorem of Calculus, the Divergence Theorem, and the Kelvin–Stokes Theorem.

3.4.The Hodge $\star$ and Inner Product

3.4.1. Hodge $\star$ Operator

Let M be an n-dimensional oriented Riemannian manifold with volume form ω_n. The *Hodge $\star$ operator* is the linear mapping

$$\star : \Lambda^k(M) \longrightarrow \Lambda^{n-k}(M)$$

that assigns to each k-form its dual $(n-k)$-form. This duality is characterized by the relation

$$\eta \wedge \lambda = \langle \star\eta, \lambda \rangle \, \omega_n, \tag{3.10}$$

for all $\eta \in \Lambda^k(M)$ and $\lambda \in \Lambda^{n-k}(M)$, where $\langle \cdot, \cdot \rangle$ denotes the inner product on forms induced by the metric [9, 27].

In three-dimensional Euclidean space with standard coordinates (x^1, x^2, x^3), the Hodge $\star$ operates as follows:

- For a 0-form f:
$$\star f = f \, dx^1 \wedge dx^2 \wedge dx^3.$$
- For a 1-form:
$$\star dx^1 = dx^2 \wedge dx^3, \quad \star dx^2 = dx^3 \wedge dx^1, \quad \star dx^3 = dx^1 \wedge dx^2.$$
- For a 2-form:
$$\star(dx^2 \wedge dx^3) = dx^1, \quad \star(dx^3 \wedge dx^1) = dx^2, \quad \star(dx^1 \wedge dx^2) = dx^3.$$
- For the 3-form:
$$\star(dx^1 \wedge dx^2 \wedge dx^3) = 1.$$

These examples illustrate the one-to-one correspondence between k-forms and $(n-k)$-forms in $\mathbb{R}^n$, consistent with the combinatorial fact that the number of basis elements is given by $\binom{n}{k} = \binom{n}{n-k}$. An important property of the Hodge $\star$ operator is its behavior under successive application:

$$\star\star \, \alpha^{(k)} = (-1)^{k(n-k)} \alpha^{(k)}, \quad \forall \alpha^{(k)} \in \Lambda^k(M). \tag{3.11}$$

Unlike the exterior derivative, which is a topological operator, the Hodge $\star$ is **metric dependent**. The metric enters through the definition of the volume form ω_n and the inner product on forms.

Geometrically, the Hodge $\star$ relates the orientations of differential forms. In $\mathbb{R}^3$, a 1-form (a covector) is dual to a 2-form representing an oriented area, which in turn corresponds to the normal direction of the plane [37]. More generally, Hodge duality encapsulates the idea that a k-dimensional volume can be described equivalently by its complementary $(n-k)$-dimensional structure. That is, the Hodge $\star$ operator encodes the distinction between *inner* and *outer* orientations. As discussed by Mattiussi [14] and Bossavit [15], this distinction plays a crucial role in mimetic discretization methods, where computational models aim to preserve underlying geometric structures without introducing spurious numerical artifacts. In the previous chapter, configuration and source variables were introduced, along with three types of equations arising from them—balance laws, constitutive relations, and compatibility conditions. The Hodge $\star$ operator the conversion between these variables by mapping differential forms from the configuration space into their dual source space, thereby incorporating metric information into the formulation.

3.4.2. Inner Product on k-Forms

The inner product on the space of k-forms is closely connected with the Hodge $\star$ operator. For two k-forms $a, b \in \Lambda^k(M)$, one common definition is to require that

$$a \wedge \star b = \langle a, b \rangle \, \omega_n, \tag{3.12}$$

where ω_n denotes the volume form on M. In local orthonormal coordinates, the inner product reduces to the familiar Euclidean form:

$$\langle a, b \rangle = \sum_i a_i b_i.$$

Further in the forthcoming sections, it can be seen this relation plays a crucial role in the derivation of weak formulations. When one takes the inner product of a differential equation with a test function and integrates over the domain, the resulting volume form naturally fits under the integral sign, ensuring that the geometric structure is preserved. This property also uniquely determines the wedge product on the space of k-forms. Although this approach is somewhat abstract, it highlights the geometric significance of the wedge product. For example, consider the case of vectors in $\mathbb{R}^3$. If u and v are vectors with corresponding 1-forms $u^\flat$ and $v^\flat$, then the Euclidean inner product can be expressed via differential forms as

$$u \cdot v = \star\big(u^\flat \wedge \star v^\flat\big),$$

and the familiar cross product is given by

$$u \times v = \star\big(u^\flat \wedge v^\flat\big).$$

These identities reflect the geometric interpretation of the Hodge star: it converts a 1-form into a form whose wedge product with another 1-form creates a volume element, thus encoding the notion of perpendicularity and area.

3.5.De Rham Complexes

The de Rham complex unifies differential forms of varying degrees via the exterior derivative, providing a natural framework for many geometric and physical phenomena. It underpins de Rham cohomology, which characterizes the topological properties of manifolds.

Concretely, the exterior derivative d maps a k-form to a $(k+1)$-form and satisfies $d \circ d = 0$. This implies that the range of d always lies in the null space (kernel) of the subsequent d. On contractible domains (those without “holes”) the range of d *exactly* matches the null space, making the complex exact. In domains with non trivial topology, however, the range of d is only a subspace of the null space of the next d.

$$\mathbb{R} \longrightarrow \Lambda^0(M) \xrightarrow{d} \Lambda^1(M) \xrightarrow{d} \Lambda^2(M) \xrightarrow{d} \Lambda^3(M) \longrightarrow 0.$$

Further by incorporating the Hodge $\star$ operator—which maps a k-form to an $(n-k)$-form—the de Rham complex extends to include dual spaces. In three dimensions, this double complex is represented by:

$$\begin{array}{ccccccccc}
\mathbb{R} & \hookrightarrow & \Lambda^0(M) & \xrightarrow{d} & \Lambda^1(M) & \xrightarrow{d} & \Lambda^2(M) & \xrightarrow{d} & \Lambda^3(M) \to 0 \\
 & & \downarrow\star & & \downarrow\star & & \downarrow\star & & \downarrow\star \\
0 & \longleftarrow & \tilde{\Lambda}^3(M) & \xleftarrow{\tilde{d}} & \tilde{\Lambda}^2(M) & \xleftarrow{\tilde{d}} & \tilde{\Lambda}^1(M) & \xleftarrow{\tilde{d}} & \tilde{\Lambda}^0(M) \hookleftarrow \mathbb{R},
\end{array}$$

where $\tilde{\Lambda}^k(M)$ denotes the dual spaces under the Hodge $\star$. Here, the horizontal maps in the primal space are given by d, the vertical maps represent the Hodge $\star$ operator and the change in orientations to dual space and $\tilde{d}$ represents the exterior derivative in the dual space when the boundary conditions are all zero . In three dimensions, as mentioned in previous sections, the exterior derivative recovers the classical vector calculus operators such as *gradient*,*curl* and *divergence* and satisfies identities, such as $\nabla \times (\nabla f) = 0$ and $\nabla \cdot (\nabla \times \mathbf{A}) = 0$, which are direct consequences of $d \circ d = 0$ and can clearly be seen that the De Rham complex outlines these properties as well.

Up to this point, key concepts of manifolds, tangent and dual spaces, differential forms, and the operators d,$\star$ and $(,)$ have been introduced in a purely continuous setting, providing the theoretical backbone for mimetic methods. However, actual implementations of these methods require a transition from the continuous viewpoint to a discrete one, where preserving the essential geometric and topological properties is crucial for stability and accuracy.In the next chapter, the focus shifts to the discrete setting, explaining how these foundational ideas can be implemented in a spectral element context. By utilizing principles from Finite Element Exterior Calculus [26], which draw on concepts from Algebraic Topology, the exactness and duality inherent to the continuous theory are preserved.

4

Discrete Setting and Spectral Implementation

Mimetic discretizations combine continuous geometric concepts with carefully chosen discrete analogs to preserve critical structural properties at the discrete level. In algebraic topology, a manifold is replaced by a cell complex (often simplicial or polyhedral), whose sets of points, edges, faces, and volumes form the building blocks known as *chains*. Integrated differential forms then become *cochains*, which assign numerical values to these discrete elements via a *reduction* processes. The resulting framework mirrors the continuous manifold in a piecewise-linear fashion, preserving essential topological and geometric features.

Within this discrete setting, the incidence matrices associated with the cell complex serve as the counterpart to the exterior derivative, maintaining properties such as exactness and nilpotency. Consequently, relations akin to the generalized Stokes theorem naturally emerge: for instance, summing cochain values around the boundary of a collection of cells mirrors the continuous integral identities. Metric-dependent operators, by contrast, are approximated rather than preserved exactly. Specifically, discrete analogs of the Hodge $\star$ operator often take the form of mass matrices and introduce the main source of numerical error [23]. This arises because $\star$ encodes the local geometry (e.g., distances and angles) that can vary significantly over a discrete mesh.

4.1. Mesh - Discrete Manifold

The continuous manifold described in the previous chapter can be discretized by constructing a *mesh*, which in algebraic-topological language is a *cell complex* composed of 0-cells (points), 1-cells (edges), 2-cells (surfaces), and 3-cells (volumes). Assigning orientations and defining boundary relations on these cells creates a discrete analog of the continuous geometry, allowing for the representation of differential forms in a piecewise manner. In high-order *spectral element methods* (SEM), additional structure is introduced by placing *Gauss–Lobatto–Legendre* (GLL) nodes within each cell, facilitating precise numerical integration and interpolation. This combination of oriented cells, carefully chosen nodal distributions, and boundary mappings lays the groundwork for robust and accurate approximations of partial differential equations while retaining essential geometric and topological features.

A cell complex is built by specifying how individual p-dimensional objects, or p-*cells*, connect and adjoin [30]. For instance:

- **0-cells**: Points or vertices in the mesh.
- **1-cells**: Edges or line segments bounded by two vertices.
- **2-cells**: Surface patches enclosed by one or more edges.
- **3-cells**: Three-dimensional volumes bounded by 2-cells (in 3D problems).

A sum of p-cells with integer or real coefficients is referred to as a p-*chain* [14]. Orientation is assigned to each cell to keep track of sign conventions in discrete integrals, boundary operations, and flux directions. For example, choosing a direction along an edge fixes whether a traversal from one endpoint to the other is considered positive.

4.1.1. Primal and Dual Meshes

In many mimetic and spectral element methods, the mesh is subdivided into *primal* and *dual* grids, reflecting the concept of dual spaces introduced in the previous chapters. The *primal* mesh typically represents the physical geometry directly, while the *dual* mesh is constructed so that its cells intersect those of the primal mesh in a staggered arrangement. This nomenclature is tied to the orientation schemes outlined by Tonti [33] where *configuration* variables reside on the primal (inner-oriented) mesh, whereas *source* variables are associated with the dual (outer-oriented) mesh generally, though there is no out-right rule stating this order. By distributing complementary degrees of freedom across these two grids, the discrete model preserves topological invariants such as $\partial \circ \partial = 0$ where ∂ is the discrete counter part of the exterior derivative.

4.1.2. Spectral Element Grids and Gauss-Lobatto-Legendre (GLL) Nodes

A typical spectral element method (SEM) builds each mesh element from high-order polynomial expansions rather than just straight-edged or bilinear shapes. A common choice in these methods is to place collocation points at *Gauss–Lobatto–Legendre* (GLL) nodes [29, 30, 36, 43]. These nodes $\{\xi_0, \xi_1, \ldots, \xi_N\}$ lie in the interval $[-1, 1]$ and include the endpoints. Specifically, $\xi_0 = -1, \quad \xi_N = 1, \quad$ and $\quad \xi_i$ are the roots of,

$$(1 - \xi_i)\, L'_N(\xi) = 0 \qquad \text{for } -1 \leq \xi_i \leq 1 \quad \text{and} \quad i = 1, \ldots, N-1, \tag{4.1}$$

where $L_N(\xi)$ is the N-th Legendre polynomial and L'_N its derivative. GLL nodes facilitate accurate numerical integration and interpolation in both one-dimensional and multi-dimensional problems. In one dimension, these GLL points include the interval endpoints as well as interior collocation points. In two or three dimensions, tensor-product constructions extend this idea so that 0-forms (nodal variables) reside at vertices, while 1-forms might reside along edges, and 2-forms on surfaces and 3-forms on volumes, all at appropriately chosen GLL locations. This approach can be implemented for both primal and dual meshes which will be further detailed in the following sections. The Figure 4.1 below illustrate such GLL meshes in $\mathbb{R}^2$ for a polynomial order of $N = 3$.

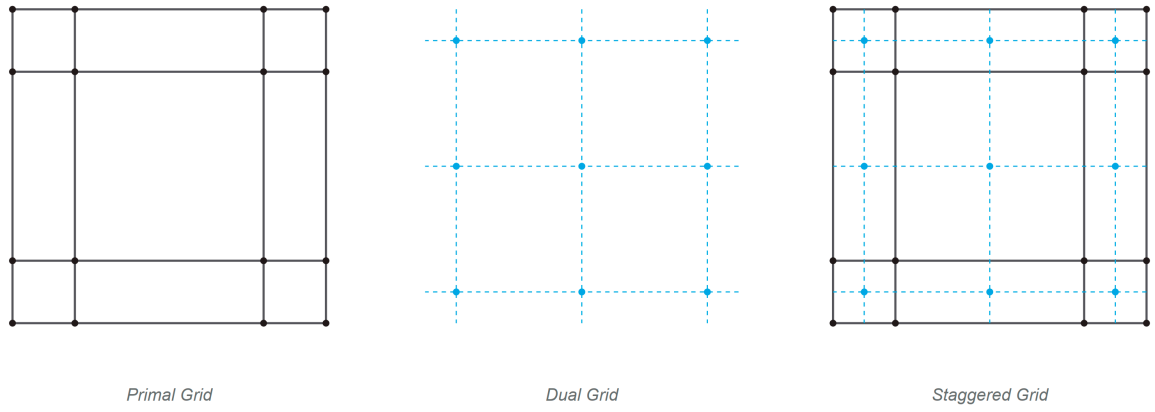

Figure 4.1: Primal, dual and staggered GLL grids in $\mathbb{R}^2$

4.2.Reduction and Reconstruction in a Spectral Framework

The *reduction* and *reconstruction* operators are central to linking continuous differential forms with their discrete analogs (cochains) in high-order mimetic and spectral element methods. This section introduces these two operators and shows how *nodal* and *edge* basis functions often constructed using Gauss-Lobatto-Legendre (GLL) nodes facilitate accurate polynomial approximations.

4.2.1. Reduction Operator

Let $\alpha^{(p)}$ be a differential p-form defined on a domain Ω that has been partitioned into p-cells making up a cell complex. The *reduction operator* R maps $\alpha^{(p)}$ to a p-cochain by integrating $\alpha^{(p)}$ over each p-cell $C^{(p)}$. Formally [18],

$$\left\langle R\alpha^{(p)},\, C^{(p)} \right\rangle \;:=\; \int_{C^{(p)}} \alpha^{(p)}, \tag{4.2}$$

where $\langle \cdot, \cdot \rangle$ denotes evaluation of the cochain on a chain. By linearity, the above definition extends to any p-chain composed of multiple cells.

A crucial property is that reduction commutes with the exterior derivative d and the discrete boundary operator δ:

$$R \,\circ\, d \;=\; \delta \,\circ\, R.$$

Hence, one may either first apply d in the continuous setting and then reduce, or first reduce and then apply δ, with no discrepancy in the outcome.

4.2.2. Reconstruction Operator

While reduction converts forms to cochains, the *reconstruction operator* I reverses this process by mapping a p-cochain back to an approximate differential p-form. It is a *left-inverse* of R, meaning

$$R \circ I \;=\; \mathrm{Id},$$

where Id is the identity on p-cochains. This guarantees that reconstructing a form from cochain data and then immediately reducing it recovers the same cochain values. However, I is only an *approximate right-inverse*: the composition $I \circ R$ approximates the identity on sufficiently smooth forms up to a chosen polynomial order. Additionally, it is often required that I commutes with d and δ, namely $I \circ \delta \;=\; d \circ I$, to preserve the structure of the de Rham complex in the discrete setting [30].

4.2.3. Nodal (Lagrange) Basis for 0-Forms

For discretizing scalar fields (0-forms), one typically uses the *Lagrange* basis associated with the GLL points. Let $\{\xi_0, \xi_1, \ldots, \xi_N\}$ be the set of GLL nodes on $[-1, 1]$ then the associated nodal Lagrange basis is defined as,

$$h_i(\xi) \;=\; \prod_{\substack{0 \le j \le N \\ j \neq i}} \frac{\xi - \xi_j}{\xi_i - \xi_j}, \quad i = 0, 1, \ldots, N. \tag{4.3}$$

These polynomials satisfy the Kronecker delta property $h_i(\xi_j) \;=\; \begin{cases} 1, & \text{if } i = j \\ 0, & \text{if } i \neq j \end{cases}$ If a 0-cochain Φ stores function values Φ_i at each node ξ_i, its reconstructed polynomial $\Phi_h(\xi)$ can be written as,

$$\Phi_h(\xi) \;=\; \sum_{i=0}^{N} \Phi_i \, h_i(\xi). \tag{4.4}$$

4.2.4. Edge Basis for 1-Forms

When handling vector fields or covector fields (1-forms), a suitable basis must reflect line integrals along edges. The construction of *edge basis functions* $e_i(\xi)$ according to [28] is done such that

$$\int_{\xi_{j-1}}^{\xi_j} e_i(\xi)\, d\xi \;=\; \delta_{ij}, \tag{4.5}$$

meaning each $e_i(\xi)$ integrates to one only on the edge $[\xi_{i-1},\, \xi_i]$ and zero elsewhere. A practical way to define $e_i(\xi)$ uses the nodal polynomials from (4.3) as shown in [28]

$$e_i(\xi) \;=\; -\sum_{k=0}^{i-1} \frac{d}{d\xi} \left[h_k(\xi) \right], \quad i = 1, \ldots, N. \tag{4.6}$$

In this form, each basis function e_i achieves the line-integral property given in (4.5). If a 1-cochain Ψ stores integral values Ψ_i over each sub-interval $[\xi_{i-1},\, \xi_i]$, its reconstructed 1-form $\Psi_h(\xi)$ can be expressed as

$$\Psi_h(\xi) \;=\; \sum_{i=1}^{N} \Psi_i \, e_i(\xi). \tag{4.7}$$

Under reduction, $\Psi_h(\xi)$ integrates to Ψ_i on the i-th edge, that is $\Psi_i = \int_{\xi_{i-1}}^{\xi_i} \Psi(\xi)\, d\xi$ recovering the original cochain data. These cochain values Ψ_i and Φ_i in the above examples, are generally known as the degrees of freedom of the discretised PDE in Finite Element formulations. The plots of both the nodal and edge basis in one-dimension are shown in the figure 4.2 below.

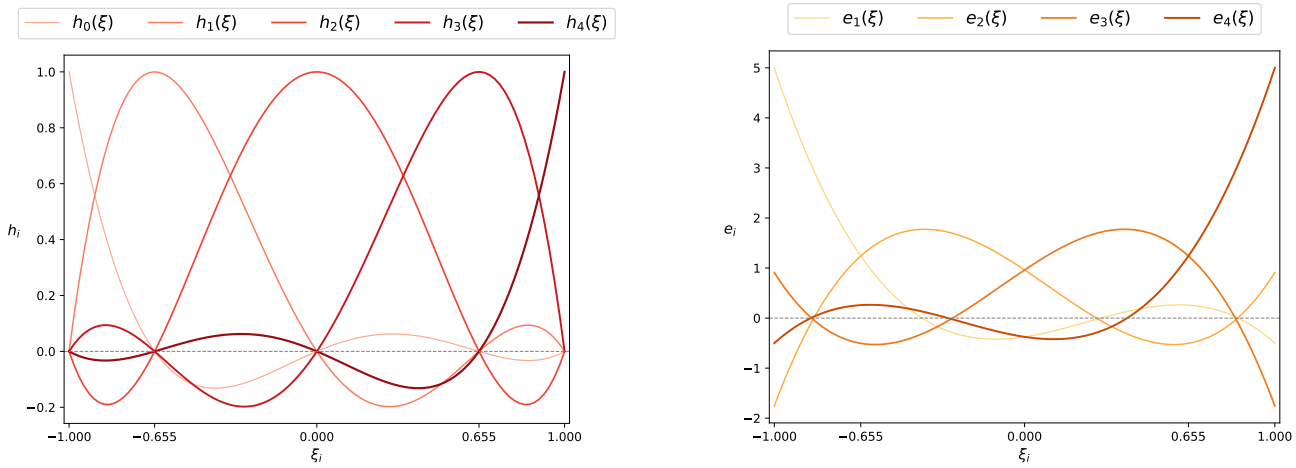

(a) Nodal Lagrange polynomial basis

(b) Edge polynomial basis

Figure 4.2: 1D basis functions for polynomial degree N = 4

4.2.5. Multi-Dimensional Polynomial Basis in Three Dimensions

In higher dimensions, the discrete spaces for differential forms (cochains) are built by taking tensor products of the one-dimensional (1D) nodal and edge polynomials introduced in Sections 4.2.3 and 4.2.4. A *k-form basis in d-dimensions* is formed by choosing *exactly k factors* of the edge polynomials (differentiated Lagrange polynomials) and $d-k$ *factors* of the nodal polynomials (undifferentiated Lagrange polynomials). Concretely:

- 0-form bases (for scalar fields) use nodal polynomials in every direction,
- 1-form bases have one edge direction and nodal polynomials in the other directions,
- 2-form bases have two edge directions and nodal polynomials in the remainder,
- …up to d-form bases, which involve an edge polynomial in each of the d directions.

This tensor-product approach ensures that each discrete k-form basis function integrates (or evaluates) to a Kronecker delta on the corresponding k-dimensional sub-cell (edge, face, volume, etc.), mirroring the 1D properties of Eqs. (4.5)–(4.6).

Consider the 3D reference domain $\Omega_{\text{ref}} = [-1,1]^3$ with coordinates (ξ,η,τ). Let $\{\xi_0,\dots,\xi_N\}$, $\{\eta_0,\dots,\eta_N\}$, and $\{\tau_0,\dots,\tau_N\}$ be the Gauss–Lobatto–Legendre (GLL) nodes partitioning each interval $[-1,1]$ in the ξ, η, and τ directions. Recall from Sections 4.2.3 and 4.2.4 that $h_i(\cdot)$ denotes the nodal (Lagrange) polynomial basis, while $e_i(\cdot)$ denotes the edge polynomial basis.

0-form basis in 3D. A discrete 0-form (scalar field) in three dimensions is approximated using only nodal polynomials in each direction:

$$\Phi_h^{(0)}(\xi,\eta,\tau) \;=\; \sum_{i=0}^{N}\sum_{j=0}^{N}\sum_{k=0}^{N} \Phi_{i,j,k} \Big(h_i(\xi) \;\otimes\; h_j(\eta) \;\otimes\; h_k(\tau) \Big). \tag{4.8}$$

Here, $\Phi_{i,j,k}$ is the value of the field at the nodal point (ξ_i, η_j, τ_k). As in 1D or 2D, these 3D tensor-product nodal basis functions satisfy a *pointwise* Kronecker-delta property at each nodal triple.

1-form basis in 3D. A discrete 1-form in three dimensions has three components, one associated with each coordinate direction:

- ξ**-component:**

$$\Psi_h^{(1,\xi)}(\xi,\eta,\tau) \;=\; \sum_{i=1}^{N}\sum_{j=0}^{N}\sum_{k=0}^{N} \Psi_{i,j,k}^{(\xi)} \Big(e_i(\xi) \;\otimes\; h_j(\eta) \;\otimes\; h_k(\tau)\Big), \tag{4.9}$$

- η**-component:**

$$\Psi_h^{(1,\eta)}(\xi,\eta,\tau) \;=\; \sum_{i=0}^{N}\sum_{j=1}^{N}\sum_{k=0}^{N} \Psi_{i,j,k}^{(\eta)} \Big(h_i(\xi) \;\otimes\; e_j(\eta) \;\otimes\; h_k(\tau)\Big), \tag{4.10}$$

- τ**-component:**

$$\Psi_h^{(1,\tau)}(\xi,\eta,\tau) \;=\; \sum_{i=0}^{N}\sum_{j=0}^{N}\sum_{k=1}^{N} \Psi_{i,j,k}^{(\tau)} \Big(h_i(\xi) \;\otimes\; h_j(\eta) \;\otimes\; e_k(\tau)\Big). \tag{4.11}$$

In each component, there is exactly *one* edge polynomial factor (e.g. $e_i(\xi)$) and *two* nodal polynomial factors (e.g. $h_j(\eta), h_k(\tau)$). By construction, the coefficient $\Psi_{i,j,k}^{(\xi)}$ represents the integral of the field along the ξ-edge bounded by (ξ_{i-1}, ξ_i) at fixed (η_j, τ_k), and similarly for the η- and τ-components.

2-form basis in 3D. A discrete 2-form (surface-like field) in 3D has three possible orientations (normals in the ξ, η, or τ direction). Consequently, each 2-form component contains *two* edge polynomial directions and *one* nodal direction. For instance, the component normal to ξ is

$$\Phi_h^{(2,\xi)}(\xi,\eta,\tau) \;=\; \sum_{i=0}^{N}\sum_{j=1}^{N}\sum_{k=1}^{N} \Phi_{i,j,k}^{(2,\xi)} \Big(h_i(\xi) \;\otimes\; e_j(\eta) \;\otimes\; e_k(\tau)\Big). \tag{4.12}$$

Analogously, one constructs $\Phi_h^{(2,\eta)}$ and $\Phi_h^{(2,\tau)}$ by using $e(\cdot)$ basis in the appropriate pairs of directions (with $h(\cdot)$ in the remaining one). Here, each coefficient $\Phi_{i,j,k}^{(2,\xi)}$ represents the surface integral value across the rectangular face at ξ_i spanned by $(\eta_{j-1}, \eta_j) \times (\tau_{k-1}, \tau_k)$.

3-form basis in 3D. Lastly, a discrete 3-form in three dimensions (think of a volumetric field) must involve *edge polynomials in all three directions*:

$$\Theta_h^{(3)}(\xi,\eta,\tau) \;=\; \sum_{i=1}^{N}\sum_{j=1}^{N}\sum_{k=1}^{N} \Theta_{i,j,k}^{(3)} \Big(e_i(\xi) \;\otimes\; e_j(\eta) \;\otimes\; e_k(\tau)\Big). \tag{4.13}$$

The coefficient $\Theta_{i,j,k}^{(3)}$ is the integral of $\Theta_h^{(3)}$ over the hexahedral sub-cell $[\xi_{i-1}, \xi_i] \times [\eta_{j-1}, \eta_j] \times [\tau_{k-1}, \tau_k]$.

In all cases, these tensor-product basis functions *inherit* the pointwise or integral Kronecker-delta properties from their 1D building blocks, ensuring that the expansion coefficients directly represent nodal values, edge fluxes, face fluxes, or volume integrals. Hence, the discrete degrees of freedom match physically meaningful quantities, making this construction *mimetic* (or *compatible*). For additional details, see, for example, [18, 26, 28, 35, 42]

4.3.Relation to Classical Finite Element Spaces

In finite element theory [19, 21, 24, 42], a *finite element* on a domain $K \subset \mathbb{R}^d$ is classically specified by:

- a topologically simple subdomain K with Lipschitz boundary (e.g. a GLL-meshed interval, quadrilateral, or hexahedron in this work),
- a finite-dimensional function space $\mathcal{P}$ (often polynomials of degree $\leq N$),

- a set of linear functionals $\{\mathcal{N}_i\}$ (the degrees of freedom) acting on $\mathcal{P}$ that define a bijection $\mathcal{P} \to \mathbb{R}^N$.

The polynomial-based cochain perspective in Sections 4.2 and 4.2.3–4.2.5 matches this setup naturally by identifying:

$$(i)\ K = [-1,1]^d, \quad (ii)\ \mathcal{P} = \text{polynomial basis up to degree } N, \quad (iii)\ \mathcal{N}_i = \text{nodal or integral cochains.}$$

A key property of these polynomial basis functions is that they mimic the Sobolev spaces found in finite elements:

$$H^1(\Omega), \quad H(\mathrm{curl};\Omega), \quad H(\mathrm{div};\Omega), \quad L^2(\Omega)$$

Concretely in $\mathbb{R}^3$ for example, 0-form basis correspond to H^1-conforming elements embedded in , 1-form basis to $H(\mathrm{curl})$ conforming elements , 2-form basis to $H(\mathrm{div})$ - conforming spaces, and 3-form basis to $L^2(\Omega)$. In summary, the "edge" and "nodal" polynomials introduced above form precisely the building blocks for high-order *spectral element* basis that also realize *classical finite element spaces* on GLL meshes.

4.4.Incidence Matrices - Discrete Exterior Derivative

Incidence matrices are fundamental to mimetic discretization methods because they encode the topological connectivity and orientation of a mesh. They serve as the discrete analogs of the exterior derivative 'd' from differential geometry and enable the exact implementation of differential operators (such as the gradient, curl, and divergence) in the discrete setting.

Consider a Gauss–Lobatto–Legendre (GLL) mesh in $\mathbb{R}^2$ with polynomial order $N = 2$, as illustrated in Figure 4.3. This mesh comprises:

- 9 nodes ($(N+1)^2$), depicted as p_i
- 12 edges ($2N(N+1)$), depicted as e_i
- 4 surfaces (N^2), depicted as s_i

Each of these geometrical elements is labelled following a lexicographic order. Additionally, the mesh elements are endowed with an inner orientation: nodes act as sinks, edges have positive orientations aligned with their respective axes, and surfaces are oriented clockwise.

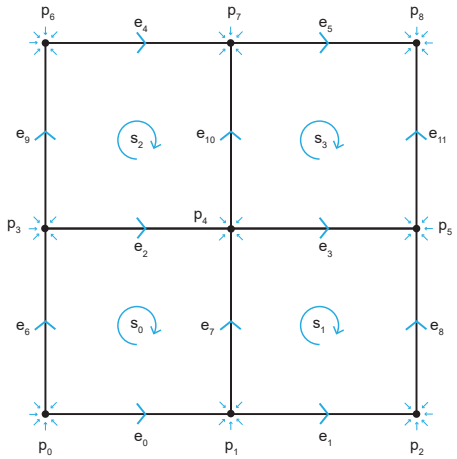

Figure 4.3: GLL Mesh of Polynomial Order $N = 2$

Let a scalar function φ be discretized on the above mesh using a nodal (0-form) expansion. The approximate function $\varphi_h(\xi,\eta)$ is written as

$$\varphi_h(\xi,\eta) \;=\; \sum_{i=0}^{N}\sum_{j=0}^{N} \varphi_{i,j}\, h_i(\xi)\, h_j(\eta), \tag{4.14}$$

where

- $h_i(\xi)$ and $h_j(\eta)$ denote the nodal basis functions,
- $\varphi_{i,j}$ represent the nodal degrees of freedom (0-form cochain values).

As mentioned earlier, for notational convenience, a lexicographic indexing is adopted: the point with coordinates (ξ_i, η_j) is denoted by $p_{i(N+1)+j}$.

From previous chapters, it is known that the exterior derivative acting on 0-forms produces 1-forms, corresponding to the gradient in the continuous setting. In the discrete framework, the resulting 1-forms are represented as integrated quantities along the edges of the mesh.

Applying the generalized Stokes theorem locally on an edge , E_1 with endpoints p_0 and p_1 for example, yields

$$\int_{E_1} d\varphi \;=\; \int_{p_0}^{p_1} \varphi \;=\; \varphi(p_1) - \varphi(p_0). \tag{4.15}$$

Since φ is expanded as in Eq. (4.14), the point evaluation $\varphi(p_i)$ corresponds directly to the nodal value $\overline{\varphi}_i$.

By applying the Stokes theorem to all edges of the mesh, the contributions from the nodal degrees of freedom are assembled into a matrix that defines the discrete gradient operator acting on the degrees of freedom (i.e. the expansion coefficient) , denoted by $\mathbb{E}^{1,0}$ as shown below. The superscripts indicate that the operator maps nodal values (0-cochains) to edge-integrated values (1-cochains).

$$\begin{pmatrix} \int\limits_{E_1} \nabla\,\overline{\varphi}\; dE_1 \\ \int\limits_{E_1} \nabla\,\overline{\varphi}\; dE_2 \\ \vdots \\ \int\limits_{E_{12}} \nabla\,\overline{\varphi}\; dE_{12} \end{pmatrix} = \begin{pmatrix} -1 & 1 & 0 & 0 & 0 & 0 & 0 & 0 & 0 \\ 0 & -1 & 1 & 0 & 0 & 0 & 0 & 0 & 0 \\ 0 & 0 & 0 & -1 & 1 & 0 & 0 & 0 & 0 \\ 0 & 0 & 0 & 0 & -1 & 1 & 0 & 0 & 0 \\ 0 & 0 & 0 & 0 & 0 & 0 & -1 & 1 & 0 \\ -1 & 0 & 0 & 1 & 0 & 0 & 0 & 0 & 1 \\ 0 & 0 & 0 & 0 & 0 & 0 & 0 & 0 & 0 \\ 0 & -1 & 0 & 0 & 1 & 0 & 0 & 0 & 0 \\ 0 & 0 & -1 & 0 & 0 & -1 & 1 & 0 & 0 \\ 0 & 0 & 0 & 0 & 0 & 0 & 0 & -1 & 1 \end{pmatrix} \begin{pmatrix} \overline{\varphi}_0 \\ \overline{\varphi}_1 \\ \vdots \\ \overline{\varphi}_8 \end{pmatrix} \tag{4.16}$$

Geometrically, considering the example of E_1, the default orientation of the edge is in the positive ξ-direction, connecting nodes p_0 and p_1, which are sink-like. In this orientation, the edge enters the sink at p_1 and exits the sink at p_0, meaning it has the same orientation as the edge at p_1 and an opposing orientation at p_0. This relationship is reflected in the incidence matrix, where the corresponding entries are $+1$ and -1, respectively.

Each row of $\mathbb{E}^{1,0}$ corresponds to an edge, with the entries in that row representing the contribution of the nodal values at the edge's endpoints. The signs are determined by the relative orientation between the edge and the nodes:

- $+1$ if the edge enters a sink-like node.
- -1 if the edge leaves a sink-like node.

This convention ensures that the incidence matrix correctly encodes the orientation and connectivity of the mesh. An alternative approach to deriving the incidence matrix $\mathbb{E}^{1,0}$ involves polynomial expansions. Instead of relying on discrete geometric arguments, this approach constructs incidence matrices by analyzing the structure of polynomial basis functions and their derivatives. By expressing a function in terms of nodal basis polynomials, the differentiation process naturally leads to a structured transformation of degrees of freedom and the basis. In the one-dimensional case, nodal values determine the coefficients of basis polynomials, while differentiation introduces relationships between adjacent nodal degrees of freedom, forming a structured difference pattern. This pattern can be encoded as an incidence matrix that maps nodal values to integral edge degrees of freedom. The same idea extends to multiple dimensions, for additional details, see [28, 42].

Having defined the discrete gradient $\mathbb{E}^{1,0}$, we now construct the next incidence matrix, $\mathbb{E}^{2,1}$, which acts as the discrete curl operator in two dimensions. It maps integral edge values (1-cochains) to integral surface values (2-cochains).

By applying the generalized Stokes theorem (cf. §4.4) on each 2-cell (surface/face),

$$\int_S (\nabla \times \mathbf{u}) \cdot \hat{n} \, \mathrm{d}S \;=\; \oint_{\partial S} \mathbf{u} \cdot \hat{t} \, \mathrm{d}\ell, \tag{4.17}$$

we see that the integrated curl of $\mathbf{u}$ over a face S is exactly the sum of the fluxes on its boundary edges ∂S. Following the same oriented-incidence convention as before, each row of $\mathbb{E}^{2,1}$ collects the contribution of the edges bounding a particular face, with ± 1 signs determined by the relative orientations of those edges. In the above mesh, there are four cells/surfaces and twelve edges, giving a (4×12) matrix $\mathbb{E}^{2,1}$.

$$\mathbb{E}^{2,1} = \begin{pmatrix} -1 & 0 & 1 & 0 & 0 & 0 & 0 & 1 & -1 & 0 & 0 & 0 & 0 \\ 0 & -1 & 0 & 1 & 0 & 0 & 0 & 0 & 1 & -1 & 0 & 0 & 0 \\ 0 & 0 & -1 & 0 & 1 & 0 & 0 & 0 & 0 & 0 & 1 & -1 & 0 \\ 0 & 0 & 0 & -1 & 0 & 1 & 0 & 0 & 0 & 0 & 0 & 1 & -1 \end{pmatrix} \tag{4.18}$$

The incidence matrices $\mathbb{E}^{1,0}$ and $\mathbb{E}^{2,1}$ introduced earlier are also known as *coboundary operators* in algebraic topology. These matrices connect cochains of consecutive degrees (0-forms to 1-forms, and 1-forms to 2-forms) and preserve the fundamental topological property that the "boundary of a boundary is zero." In the discrete setting, this property is expressed through the exactness relations

$$\mathbb{E}^{2,1}\,\mathbb{E}^{1,0} = 0, \quad \text{and more generally} \quad \mathbb{E}^{k+1,k}\,\mathbb{E}^{k,\,k-1} = 0,$$

which mirror the continuous identities $\nabla \times (\nabla \varphi) = 0$ and $\nabla \cdot (\nabla \times \mathbf{u}) = 0$. Together with suitable projectors, these coboundary matrices form the core of a *discrete de Rham complex*, preserving essential geometric and topological structures at the discrete level.

The discussion so far has considered an *inner* orientation, where nodes function as sinks and surfaces are oriented clockwise. As a result, the discrete gradient ($\mathbb{E}^{1,0}$) and discrete curl ($\mathbb{E}^{2,1}$) operators have been introduced. However, the *divergence* operator in 2D or 3D typically requires an *outer-orientation*, which will be for the associated dual mesh, in which surface normals point outward. Consequently, the corresponding incidence matrix for divergence has not yet been presented. This topic will be addressed in the following sections, where a dual (outer) orientation is introduced, along with a construction of $\tilde{\mathbb{E}}^{2,1}$ on that dual mesh to recover the standard notion of divergence.

4.5.Discrete Hodge $\star$ Operator

In the continuous setting, the Hodge-$\star$ operator (sometimes denoted $\star$ or $*$) acts as an isomorphism between k-forms and $(n-k)$-forms by switching both dimension and orientation. Specifically, it transforms inner-oriented objects into outer-oriented ones (and vice versa) while also incorporating the metric of the underlying manifold. In the discrete setting, this principle translates into a map between k-cochains and $(n-k)$-cochains that carry the opposite orientation.

A k-cochain in a cell complex is an assignment of real values to k-dimensional geometric elements (oriented in a certain way). Applying the discrete Hodge operator $\star$ changes both the dimension and the orientation type of those elements, yielding $(n-k)$-cochains. Topological operators such as the boundary or co-boundary (incidence matrices) do not fully capture this switch in orientation, since those operators are independent of metric data. By contrast, the $\star$ operator is metric-dependent, reflecting the geometric attributes (e.g., distances and angles) of the manifold or mesh.

4.5.1. Mass Matrix as the Discrete Hodge in Galerkin Formulations

In the Galerkin approach, a continuous partial differential equation typically takes the form

$$\mathcal{L}\,\omega^{(k-1)} = 0, \quad \omega^{(k-1)} \in \Lambda^{k-1}(\Omega), \tag{4.19}$$

where $\mathcal{L}$ is a linear operator (e.g., involving first order derivatives) acting on a $k-1$-form $\omega^{(k-1)}$. To derive its weak (Galerkin) form, a test k-form $\beta^{(k)}$ is chosen from the same functional space as the solution and multiplied through the equation, followed by a wedge product with $*\,\beta^{(k)}$ and an integral over the domain Ω. Symbolically,

$$\int_\Omega \big(\mathcal{L}\,\omega^{(k-1)}\big) \;\wedge\; \big(*\,\beta^{(k)}\big) \;=\; 0. \tag{4.20}$$

Depending on the nature of $\mathcal{L}$, an integration-by-parts step may be invoked to move derivatives off of $\omega^{(k-1)}$ onto $\beta^{(k)}$, producing boundary terms or flux-like expressions that must be handled by suitable boundary or interface conditions.

After applying these steps ($\mathcal{L}\,\omega^{(k-1)} = \alpha^{(k)}$), the formulation involves integrals of the form

$$\int_\Omega \alpha^{(k)} \;\wedge\; \big(*\,\beta^{(k)}\big), \tag{4.21}$$

In this weak formulation, $\star$ denotes the continuous Hodge star and $\alpha^{(k)}, \beta^{(k)}$ are both k-forms. A high-order finite or spectral element approach then approximates $\alpha^{(k)}$ and $\beta^{(k)}$ within a finite-dimensional subspace spanned by basis functions $\{\psi_j^{(k)}\}$. Specifically,

$$\alpha_h^{(k)} \;=\; \sum_j \alpha_j\,\psi_j^{(k)}, \quad \beta_h^{(k)} \;=\; \sum_i \beta_i\,\psi_i^{(k)}. \tag{4.22}$$

Substituting these expansions into the weak form leads to a system of algebraic equations in the unknown degrees of freedom $\{\alpha_j\}$. The integrals that arise in these equations are consistent with the metric-dependent inner product (wedge product in L^2) and produces a *mass matrix* $\mathbb{M}^{(k)}$ defined by

$$\mathbb{M}^{(k)}[i,j] \;=\; \int_\Omega \psi_j^{(k)} \;\wedge\; \big(\star\,\psi_i^{(k)}\big), \tag{4.23}$$

As a result, the matrix $\mathbb{M}^{(k)}$ fulfills the role of the *discrete* Hodge star applied to the degrees of freedom.

$$\star\,\alpha_h^{(k)} \;\longleftrightarrow\; \mathbb{M}^{(k)}\,\alpha_i. \tag{4.24}$$

Hence, if α_i collects the integral values associated with the k-form, then $\mathbf{M}^{(k)}\,\alpha_i$ provides the co-chain values of the $(n-k)$-form, thereby encoding the dimension and orientation change in the discrete setting. Earlier sections introduced the idea that constitutive equations commonly relate k-forms and $(n-k)$-forms in a metric-sensitive manner. For example, in fluid dynamics, a constitutive law may pair velocity (a 1-form in 2d-spacetime $\mathbb{R}^{2+1}$) with momentum (a 2-form) through a material-dependent metric (Density/Mass). In the mimetic spectral element framework, the mass matrix (discrete Hodge) encodes this pairing: the $\star$ operator translates a co-chain of degree k (inner-oriented) into its complementary co-chain of degree $(n-k)$ (outer-oriented). Thus, the same matrix that arises in the weak formulation as the discrete Hodge operator also enforces the constitutive relation that depends on the metric or material properties.

When using a spectral element approach, the basis functions $\psi_j^{(k)}$ typically originate from mapping a reference domain (such as $[-1,1]^n$) onto each physical element of Ω. This mapping incorporates a Jacobian determinant and a metric tensor, both of which enter into the definition of $\star$. Consequently, each element's local contribution to the mass matrix includes metric-dependent factors such as the determinant of the Jacobian of the mapping $\sqrt{\det(g)}$ and directional scaling terms. High-order Gauss–Lobatto–Legendre quadrature is commonly employed to evaluate these integrals with the necessary precision [42]. Further details regarding the construction and properties of mass matrices in high-order settings can be found in [35, 36, 42, 43].

4.6. Dual Basis Functions and Differential Operators on the Dual Grid

In finite element methods the choice of basis functions is critical for both the accuracy and efficiency of the numerical solution. Typically, one begins with a *primal* finite element basis discussed in the previous sections. However, when constructing discrete differential operators or enforcing constraints via weak formulations, it can be advantageous to work with a *dual* basis that is bi-orthogonal to the primal basis. The dual basis is obtained by a transformation involving the mass matrix, which plays a role analogous to the Hodge star operator in differential geometry as shown in the previous section.

The general formula for obtaining the dual basis function is given by

$$\tilde{\Psi}^{(n-k)} = \Psi^k \left[\mathbb{M}^k\right]^{-1}, \tag{4.25}$$

where Ψ^k represents the vector of basis functions associated with an oriented k-form, and $\tilde{\Psi}^{(n-k)}$ denotes its dual, corresponding to the complementarily oriented $(n-k)$-form. For a more rigorous derivation of dual basis functions, refer to [42].

4.6.1. Dual Nodal Basis

These basis functions are dual to the edge functions $e(\xi)$, which are defined on the edges of the primal grid. The dual nodal basis functions are instead defined on the nodes of the dual grid as follows in 1D:

$$\tilde{h}(\xi) = e(\xi) \left[\mathbb{M}^1\right]^{-1}, \tag{4.26}$$

where the mass matrix $\mathbb{M}^{(1)}$ is given by

$$\mathbb{M}^{(1)}_{ij} = \int_{\xi_{i-1}}^{\xi_i} e_i(\xi) e_j(\xi)\, d\xi \quad \text{for} \quad i = 1, 2, \ldots, N. \tag{4.27}$$

4.6.2. Dual Edge Basis

These basis functions are dual to the nodal functions $h(\xi)$, which are defined at the nodes of the primal grid. The dual edge basis functions are instead defined on the edges of the dual grid as follows in 1D:

$$\tilde{e}(\xi) = h(\xi) \left[\mathbb{M}^0\right]^{-1}, \tag{4.28}$$

where the mass matrix $\mathbb{M}^{(0)}$ is given by

$$\mathbb{M}^{(0)}_{ij} = \int_{\xi_{i-1}}^{\xi_i} h_i(\xi) h_j(\xi)\, d\xi \quad \text{for} \quad i = 0, 1, \ldots, N. \tag{4.29}$$

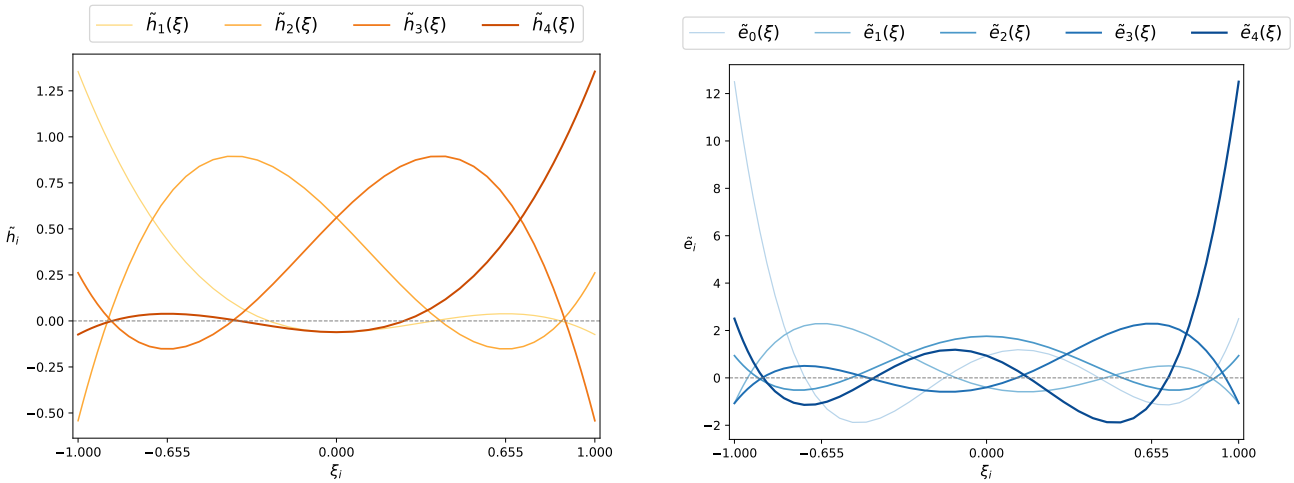

(a) Dual Nodal polynomial basis

(b) Dual Edge polynomial basis

Figure 4.4: 1D Dual basis functions for polynomial degree N = 4

Beyond their importance in defining degrees of freedom, dual basis functions play a crucial role in constructing *discrete differential operators* on the dual grid [42], when applying integration by parts in a weak formulation, the appearance of the mass matrix naturally leads to expressions involving the dual basis functions. In a primal (nodal) setting, we typically have basis functions $\{\psi_i\}$ that allow for a strong (pointwise) derivative:

$$\frac{d}{d\xi} u_h(\xi) = \sum_{i=0}^{N} u_i \, h_i'(\xi), \tag{4.30}$$

or in higher dimensions,

$$\nabla u_h(\mathbf{x}) = \sum_i u_i \, \nabla \psi_i(\mathbf{x}).$$

In contrast, a field defined in the dual setting (for example, an element in $H(\mathrm{div})$-like discrete spaces, when the primal grid is inner oriented) often has integral-type degrees of freedom:

$$\tilde{u}_i = \int_{\tilde{V}_i} u \, dV, \tag{4.31}$$

where $\tilde{V}_i$ is an element of the *dual mesh* (often a cell associated to a node, an edge, or a face, depending on the dimension and the PDE). Such fields lack a local pointwise representation in the same sense and thus require a *weak* derivative in the finite element assembly process. Consider a generic term from a conservation law discretized on a 2D grid, that involves a divergence of a dual variable. The continuous integration by parts identity is:

$$\int_\Omega v \, \nabla \cdot \tilde{u} \, dV = -\int_\Omega \nabla v \cdot \tilde{u} \, dV \; + \int_{\partial\Omega} v \, \tilde{u} \cdot \mathbf{n} \, dS, \tag{4.32}$$

where $\mathbf{n}$ is the outward normal on $\partial\Omega$. Discretizing, one obtains a matrix equation that can be interpreted as:

$$\tilde{\mathbb{E}}^{2,1} = \left[-\mathbb{E}^{2,1}\right]^T + \mathbb{N}^{2,1}, \tag{4.33}$$

where:

- $\mathbb{E}^{2,1}$ is the *primal curl* or gradient operator (depending on context),
- $\mathbb{E}^{2,1^T}$ is its transpose acting on dual forms,
- $\mathbb{N}^{2,1}$ is a boundary inclusion matrix enforcing the fluxes (or tangential components) at the boundary.
- $\tilde{\mathbb{E}}^{2,1}$ represents the discrete divergence operator on the dual grid.

4.7.Discrete De Rham complex

A useful way to encapsulate the behavior of differential operators in both the continuous and discrete settings is via the *De Rham complex*. The continuous one was detailed in the previous chapter, now that all the ingredients required to define the discreet counterpart are defined in this chapter, thus in 2-dimensions it can be constructed in the following way :

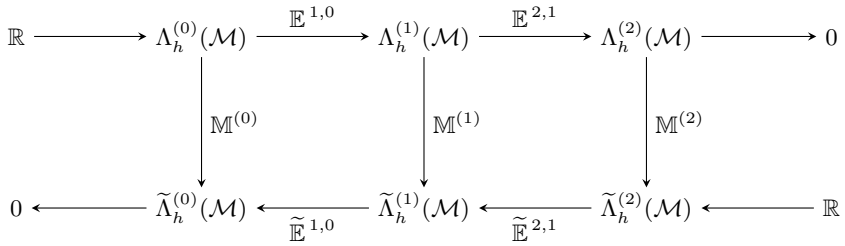

Figure 4.5: Discrete De Rham complex in two dimensions

The top row shows the finite-dimensional spaces of differential forms, while the bottom row depicts their dual spaces. Horizontal arrows represent discrete exterior derivatives, and vertical arrows indicate mass-matrix mappings.

5

Lagrangian Formulation of Barotropic Flow

5.1.Flow Description in the Lagrangian Viewpoint

To derive the barotropic flow equations in the Lagrangian framework, it is essential first to establish the concepts of reference configuration, flow maps, and deformed configuration, along with the associated deformation gradient. These definitions provide the basis for understanding the transformation of fluid configuration and enable a systematic approach to formulating the governing equations via the variational principle discussed in the coming sections.

5.1.1. Reference Configuration

The *reference configuration*, denoted as the undeformed or initial state of the fluid, is represented by its spatial configuration at $t = 0$. This configuration can be described as a compact domain $\mathcal{B} \subset \mathbb{R}^n$, where each point $\boldsymbol{X} \in \mathcal{B}$ corresponds to a unique particle label. This particle label $\boldsymbol{X}$ identifies the position of fluid particle within the reference configuration, effectively marking its location before any deformation or motion occurs. By establishing this initial layout, we create a basis from which we can track the deformation and displacement of fluid particles over time as they transition from the reference configuration to the deformed configurations throughout the flow process.

5.1.2. Deformed Configuration and Flow Map

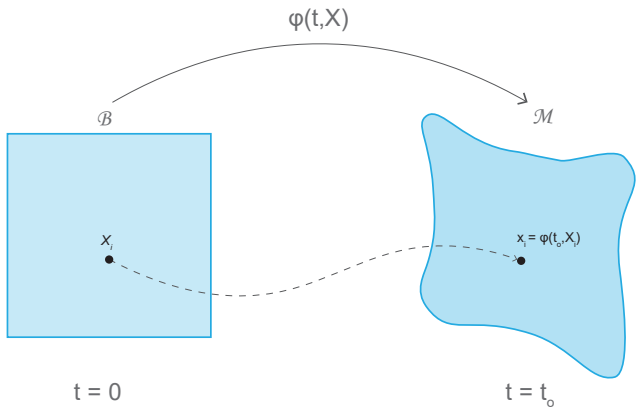

Figure 5.1: Reference and Deformed Configurations with Flow Map $\varphi(t, X)$

The *flow map*, $\varphi : \mathcal{B} \to \mathcal{M}$, is a one-to-one isomorphic mapping that describes the motion of fluid particles over time. As illustrated in the figure 5.1, given a particle labeled by $\boldsymbol{X} \in \mathcal{B}$ in the reference configuration $\mathcal{B}$, the flow map provides its position $x = \varphi(t, \boldsymbol{X})$ at any time t within the deformed configuration. The *deformed configuration* at time t is thus the spatial layout of the fluid as it has moved or deformed from its initial state. This configuration, represented as the region $\mathcal{M} = \varphi(t, \mathcal{B}) \subset \mathbb{R}^n$, shows the transformed positions of all fluid particles from the reference configuration.

5.1.3. Deformation Gradient

The deformation gradient quantifies the deformation in the reference configuration of the fluid, by considering the change in the flow map. Considering a 2D example with the fluid particle label $\boldsymbol{X} = \sum_{i=1}^{2} X_i \boldsymbol{e_i}$, where e_i represent the orthonormal basis for $\mathbb{R}^2$, Then the deformation gradient tensor $\boldsymbol{F}(t, \boldsymbol{X})$ is given by,

$$\boldsymbol{F}(t, \boldsymbol{X}) = \begin{bmatrix} \dfrac{\partial \varphi^1}{\partial X_1} & \dfrac{\partial \varphi^1}{\partial X_2} \\ \dfrac{\partial \varphi^2}{\partial X_1} & \dfrac{\partial \varphi^2}{\partial X_2} \end{bmatrix}$$

Now, in general the deformation gradient can be represented as, $\boldsymbol{F} = \boldsymbol{\nabla \varphi}$, with each individual elements given by,

$$F_{ij} = \frac{\partial \varphi^i}{\partial X_j} = \varphi^i_{,j} = \nabla_j \varphi^i. \tag{5.1}$$

The quantity $J(t, m) = det\ \boldsymbol{F}(t, \boldsymbol{X})$ of the flow configuration is the determinant of the deformation gradient, which provides the deformation of φ at $\boldsymbol{x}$, hence J can be considered as the ratios of densities at reference configuration ρ_o to the deformed configuration ρ.

$$J = det\ \boldsymbol{F}(t, \boldsymbol{X}) = \frac{\rho_o}{\rho(t, \boldsymbol{X})}. \tag{5.2}$$

5.2.Barotropic Fluids

A fluid is termed barotropic when its density fluctuations are solely the result of pressure changes, establishing a direct correlation between the fluid's density and its pressure. Which means that for any given value of pressure, there is a corresponding and unique density value, and vice versa. Consequently, in a barotropic fluid, isobaric surfaces (surfaces of constant pressure) and isopycnic surfaces (surfaces of constant density) coincide. This property simplifies the analysis of fluid motion because the state of the fluid can be described by a single variable (either pressure or density).

$$p = p(\rho), \quad U = U(\rho),$$

Where U represents the internal energy of the fluid, which is a function of reference density ρ_o and deformation gradient J, since $\rho = \rho(\rho_o, J)$, thus internal energy is related to volume change during deformation. From the first law of thermodynamics, the change in internal energy of the fluid can be written as,

$$dU = dQ - dW.$$

Where W represents the work done on the fluid, further in the absence of heat exchange or viscous dissipation ($dQ = 0$), and any other form of work except the work due to deformation, the equation reduces to,

$$dU = -dW, \quad dU = -(P_W)dV,$$

Where P_W is the material pressure and V represents the volume of the fluid, considering the change with respect to deformation J,

$$\frac{\partial U}{\partial J} = -P_W \frac{\partial V}{\partial J}, \quad P_W = -\frac{\partial U}{\partial J}\frac{\partial J}{\partial V},$$

Obtaining the final expression for the material pressure in terms of change in internal energy,

$$P_W(\rho_o, J) = -\rho_o \frac{\partial U(\rho_o, J)}{\partial J}. \tag{5.3}$$

5.3.Lagrangian Variational Formalism

The equations governing barotropic fluid dynamics are derived through the application of Hamilton's principle, this requires finding the configuration for which the action integral, formulated from the Lagrangian representing the system's kinetic and potential energy, which is stationary.

The Lagrangian density $\mathcal{L} = T - \mathcal{V}$ of a barotropic fluid with kinetic energy, $T = \frac{1}{2}\rho_o \left|\dot{\varphi}\right|^2$, internal energy $U(\rho_o, J)$ and potential energy $\Pi(\varphi)$, such that $V = \rho_o U(\rho_o, J) + \rho_o \Pi(\varphi)$ is described as in [38],

$$\mathcal{L}(\varphi, \dot{\varphi}, \nabla\varphi) = \frac{1}{2}\rho_o \left|\dot{\varphi}\right|^2 - \rho_o U(\rho_o, J) - \rho_o \Pi(\varphi). \tag{5.4}$$

The Hamilton's principle states that,

$$\delta \int_0^T \int_{\mathcal{B}} \mathcal{L}(\varphi, \dot{\varphi}, \nabla\varphi)\, dt\, dX = 0. \tag{5.5}$$

Now the above equation 5.5 can be solved by applying the Euler-Lagrange equations from variational calculus (refer to Appendix A), to minimize the functional $\mathcal{L}(\varphi, \dot{\varphi}, \nabla\varphi)$, For arbitrary variations of φ vanishing at $t = 0$ and $t = T$ we obtain,

$$\frac{\partial}{\partial t}\left(\frac{\partial \mathcal{L}}{\partial \dot{\varphi}}\right) + \frac{\partial}{\partial X_j}\left(\frac{\partial \mathcal{L}}{\partial \nabla_j \varphi^i}\right) - \frac{\partial \mathcal{L}}{\partial \varphi} = 0. \tag{5.6}$$

Similar to the temporal boundary, the variations of the flow configuration are set to zero on the spatial boundary, resulting in a natural boundary condition,

$$\frac{\partial \mathcal{L}}{\partial \nabla_j \varphi^i}.n_j.\delta\varphi^i = 0. \tag{5.7}$$

by substituting 5.4 in 5.6 we obtain,

$$\frac{\partial}{\partial t}(\rho_o \dot{\varphi}) + \frac{\partial}{\partial X_j}\left(\frac{\partial}{\partial \nabla_j \varphi^i}(-\rho_o U(\rho_o, J))\right) - \frac{\partial}{\partial \varphi}(-\rho_o \Pi(\varphi)) = 0,$$

$$\rho_o \ddot{\varphi} + \frac{\partial}{\partial X_j}\left(-\rho_o \frac{\partial U}{\partial J}\frac{\partial J}{\partial \nabla_j \varphi^i}\right) + \rho_o \frac{\partial \Pi}{\partial \varphi} = 0.$$

The term $\dfrac{\partial J}{\partial \nabla_j \varphi^i}$ in the above equation represents the derivative of the determinant of a matrix with respect to its elements. This is given by Jacobi's formula for the derivative of a determinant. Refer to Appendix B for the complete derivation.

$$\frac{\partial \det(A)}{\partial A_{ij}} = \det(A) \cdot \left(A^{-1}\right)_{ji} \tag{5.8}$$

$$\frac{\partial J}{\partial \nabla_j \varphi^i} = \frac{\partial (det(\boldsymbol{F}))}{\partial \boldsymbol{F}_{ij}} = det(\boldsymbol{F}).(\boldsymbol{F}^{-1})_{ji} = J\boldsymbol{F}^{-T}.$$

Further from 5.3 we know that $P_W(\rho_o, J) = -\rho_o \dfrac{\partial U(\rho_o, J)}{\partial J}$, by substituting the above two results we get the Barotropic Fluid equations in the Lagrangian description, along with the natural boundary conditions,

$$\boxed{\rho_o \ddot{\varphi}_i + \frac{\partial}{\partial X_j}\left(P_W J \boldsymbol{F}^{-T}\right)_{ij} + \rho_o \frac{\partial \Pi}{\partial \varphi_i} = 0.} \tag{5.9}$$

Along with the associated natural boundary conditions,

$$P_W J (\boldsymbol{F}^{-T})^j_i \boldsymbol{n_i} \delta\varphi^i = 0 \quad \text{on } \partial\mathcal{B} \tag{5.10}$$

The above equations translate to a pressure condition $P_W = 0$ on the boundary. Thus, to prescribe nonzero pressure boundary conditions, the Lagrangian should be modified by introducing the external pressure P_{ext} (boundary) in the internal energy expression, such that:

$$P_W(\rho_o, J) = -\rho_o \frac{\partial U}{\partial J} = P_f - P_{ext},$$

where P_f is the fluid barotropic pressure, thereby equation 5.10 would lead to,

$$(P_{\mathsf{f}} - P_{\mathsf{ext}}) J \boldsymbol{F}^{-T}.\boldsymbol{n}\ \delta\varphi^i = 0, \quad \text{thus} \quad P_f = P_{ext} \quad \text{on} \quad \partial\mathcal{B}. \tag{5.11}$$

5.3.1. Piola-Kirchoff Stress Tensor

The well known, *Cauchy stress tensor* is the fundamental measure of stress in the current configuration (deformed) of a continuum. It specifies the traction that one part of the continuum exerts on another across an infinitesimal surface. In a barotropic fluid where viscosity and other deviatoric stresses are negligible, the Cauchy stress tensor reduces to

$$\boldsymbol{T} \;=\; -p\,\boldsymbol{I}, \tag{5.12}$$

where p is the pressure, and $\boldsymbol{I}$ is the identity tensor. This representation highlights the isotropic character of pressure in an inviscid or ideal fluid. Although $\boldsymbol{T}$ is measured with respect to surfaces and normals in the *current* configuration, Lagrangian fluid-mechanics formulations include a stress measure defined on the *reference* (undeformed) configuration. The first Piola–Kirchhoff stress tensor $\mathbf{P}$ accomplishes this by providing the force acting in the *deformed* configuration per unit area in the *reference* configuration. Continuum-mechanics texts [25, 39] often define $\mathbf{P}$ as:

$$\mathbf{P} \;=\; \frac{\partial W}{\partial \boldsymbol{F}}, \tag{5.13}$$

where $W(\boldsymbol{F}) \;=\; \rho_0\, U\big(\rho_0, J\big)$ is the internal (or strain) energy density, expressed in Lagrangian coordinates. For a *barotropic fluid*, as shown in the previous section, this takes the form of

$$\mathbf{P} \;=\; -P_W J \boldsymbol{F}^{-T} \tag{5.14}$$

The scalar Jacobian determinant J accounts for local volumetric changes, and $\boldsymbol{F}^{-T}$ ensures the transformation from the reference to current configuration is included correctly. Transformations of surface elements from the reference domain $\mathcal{B}$ to the current domain are governed by Nanson's formula. If $\mathrm{d}\boldsymbol{A}_0$ is an oriented surface element in the reference domain with outward normal $\boldsymbol{N}$, then its corresponding oriented surface element in the current domain is

$$\mathrm{d}\boldsymbol{A} \;=\; J\boldsymbol{F}^{-T}\,\mathrm{d}\boldsymbol{A}_0. \tag{5.15}$$

This identity shows how measuring force per unit area in the reference configuration ($\mathbf{P}$) differs from measuring it in the deformed configuration ($\boldsymbol{T}$). Thus the first Piola-Kirchoff stress tensor can also be obtained by applying this *Nanson's Formula* to the Cauchy stress tensor, effectively switching from "true" (current-configuration) stress to "nominal" (reference-configuration) stress,

$$\mathbf{P} \;=\; -J\boldsymbol{T}\,\boldsymbol{F}^{-T}. \tag{5.16}$$

Essentially, the first Piola-Kirchhoff tensor $\mathbf{P}$ captures how a given material volume element in the reference configuration develops forces that appear as the isotropic pressure forces in the current configuration. The tensor $\mathbf{P}$ appears naturally via the variational formulation for barotropic fluids in the Lagrangian coordinates, as shown in the previous sections. From a differential-geometric standpoint, $\mathbf{P}$ corresponds to the one-sided pullback of the Cauchy stress tensor $\mathbf{T}$ [22]. In this construction, the area element is measured in the reference configuration, while the forces themselves are still considered in the deformed configuration.

5.4.From Lagrangian to Hamiltonian Description

The Euler–Lagrange equations governing barotropic fluid flow were derived in earlier sections by starting from the Lagrangian density, applying Hamilton's principle, and obtaining

$$\rho_o\,\ddot{\varphi}_i \;+\; \frac{\partial}{\partial x_i}\Big(P_W\,J\,\boldsymbol{F}^{-T}\Big)^i \;+\; \rho_o\,\frac{\partial \Pi}{\partial \varphi_i} \;=\; 0, \tag{5.17}$$

as in Equation 5.9. The next step is to recast these equations in a Hamiltonian framework by means of a Legendre transform in time, following the analogy with finite-dimensional Hamiltonian mechanics. A *canonical momentum* $\boldsymbol{\pi}$ (per unit reference volume) conjugate to φ is introduced through the standard relation

$$\boldsymbol{\pi}(\boldsymbol{X},t) \;=\; \frac{\partial \mathcal{L}}{\partial \dot{\varphi}} \;=\; \rho_0\,\dot{\varphi}, \tag{5.18}$$

where $\mathcal{L}$ is the Lagrangian density,

$$\mathcal{L}\big(\varphi,\dot{\varphi},\nabla\varphi\big) \;=\; \frac{1}{2}\,\rho_0\,\big|\dot{\varphi}\big|^2 \;-\; \rho_0\,U\big(\rho_0,J\big) \;-\; \rho_0\,\Pi\big(\varphi\big), \tag{5.19}$$

and $\dot{\varphi} \equiv \partial\varphi/\partial t$. The definition of $\boldsymbol{\pi}$ is analogous to the finite-dimensional expression $p = \partial L/\partial\dot{q}$ in classical mechanics. A *Legendre transform* of $\mathcal{L}$ with respect to $\dot{\varphi}$ produces the Hamiltonian density $\mathcal{H}$. Specifically, the definition is

$$\mathcal{H}\big(\varphi,\boldsymbol{\pi},\nabla\varphi\big) \;=\; \boldsymbol{\pi}\cdot\dot{\varphi} \;-\; \mathcal{L}\big(\varphi,\dot{\varphi},\nabla\varphi\big). \tag{5.20}$$

Since $\dot{\varphi} = \boldsymbol{\pi}/\rho_0$, substitute this relation back to find

$$\mathcal{H}\big(\varphi,\boldsymbol{\pi},\nabla\varphi\big) \;=\; \frac{1}{2\,\rho_0}\,\big|\boldsymbol{\pi}\big|^2 \;+\; \rho_0\,U\big(\rho_0,J\big) \;+\; \rho_0\,\Pi\big(\varphi\big). \tag{5.21}$$

The Hamiltonian density then depends on $\boldsymbol{\pi}$ and on $\nabla\varphi$ (through $J = \det(\nabla\varphi)$), reflecting the usual split between coordinates and momenta in time. The function $\mathcal{H}$ can be interpreted physically as the total energy density of the barotropic fluid. When integrated over the reference domain $\mathcal{B}$, it yields the total energy. More explicitly,

$$E \;=\; \int_{\mathcal{B}} \mathcal{H}\big(\varphi,\boldsymbol{\pi},\nabla\varphi\big)\,d^nX, \tag{5.22}$$

which represents the sum of kinetic, internal, and potential energies. For the barotropic flow considered here,

$$E \;=\; \int_{\mathcal{B}}\left(\frac{1}{2\,\rho_0}\,|\boldsymbol{\pi}|^2 \;+\; \rho_0\,U(\rho_0,J) \;+\; \rho_0\,\Pi(\varphi)\right)d^nX. \tag{5.23}$$

This quantity remains constant in time if the Lagrangian density does not explicitly depend on time and if appropriate boundary conditions are satisfied.

5.5.Noether's Theorem and Conservation Laws

Noether's theorem provides a connection between *continuous symmetries* in a physical system and *conserved quantities*. In practical terms, if a barotropic fluid's Lagrangian does not change under some continuous transformation (for example, shifting time or shifting positions in space), the equations of motion imply that a corresponding physical quantity remains constant. Consider an action functional

$$\mathcal{A} \;=\; \int_{t=0}^{t=T} \int_{\mathcal{B}} \mathcal{L}\big(\varphi, \partial_t \varphi, \nabla \varphi\big)\, \mathrm{d}^n X \, \mathrm{d}t \tag{5.24}$$

that determines how a barotropic fluid evolves. If changing the time variable by a small shift $t \mapsto t + \delta t$ has *no effect* on $\mathcal{A}$ (other than possibly rewriting boundary terms), then energy cannot be created or destroyed. As a result, the total energy of the fluid remains constant in time. Similarly, if the action does not change under small shifts of space $\boldsymbol{X} \mapsto \boldsymbol{X} + \delta \boldsymbol{a}$, then the total (linear) momentum must be constant.

In the mathematical formulation, the key object is a *Noether current*, which can be viewed as a localized measure of the conserved quantity. The statement of Noether's theorem shows that this current satisfies a continuity equation, indicating that the quantity in question can neither spontaneously appear nor vanish within the fluid domain.

Time-translation symmetry. A barotropic fluid's Lagrangian typically does not include any explicit time dependence (aside from the evolving fields). This leads to an exact conservation of *total energy*, reflecting kinetic, internal, and potential contributions.

Space-translation symmetry. If the fluid domain and governing equations are uniform in space, then shifting positions leaves the action unchanged. This symmetry implies *linear momentum conservation*. In practice, it manifests as a momentum balance law that can be written in either material (Lagrangian) or spatial (Eulerian) coordinates.

Rotational symmetry. In isotropic fluids, the Lagrangian remains the same under rotations of the reference or spatial coordinates. The outcome is *angular momentum conservation*. Physically, this means any net spinning or rotational effect remains constant unless forces or torques act at the boundary.

The transition from a Lagrangian to a Hamiltonian description, and further to a multi-symplectic formulation, reveals deeper geometric structures in barotropic fluid flow. The Lagrangian and Hamiltonian approaches clarify canonical momentum, energy, and the way variational principles specify the equations of motion. A multi-symplectic representation then allows time and space to be treated symmetrically, leading to local conservation of symplectic forms in multiple dimensions. Noether's theorem connects continuous symmetries of the action with physically significant conservation laws, including energy, momentum, and angular momentum.

When applied in numerical practice, preserving geometric or symmetry-based invariants often improves stability and accuracy, especially over long simulations. Multi-symplectic methods, in particular, impose a discrete version of the symplectic conservation law across space–time grids, ensuring that numerical approximations respect core physical properties inherent to barotropic flows.

6

Weak Formulation and the Full Discrete System

6.1.Strong Form and Classification

In the previous chapter, we derived the strong form of the Lagrangian inviscid barotropic flow equations via a variational formulation. Neglecting the gravitational potential term, the resulting strong form is:

$$\rho_o \ddot{\varphi} + \frac{\partial}{\partial X_j} \left(P_W J \boldsymbol{F}^{-T} \right)_j = 0. \tag{6.1}$$

where, φ is the flowmap, ρ_0 is the (constant) reference density, P_W is the material pressure of the fluid, $\mathbf{F}$ is the deformation gradient, $J = \det(\mathbf{F})$ is the determinant of the deformation gradient. The above equation can be re-written, to classify and separate the equation into *Balance*, *constitutive* and *Definition* equations as follows,

$$\begin{cases} \dfrac{\partial \boldsymbol{\pi}_i}{\partial t} - \dfrac{\partial}{\partial X_j}(\boldsymbol{P})_{ij} = 0 & \textit{Balance Equation} \\ \boldsymbol{\pi}_i = \rho_0 \dfrac{\partial \varphi_i}{\partial t} & \textit{Constitutive Equation} \\ \boldsymbol{P}_{ij} = -P_W J \boldsymbol{F}^{-T}_{ij} & \textit{Constitutive Equation} \\ \boldsymbol{F}_{ij} = \dfrac{\partial \varphi_i}{\partial X_j} & \textit{Definition Equation} \end{cases} \tag{6.2}$$

Here, π is the linear momentum density, $\boldsymbol{P}$ is the first Piola-Kirchhoff stress tensor. These four sets of equations respectively represent the local form of momentum balance, two constitutive relationships (one for the momentum π and another for the stress $\boldsymbol{P}$), and the definition of the deformation gradient.

6.2. Variable Representation in Two Dimensional Space and Time $\mathbb{R}^{2+1}$

In a two-dimensional Cartesian space, any vector- or covector-valued physical quantity naturally splits into two components—one along the x-axis and one along the y-axis—and these often appear in separate momentum balance and constitutive equations. Nevertheless, using *bundle-valued forms* defined on a single space-time manifold $\mathcal{M}$ allows both components to be discretized coherently on the discrete counterpart of the manifold. Thus the variables pertaining to the problem are represented as follows,

Flow map - $\boldsymbol{\varphi}$: The flow map is described as a vector-valued 0-form in both space and time belonging to $\Lambda^{(0)}(\boldsymbol{\mathcal{M}})$.

$$\boldsymbol{\varphi}^{(0)} = \boldsymbol{\partial}_x \otimes \varphi_x^{(0)}(\xi,\eta,\tau) + \boldsymbol{\partial}_y \otimes \varphi_y^{(0)}(\xi,\eta,\tau). \tag{6.3}$$

Velocity - $\boldsymbol{V}$: Velocity is described as a vector-valued 0-form in space and a 1-form in time belonging to $\Lambda^{(1)}(\boldsymbol{\mathcal{M}})$.

$$\boldsymbol{V}^{(0)} = \boldsymbol{\partial}_x \otimes V_x^{(1)}(\xi,\eta,\tau)\ dt + \boldsymbol{\partial}_y \otimes V_y^{(1)}(\xi,\eta,\tau)\ dt. \tag{6.4}$$

$$V_x^{(0)} = \frac{\partial \varphi_x^{(0)}}{\partial t}, \quad V_y^{(0)} = \frac{\partial \varphi_y^{(0)}}{\partial t}.$$

Deformation Gradient - $\boldsymbol{F}$: It is described as a vector-valued 1-form in space and a 0-form in time belonging to $\Lambda^{(1)}(\boldsymbol{\mathcal{M}})$.

$$\boldsymbol{F}^{(1)} = \boldsymbol{\partial}_x \otimes \left(F_{xx}^{(1)}(\xi,\eta,\tau)\,dx + F_{xy}^{(1)}(\xi,\eta,\tau)\,dy\right) + \boldsymbol{\partial}_y \otimes \left(F_{yx}^{(1)}(\xi,\eta,\tau)\,dx + F_{yy}^{(1)}(\xi,\eta,\tau)\,dy\right) \tag{6.5}$$

$$F_{xx}^{(1)} = \frac{\partial \varphi_x^{(0)}}{\partial x}, \quad F_{xy}^{(1)} = \frac{\partial \varphi_x^{(0)}}{\partial y}, \quad F_{yx}^{(1)} = \frac{\partial \varphi_y^{(0)}}{\partial x}, \quad F_{yy}^{(1)} = \frac{\partial \varphi_y^{(0)}}{\partial y}.$$

Momentum - $\boldsymbol{\pi}$: Momentum is described as a co-vector valued 2-form in space and a 0-form in time belonging to $\tilde{\Lambda}^{(2)}(\boldsymbol{\mathcal{M}})$

$$\boldsymbol{\pi}^{(2)} = (\boldsymbol{d}x \otimes \pi_x^{(2)}(\xi,\eta,\tau) + \boldsymbol{d}y \otimes \pi_y^{(2)}(\xi,\eta,\tau))\ dx \wedge dy. \tag{6.6}$$

First Piola-Kirchoff Stress - $\boldsymbol{P}$: It is described as a co-vector valued 2 space-time form, that is, a 1-form in space and a 1-form in time belonging to $\tilde{\Lambda}^{(2)}(\boldsymbol{\mathcal{M}})$.

$$\boldsymbol{P}^{(2)} = \boldsymbol{d}x \otimes \left(P_{xx}^{(2)}(\xi,\eta,\tau)\ dy - P_{xy}^{(2)}(\xi,\eta,\tau)\ dx\right) \wedge dt + \boldsymbol{d}y \otimes \left(P_{yx}^{(2)}(\xi,\eta,\tau)\ dy - P_{yy}^{(2)}(\xi,\eta,\tau)\ dx\right) \wedge dt \tag{6.7}$$

6.3.Discretisation on the Mesh

The first step in discretisation involves classifying the variables into *Configuration* and *Source* variables. From the definitions in the previous chapter and sections, it is trivial that the flow map, velocity and deformation gradient act as the configuration variables and the momentum and Piola-Kirchoff stress act as the source variables.

6.3.1. Primal and Dual Grid

In a Lagrangian framework, the fundamental configuration variables $\boldsymbol{\varphi}$ naturally appear in the Lagrangian($\mathcal{L}(\varphi, \dot{\varphi}, \nabla\varphi)$) defining the spatial arrangement of fluid elements. Since the *primal* grid provides the first, direct discrete representation of the fluid domain, it is characteristic to place these *vector-valued configuration fields* on the primal mesh. In contrast, *covector-valued source variables* such as forces, momentum, or stresses do not define geometry but rather act upon the configuration thus they are defined on a dual grid, further it can be seen that their influence is analogous to the dual grid, which remains concealed (its points may not coincide with physical locations). Although neither the source variables nor the dual cells are directly observed, their interaction is manifested in the changes induced in the visible (primal) configuration.

6.3.2. Orientation

In many geometric and topological approaches to numerical partial differential equations, the *primal* grid is assigned an *inner orientation*, whereas the *dual* grid is given an *outer orientation* [13, 26]. This choice indicates how gradient- and divergence-like operations are naturally represented in a discrete setting. First, because the primal mesh has the *configuration* variables (e.g., position, displacement, or velocity potentials), the definition equations involving gradients are discretised on it, thus having it as an inner-oriented mesh makes it convenient to define the discrete gradient operator. Meanwhile, the divergence operator is closely linked to outward-pointing normals on boundary surfaces. Assigning an outer orientation to the dual cells simplifies the representation of fluxes and balance laws, since each dual face inherits a naturally outward-pointing normal that is used in discrete divergence computations. Thus, the divergence—or more generally, the flux balance—finds a natural setting on the outer-oriented dual mesh. Finally, coupling an inner-oriented primal grid for gradients with an outer-oriented dual grid for divergences allows both discrete operators to mimic their continuous counterparts in a geometrically compatible way. This alignment often leads to better stability and conservation properties in numerical simulations.

6.3.3. Geometric Association

Once the primal and dual associations, orientation selection, and variable representations are established, associating physical variables with the geometric elements of the mesh becomes straightforward. The table below illustrates this relationship, where N denotes the spatial polynomial order and N_t denotes the temporal polynomial order of the spectral GLL grid.

Integral Quantities / DOFs	Geometry	Grid	Number of elements
$\bar{\varphi}$	Nodes	Primal	$(N_t+1)(N+1)^2$
$\bar{\boldsymbol{F}}$	Spatial Edges	Primal	$2(N_t+1)N(N+1)$
$\bar{\boldsymbol{V}}$	Temporal Edges	Primal	$N_t(N+1)^2$
$\bar{\boldsymbol{\pi}}$	Spatial Faces	Dual	$N_t(N+1)^2$
$\bar{\boldsymbol{P}}$	Spatio-Temporal Faces	Dual	$2(N_t+1)N(N+1)$

Table 6.1: Geometric association of physical variables on the Primal and Dual Grid

The figure below shows both the primal and dual GLL grid, along with the associated variables for a spatial polynomial order of $\boldsymbol{N}=2$ and temporal polynomial order of $\boldsymbol{N}_t=1$. Here $\boldsymbol{\xi}$ corresponds to X direction, $\boldsymbol{\eta}$ to y and $\boldsymbol{\tau}$ denotes the temporal direction.

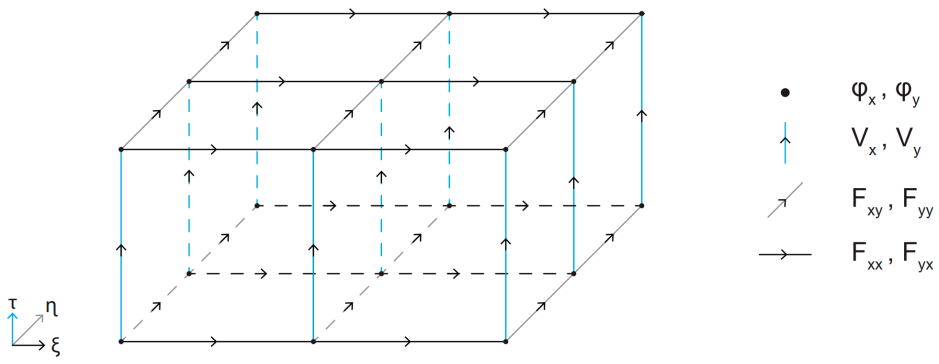

Figure 6.1: Primal Grid along with the representation of associated variables

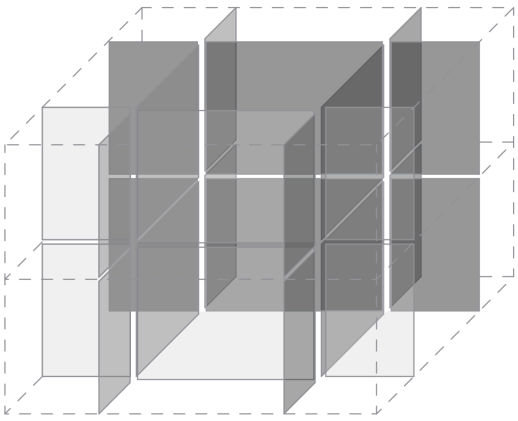

Figure 6.2: Spatio-temporal surfaces depicting the Piola-Kirchoff stress DOFs on the dual grid

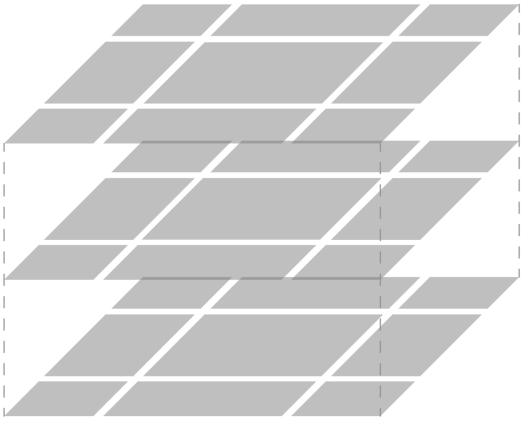

Figure 6.3: Spatial surfaces depicting the momentum DOFs on the dual grid

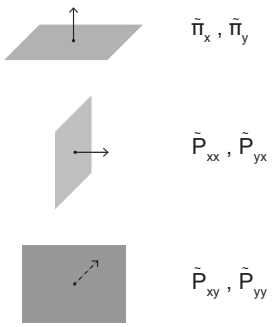

Figure 6.4: Dual Grid along with the representation of associated variables

6.3.4. Spectral Basis Expansion

For the $\mathbb{R}^{(2+1)}$ grid shown above, the basis functions used to expand the above discussed variables, can be constructed at the Gauss-Lobatto-Legendre (GLL) co-ordinates (ξ, η, τ):

$$\xi = \xi_0,\ \xi_1, \ldots, \xi_{N+1}, \quad \eta = \eta_0,\ \eta_1, \ldots, \eta_{N+1}, \quad \tau = \tau_0,\ \tau_1, \ldots, \tau_{N_t+1}$$

using tensor products of one-dimensional basis functions, as previously discussed. Specifically, they are formulated as follows:

Primal Nodal Basis: The primal nodal basis functions $\mathbf{\Psi}_0$, are defined as the tensor product of one-dimensional nodal Lagrange basis functions, and belong to the discrete space $\Lambda_h^{(0)}(\mathcal{B} \times T)$ which can also be interpreted as the space $H^1(\mathcal{B} \times T) \subset L^2(\mathcal{B} \times T)$.

$$\mathbf{\Psi}_0 = h(\xi) \otimes h(\eta) \otimes h(\tau) \tag{6.8}$$

which, in index notation, expands to $\mathbf{\Psi}_0 = h_i(\xi)\ h_j(\eta)\ h_k(\tau), \quad \forall\ i, j = 0, 1, \ldots, N, \quad k = 0, 1, \ldots, N_t.$

Primal Edge Basis: The edge basis are obtained similarly by tensor product of combination of edge basis in that respective direction and nodal basis in remaining directions. They belong to the discrete space $\Lambda_h^{(1)}(\mathcal{B} \times T)$ which can also be interpreted as the space $H\ (grad\ ;\ \mathcal{B} \times T)$.

$$\boldsymbol{\Psi}_1 = \begin{bmatrix} e(\xi) \otimes h(\eta) \otimes h(\tau) & 0 & 0 \\ 0 & h(\xi) \otimes e(\eta) \otimes h(\tau) & 0 \\ 0 & 0 & h(\xi) \otimes h(\eta) \otimes e(\tau) \end{bmatrix} \tag{6.9}$$

which in index notation expands to:

- Edge in the ξ-direction : $\boldsymbol{\Psi}_1^{\xi} = e_i(\xi)\; h_j(\eta)\; h_k(\tau), \quad \forall\, i = 1, 2, \ldots, N, \quad j = 0, 1, \ldots, N, \quad k = 0, 1, \ldots, N_t.$
- Edge in the η-direction : $\boldsymbol{\Psi}_1^{\eta} = h_i(\xi)\; e_j(\eta)\; h_k(\tau), \quad \forall\, i = 0, 1, \ldots, N, \quad j = 1, 2, \ldots, N, \quad k = 0, 1, \ldots, N_t.$
- Edge in the τ-direction : $\boldsymbol{\Psi}_1^{\tau} = h_i(\xi)\; h_j(\eta)\; e_k(\tau), \quad \forall\, i, j = 0, 1, \ldots, N, \quad k = 1, 2, \ldots, N_t.$

Dual Surface Basis: The dual surface basis functions are constructed by taking the tensor product of a dual edge basis function in two coordinate directions and a nodal basis in the perpendicular direction. They belong to the discrete space $\tilde{\Lambda}_h^{(2)}(\mathcal{B} \times T)$ which can also be interpreted as the space $H\;(div\;;\; \mathcal{B} \times T)$.

$$\tilde{\boldsymbol{\Psi}}_2 = \begin{bmatrix} \tilde{h}(\xi) \otimes \tilde{e}(\eta) \otimes \tilde{e}(\tau) & 0 & 0 \\ 0 & \tilde{e}(\xi) \otimes \tilde{h}(\eta) \otimes \tilde{e}(\tau) & 0 \\ 0 & 0 & \tilde{e}(\xi) \otimes \tilde{e}(\eta) \otimes \tilde{h}(\tau) \end{bmatrix} \tag{6.10}$$

which in index notation, expands to:

- Surface $\perp$ to the ξ-direction :

$$\boldsymbol{\Psi}_2^{\xi} = \tilde{h}_i(\xi)\, \tilde{e}_j(\eta)\, \tilde{e}_k(\tau), \quad \forall\, i = 0, 1, \ldots, N, \quad j = 1, 2, \ldots, N, \quad k = 1, 2, \ldots, N_t.$$

- Surface $\perp$ to the η-direction :

$$\boldsymbol{\Psi}_2^{\eta} = \tilde{e}_i(\xi)\, \tilde{h}_j(\eta)\, \tilde{e}_k(\tau), \quad \forall\, i = 1, 2, \ldots, N, \quad j = 0, 1, \ldots, N, \quad k = 1, 2, \ldots, N_t.$$

- Surface $\perp$ to the τ-direction :

$$\boldsymbol{\Psi}_2^{\tau} = \tilde{e}_i(\xi)\, \tilde{e}_j(\eta)\, \tilde{h}_k(\tau), \quad \forall\, i = 1, 2, \ldots, N, \quad j = 1, 2, \ldots, N, \quad k = 0, 1, \ldots, N_t.$$

Based on the above definitions, the discrete physical variables are spectrally expanded as follows,

Flowmap φ: Flowmap is associated to primal nodes, thus it is expanded using the primal nodal basis and the associated degrees of freedom $\bar{\boldsymbol{\varphi}}_x$ and $\bar{\boldsymbol{\varphi}}_y$ as follows,

$$\varphi_x^h\;(\xi, \eta, \tau) := \bar{\boldsymbol{\varphi}}_x\; \Psi_0 = \sum_{i=0}^{N} \sum_{j=0}^{N} \sum_{k=0}^{N_t} \bar{\varphi}_{ijk}^{x}\; h_i(\xi)\; h_j(\eta)\; h_k(\tau) \tag{6.11}$$

$$\varphi_y^h\;(\xi, \eta, \tau) := \bar{\boldsymbol{\varphi}}_y\; \Psi_0 = \sum_{i=0}^{N} \sum_{j=0}^{N} \sum_{k=0}^{N_t} \bar{\varphi}_{ijk}^{y}\; h_i(\xi)\; h_j(\eta)\; h_k(\tau) \tag{6.12}$$

Deformation Gradient $\boldsymbol{F}$: The deformation gradient is associated with Primal Spatial edges, thus it will be expanded using $\boldsymbol{\Psi}_1^{\xi}$ and $\boldsymbol{\Psi}_1^{\eta}$ edge basis functions along with the respective degrees of freedom $\bar{\boldsymbol{F}}_{xx}$, $\bar{\boldsymbol{F}}_{xy}$, $\bar{\boldsymbol{F}}_{yx}$ and $\bar{\boldsymbol{F}}_{yy}$ which are integral values of the deformation along the edges.

$$F_{xx}^h\;(\xi, \eta, \tau) := \bar{\boldsymbol{F}}_{xx}\; \Psi_1^{\xi} = \sum_{i=1}^{N} \sum_{j=0}^{N} \sum_{k=0}^{N_t} \bar{F}_{ijk}^{xx}\; e_i(\xi)\; h_j(\eta)\; h_k(\tau) \tag{6.13}$$

$$F_{xy}^h\;(\xi, \eta, \tau) := \bar{\boldsymbol{F}}_{xy}\; \Psi_1^{\eta} = \sum_{i=0}^{N} \sum_{j=1}^{N} \sum_{k=0}^{N_t} \bar{F}_{ijk}^{xy}\; h_i(\xi)\; e_j(\eta)\; h_k(\tau) \tag{6.14}$$

$$F^h_{yx}\ (\xi,\eta,\tau) := \bar{\boldsymbol{F}}_{yx}\ \Psi^{\xi}_1 = \sum_{i=1}^{N}\sum_{j=0}^{N}\sum_{k=0}^{N_t} \bar{F}^{yx}_{ijk}\ e_i(\xi)\ h_j(\eta)\ h_k(\tau) \tag{6.15}$$

$$F^h_{yy}\ (\xi,\eta,\tau) := \bar{\boldsymbol{F}}_{yy}\ \Psi^{\eta}_1 = \sum_{i=0}^{N}\sum_{j=1}^{N}\sum_{k=0}^{N_t} \bar{F}^{yy}_{ijk}\ h_i(\xi)\ e_j(\eta)\ h_k(\tau) \tag{6.16}$$

Velocity $\boldsymbol{V}$: Velocity is associated to primal or temporal edges, thus it is expanded using $\boldsymbol{\Psi}^{\tau}_1$ edge basis and the associated degrees of freedom $\bar{\boldsymbol{V}}_x$ and $\bar{\boldsymbol{V}}_y$, which are the integral values of the velocity along the temporal edges.

$$V^h_x\ (\xi,\eta,\tau) := \bar{\boldsymbol{V}}_x\ \Psi^{\tau}_1 = \sum_{i=0}^{N}\sum_{j=0}^{N}\sum_{k=0}^{N_t} \bar{V}^{x}_{ijk}\ h_i(\xi)\ h_j(\eta)\ h_k(\tau) \tag{6.17}$$

$$V^h_y\ (\xi,\eta,\tau) := \bar{\boldsymbol{V}}_y\ \Psi^{\tau}_1 = \sum_{i=0}^{N}\sum_{j=0}^{N}\sum_{k=1}^{N_t} \bar{V}^{y}_{ijk}\ h_i(\xi)\ h_j(\eta)\ e_k(\tau) \tag{6.18}$$

Momentum $\tilde{\boldsymbol{\pi}}$ The momentum is associated to dual surfaces, thus it is expanded using the dual spatial surface basis $\tilde{\boldsymbol{\Psi}}^{\tau}_2$ and the degrees of freedom $\tilde{\boldsymbol{\pi}}_x$ and $\tilde{\boldsymbol{\pi}}_y$ which are the integral values of the momentum along the respective surfaces.

$$\pi^h_x\ (\xi,\eta,\tau) := \tilde{\boldsymbol{\pi}}_x \boldsymbol{\Psi}^{\tau}_2 = \sum_{i=1}^{N}\sum_{j=1}^{N}\sum_{k=0}^{N_t} \tilde{\pi}^{x}_{ijk}\ \tilde{e}_i(\xi)\,\tilde{e}_j(\eta)\,\tilde{h}_k(\tau) \tag{6.19}$$

$$\pi^h_y\ (\xi,\eta,\tau) := \tilde{\boldsymbol{\pi}}_y \boldsymbol{\Psi}^{\tau}_2 = \sum_{i=1}^{N}\sum_{j=1}^{N}\sum_{k=0}^{N_t} \tilde{\pi}^{y}_{ijk}\ \tilde{e}_i(\xi)\,\tilde{e}_j(\eta)\,\tilde{h}_k(\tau) \tag{6.20}$$

First Piola-Kirchoff stress $\boldsymbol{P}$: It is associated with dual spatio-temporal surfaces, and thus is expanded using the dual surface basis $\boldsymbol{\Psi}^{\xi}_2$ and $\boldsymbol{\Psi}^{\eta}_2$ along with the degrees of freedom $\tilde{\boldsymbol{P}}_{xx}$, $\tilde{\boldsymbol{P}}_{xy}$, $\tilde{\boldsymbol{P}}_{yx}$ and $\tilde{\boldsymbol{P}}_{yy}$, which are the integral values of the stress along the respective surfaces.

$$P^h_{xx}\ (\xi,\eta,\tau) := \tilde{\boldsymbol{P}}_{xx}\ \tilde{\Psi}^{\xi}_2 = \sum_{i=0}^{N}\sum_{j=1}^{N}\sum_{k=1}^{N_t} \tilde{P}^{xx}_{ijk}\ \tilde{h}_i(\xi)\tilde{e}_j(\eta)\ \tilde{e}_k(\tau) \tag{6.21}$$

$$P^h_{xy}\ (\xi,\eta,\tau) := \tilde{\boldsymbol{P}}_{xy}\ \tilde{\Psi}^{\eta}_2 = \sum_{i=1}^{N}\sum_{j=0}^{N}\sum_{k=1}^{N_t} \tilde{P}^{xy}_{ijk}\ \tilde{e}_i(\xi)\ \tilde{h}_j(\eta)\ \tilde{e}_k(\tau) \tag{6.22}$$

$$P^h_{yx}\ (\xi,\eta,\tau) := \tilde{\boldsymbol{P}}_{yx}\ \tilde{\Psi}^{\xi}_2 = \sum_{i=0}^{N}\sum_{j=1}^{N}\sum_{k=1}^{N_t} \tilde{P}^{yx}_{ijk}\ \tilde{h}_i(\xi)\ \tilde{e}_j(\eta)\ \tilde{e}_k(\tau) \tag{6.23}$$

$$P^h_{yy}\ (\xi,\eta,\tau) := \tilde{\boldsymbol{P}}_{yy}\ \tilde{\Psi}^{\eta}_2 = \sum_{i=1}^{N}\sum_{j=0}^{N}\sum_{k=1}^{N_t} \tilde{P}^{yy}_{ijk}\ \tilde{e}_i(\xi)\ \tilde{h}_j(\eta)\ \tilde{e}_k(\tau) \tag{6.24}$$

6.4.Continuous Weak Formulation

The momentum balance equation, expressed in terms of differential bundle forms, is given by

$$d_t\ \boldsymbol{\pi}^{(2)} - d\ \boldsymbol{P}^{(2)} = 0, \tag{6.25}$$

where d_t denotes the temporal component of the exterior derivative acting on 2-forms, akin to a temporal divergence, and d represents the spatial component, acting as a spatial divergence.

To derive the weak form, as discussed in previous chapters, the strong form is tested by taking the wedge product with the Hodge dual of an arbitrary test form $\star\,\eta^{(3)}$, which belongs to the same space of forms as the solution, $\Lambda^{(3)}(\boldsymbol{\mathcal{M}})$. Integrating over the domain yields:

$$\int_{\mathcal{M}} d_t\boldsymbol{\pi}^{(2)} \;\wedge\; \star\,\eta^{(3)} \;-\; \int_{\mathcal{M}} d\boldsymbol{P}^{(2)} \;\wedge\; \star\,\eta^{(3)} = 0, \qquad \forall\,\eta^{(3)} \;\in \tilde{\Lambda}^{(3)}(\boldsymbol{\mathcal{M}}). \tag{6.26}$$

Following a similar approach, the weak form of the momentum-velocity constitutive equation is obtained as:

$$\int_{\mathcal{M}} \frac{1}{\rho_o}\boldsymbol{\pi}^{(2)} \;\wedge\; \star\alpha^{(2)} \;+\; \int_{\mathcal{M}} d_t\boldsymbol{\varphi}^{(0)} \;\wedge\; \star\alpha^{(2)}, \qquad \forall\,\alpha^{(2)} \;\in\; \tilde{\Lambda}^{(3)}(\boldsymbol{\mathcal{M}}). \tag{6.27}$$

6.5.Discrete Weak Formulation

In the previous section, the test form used in the weak formulation of the linear momentum balance was the Hodge of an arbitrary form, $\star\eta^{(3)}$, belonging to the solution (dual) space of the equation. Since applying the Hodge maps this form to the space of primal 0-forms, which coincides with the space where the flow map is defined, the test function in the discrete setting is chosen as an arbitrary function from the same space as the flow map, i.e.$\tilde{\phi} \in H^1(\mathcal{B}\times T)$. Here, $\mathcal{B}\times T$ represents the discrete counterpart of the continuous space-time manifold, $\boldsymbol{\mathcal{M}}$. Note that the 'tilde' symbol over the test function indicates that the function is a test function, and it is not related to the dual representation.

$$\int_{\mathcal{B}\times T} \frac{\partial\boldsymbol{\pi}}{\partial t}\,\tilde{\phi} \;\; d(\mathcal{B}\times T) \;-\; \int_{\mathcal{B}\times T} (\nabla\cdot\boldsymbol{P})\,\tilde{\phi} \;\; d(\mathcal{B}\times T) \;=\; 0, \qquad \forall\,\tilde{\phi}\in H^1(\mathcal{B}\times T). \tag{6.28}$$

By switching the derivatives from the dual variable to the test function via integration by parts and the divergence theorem as,

$$\int_{\mathcal{B}\times T} \frac{\partial}{\partial t}(\boldsymbol{\pi}\,\tilde{\phi}) \;\; d(\mathcal{B}\times T) \;=\; \int_{\mathcal{B}\times T} \left(\frac{\partial\boldsymbol{\pi}}{\partial t}\tilde{\phi} + \boldsymbol{\pi}\frac{\partial\tilde{\phi}}{\partial t}\right) \;\; d(\mathcal{B}\times T),$$

$$\int_{\mathcal{B}\times T} \frac{\partial\boldsymbol{\pi}}{\partial t}\,\tilde{\phi} \;\; d(\mathcal{B}\times T) \;=\; -\int_{\mathcal{B}\times T} \boldsymbol{\pi}\,\frac{\partial\tilde{\phi}}{\partial t} \;\; d(\mathcal{B}\times T) + \int_{\mathcal{B}\times\partial T} (\boldsymbol{\pi}\cdot\boldsymbol{n}_t)\,\tilde{\phi} \;\; d(\mathcal{B}\times\partial T).$$

$$\int_{\mathcal{B}\times T} \frac{\partial\boldsymbol{\pi}}{\partial t}\,\tilde{\phi} \;\; d(\mathcal{B}\times T) \;=\; -\int_{\mathcal{B}\times T} \boldsymbol{\pi}\,\frac{\partial\tilde{\phi}}{\partial t} \;\; d(\mathcal{B}\times T) \;+\; \int_{\mathcal{B}\times\partial T} (\boldsymbol{\pi}\cdot\boldsymbol{n}_t)\,\tilde{\phi} \;\; d(\mathcal{B}\times\partial T). \tag{6.29}$$

Similarly,

$$\int_{\mathcal{B}\times T} \nabla\cdot(\boldsymbol{P}\,\tilde{\phi}) \;\; d(\mathcal{B}\times T) \;=\; \int_{\mathcal{B}\times T} \Big((\nabla\cdot\boldsymbol{P})\,\tilde{\phi} + \boldsymbol{P}\cdot\nabla\tilde{\phi}\Big) \;\; d(\mathcal{B}\times T),$$

$$\int_{\mathcal{B}\times T} (\nabla\cdot\boldsymbol{P})\,\tilde{\phi} \;\; d(\mathcal{B}\times T) \;=\; -\int_{\mathcal{B}\times T} \boldsymbol{P}\cdot\nabla\tilde{\phi} \;\; d(\mathcal{B}\times T) + \int_{\partial\mathcal{B}\times T} (\boldsymbol{P}\cdot\boldsymbol{n})\,\tilde{\phi} \;\; d(\partial\mathcal{B}\times T).$$

$$\int_{\mathcal{B}\times T} (\nabla\cdot\boldsymbol{P})\,\tilde{\phi} \;\; d(\mathcal{B}\times T) \;=\; -\int_{\mathcal{B}\times T} \boldsymbol{P}\cdot\nabla\tilde{\phi} \;\; d(\mathcal{B}\times T) \;+\; \int_{\partial\mathcal{B}\times T} (\boldsymbol{P}\cdot\boldsymbol{n})\,\tilde{\phi} \;\; d(\partial\mathcal{B}\times T). \tag{6.30}$$

Substituting the results obtained from equations 6.30 and 6.29 in equation 6.37, and further neglecting the spatial boundary integral, the discrete form of the linear momentum balance is obtained as,

$$-\int_{\mathcal{B}\times T} \boldsymbol{\pi}\frac{\partial\tilde{\phi}}{\partial t}\;\; d(\mathcal{B}\times T) \;+\; \int_{\mathcal{B}\times\partial T} (\boldsymbol{\pi}\cdot\boldsymbol{n_t})\,\tilde{\phi}\;\; d(\mathcal{B}\times\partial T) \;+\; \int_{\mathcal{B}\times T} \boldsymbol{P}\cdot\nabla\tilde{\phi}\;\; d(\mathcal{B}\times T) \;=\; 0. \tag{6.31}$$

In this form, all derivatives are transferred to the test functions. From the definition of the first Piola-Kirchhoff stress tensor, $\boldsymbol{P} = P_W J\boldsymbol{F}^{-T}$, and by denoting the gradient of the test function $\boldsymbol{\nabla}\tilde{\phi}$ as $\tilde{\boldsymbol{F}}$, the above equation can be expressed in inner product notation as follows:

$$-\left(\boldsymbol{\pi}\,,\frac{\partial\tilde{\phi}}{\partial t}\right)_{\mathcal{B}\times T} + \left(\boldsymbol{\pi}\cdot\boldsymbol{n_t}\,,\tilde{\phi}\right)_{\mathcal{B}\times\partial T} + \left(P_W J\boldsymbol{F}^{-T}\,\boldsymbol{:}\,\tilde{\boldsymbol{F}}\right)_{\mathcal{B}\times T} \;=\; 0. \tag{6.32}$$

Here, the colon (:) denotes the component-wise product of two tensors, so $A : B = \sum_{i,j} A_{ij}B_{ij}$, further the first and second terms are fairly straightforward since they involve the inner product of primal and dual basis which are orthogonal to each other and lead to Kronecker delta upon taking the inner product (note that in the trace space of $\boldsymbol{\pi}$, their basis functions are orthogonal to the basis of $\tilde{\phi}$) and thus leaving just degrees of freedom. The interesting term is the third term which involves basis functions from the same space thereby leading to a Hodge matrix as follows:

$$\left(P_W J\boldsymbol{F}_x^{-T}\,\boldsymbol{:}\,\tilde{\boldsymbol{F}}_x\right)_{\mathcal{B}\times T} \;=\; \boldsymbol{\phi}_x^T\;\mathbb{E}_x^{1,0^T}\;\mathbb{H}_{P_w}\,\mathbb{E}_y^{1,0}\,\bar{\boldsymbol{\varphi}}_y \;-\; \boldsymbol{\phi}_x^T\;\mathbb{E}_y^{1,0^T}\;\mathbb{H}_{P_w}\,\mathbb{E}_x^{1,0}\,\bar{\boldsymbol{\varphi}}_y.$$

$$\left(P_W J\boldsymbol{F}_y^{-T}\,\boldsymbol{:}\,\tilde{\boldsymbol{F}}_y\right)_{\mathcal{B}\times T} \;=\; -\,\boldsymbol{\phi}_y^T\;\mathbb{E}_x^{1,0^T}\;\mathbb{H}_{P_w}\,\mathbb{E}_y^{1,0}\,\bar{\boldsymbol{\varphi}}_x \;+\; \boldsymbol{\phi}_y^T\;\mathbb{E}_y^{1,0^T}\;\mathbb{H}_{P_w}\,\mathbb{E}_x^{1,0}\,\bar{\boldsymbol{\varphi}}_x. \tag{6.33}$$

Substituting the above results in equation 6.32, and writing the remaining terms as well in terms of the degrees of freedom, the final discrete equation for the linear momentum balance is obtained as:

$$\boldsymbol{\phi}_x^T\,\mathbb{E}^{1,0^T}\tilde{\boldsymbol{\pi}}_x + \;\boldsymbol{\phi}_x^T\,\mathbb{N}_\pi\hat{\boldsymbol{\pi}}_x \;-\; \boldsymbol{\phi}_x^T\;\mathbb{E}_x^{1,0^T}\;\mathbb{H}_{P_w}\,\mathbb{E}_y^{1,0}\,\bar{\boldsymbol{\varphi}}_y \;+\; \boldsymbol{\phi}_x^T\;\mathbb{E}_y^{1,0^T}\;\mathbb{H}_{P_w}\,\mathbb{E}_x^{1,0}\,\bar{\boldsymbol{\varphi}}_y \;=\; 0. \tag{6.34}$$

$$\boldsymbol{\phi}_y^T\,\mathbb{E}^{1,0^T}\tilde{\boldsymbol{\pi}}_y + \;\boldsymbol{\phi}_y^T\,\mathbb{N}_\pi\hat{\boldsymbol{\pi}}_y \;+\; \boldsymbol{\phi}_y^T\;\mathbb{E}_x^{1,0^T}\;\mathbb{H}_{P_w}\,\mathbb{E}_y^{1,0}\,\bar{\boldsymbol{\varphi}}_x \;-\; \boldsymbol{\phi}_y^T\;\mathbb{E}_y^{1,0^T}\;\mathbb{H}_{P_w}\,\mathbb{E}_x^{1,0}\,\bar{\boldsymbol{\varphi}}_x \;=\; 0. \tag{6.35}$$

Here, the matrix $\mathbb{N}_\pi$ is the connectivity matrix which maps the temporal boundary degrees of freedom of the momentum to the equation behaving as a trace matrix. Further for any arbitrary test function the above equations reduce to,

$$\begin{aligned}
&\mathbb{E}^{1,0^T}\bar{\boldsymbol{\pi}}_x + \;\mathbb{N}_\pi\hat{\boldsymbol{\pi}}_x \;-\; \mathbb{E}_x^{1,0^T}\;\mathbb{H}_{P_w}\,\mathbb{E}_y^{1,0}\,\bar{\boldsymbol{\varphi}}_y \;+\; \mathbb{E}_y^{1,0^T}\;\mathbb{H}_{P_w}\,\mathbb{E}_x^{1,0}\,\bar{\boldsymbol{\varphi}}_y = 0.\\
&\mathbb{E}^{1,0^T}\bar{\boldsymbol{\pi}}_y + \;\mathbb{N}_\pi\hat{\boldsymbol{\pi}}_y \;+\; \mathbb{E}_x^{1,0^T}\;\mathbb{H}_{P_w}\,\mathbb{E}_y^{1,0}\,\bar{\boldsymbol{\varphi}}_x \;-\; \mathbb{E}_y^{1,0^T}\;\mathbb{H}_{P_w}\,\mathbb{E}_x^{1,0}\,\bar{\boldsymbol{\varphi}}_x = 0.
\end{aligned} \tag{6.36}$$

In a similar fashion, the discrete weak form of the constitutive equation is obtained by testing it with an arbitrary function $\tilde{\boldsymbol{v}} \in H(grad\,;\mathcal{B}\times T)$ belonging to the space where the velocity is defined.

$$\int_{\mathcal{B}\times T} \boldsymbol{\pi}\;\tilde{\boldsymbol{v}}\;\; d(\mathcal{B}\times T) \;-\; \int_{\mathcal{B}\times T} \rho_o\frac{\partial\varphi}{\partial t}\;\tilde{\boldsymbol{v}}\;\; d(\mathcal{B}\times T) \;=\; 0, \qquad \forall\,\tilde{\boldsymbol{v}}\in H^1(grad\,;\mathcal{B}\times T). \tag{6.37}$$

$$\tilde{\boldsymbol{v}}^T\bar{\boldsymbol{\pi}} \;-\; \tilde{\boldsymbol{v}}^T\left[\;\rho_o\int_{\mathcal{B}\times T}(\Psi_1^\tau)^T\;\Psi_1^\tau\;\; d(\mathcal{B}\times T)\;\right]\;\mathbb{E}_t^{(1,0)}\,\bar{\boldsymbol{\varphi}} \;=\; 0. \tag{6.38}$$

The integral within the square brackets is the density Hodge matrix and is denoted as $\mathbb{H}_{\rho_o}$, which maps primal temporal edge DOFs of the velocity to the dual spatial surface DOFs of the momentum, thus the full discrete form of the momentum constitutive equation can be obtained as :

$$\begin{aligned} \mathbb{H}_{\rho_o}^{-1}\bar{\boldsymbol{\pi}}_x \;-\; \mathbb{E}_t^{1,0}\bar{\boldsymbol{\varphi}}_x \;&=\; 0 \\ \mathbb{H}_{\rho_o}^{-1}\bar{\boldsymbol{\pi}}_y \;-\; \mathbb{E}_t^{1,0}\bar{\boldsymbol{\varphi}}_y \;&=\; 0 \end{aligned} \tag{6.39}$$

The equations in 6.36 and 6.39 can be assembled into a final matrix form system of equations as:

$$\begin{bmatrix} \mathbb{H}_{\rho_0}^{-1} & 0 & -\mathbb{E}_t^{1,0} & 0 & 0 & 0 \\ 0 & \mathbb{H}_{\rho_0}^{-1} & 0 & -\mathbb{E}_t^{1,0} & 0 & 0 \\ \mathbb{E}_t^{1,0^T} & 0 & 0 & -\mathbb{D}_{PK} & \mathbb{N}_\pi & 0 \\ 0 & \mathbb{E}_t^{1,0^T} & \mathbb{D}_{PK} & 0 & 0 & \mathbb{N}_\pi \end{bmatrix} \begin{bmatrix} \bar{\boldsymbol{\pi}}_x \\ \bar{\boldsymbol{\pi}}_y \\ \bar{\boldsymbol{\varphi}}_x \\ \bar{\boldsymbol{\varphi}}_y \\ \hat{\boldsymbol{\pi}}_x \\ \hat{\boldsymbol{\pi}}_y \end{bmatrix} = \begin{bmatrix} 0 \\ 0 \\ 0 \\ 0 \end{bmatrix}. \tag{6.40}$$

where $\mathbb{D}_{PK} = \mathbb{E}_x^{1,0^T}\,\mathbb{H}_{P_w}\,\mathbb{E}_y^{1,0} \;-\; \mathbb{E}_y^{1,0^T}\,\mathbb{H}_{P_w}\,\mathbb{E}_x^{1,0}$, to simplify the matrix representation.

6.5.1. Initial Conditions and Time stacking

As of now the system matrix defined above is not a square system, the reduction of the matrix is done via the prescription of initial conditions. Firstly the initial momentum is prescribed in a strong sense by multiplying the respective columns with the known initial degrees of freedom of the momentum $\hat{\pi}_x^{t_o}$ and $\hat{\pi}_y^{t_o}$ at the initial time level and taking it over to the right hand side. Next the flow map φ at the initial time level, $\varphi(\mathbf{X}, t_0)$, is prescribed by adding an extra set of equations rather than by eliminating the associated degrees of freedom by directly setting $\varphi(\mathbf{X}, t_0) = \mathbf{X}$. This as mentioned before, introduces an additional constraint equation of the form

$$\int_{\mathcal{B}\times T_o} \boldsymbol{\lambda}\Big[\varphi(\mathbf{x}, t_0) - \varphi_o\Big]\, d(\mathcal{B}\times T_0) = 0, \tag{6.41}$$

where $\boldsymbol{\lambda}$ is a Lagrange multiplier field. In the discrete setting, this approach augments the global system with extra unknowns (the components of $\boldsymbol{\lambda}$), while the coupling to the flow map φ is typically realized through a connectivity matrix such as $\mathbb{N}_\pi^T$.

From a Hamiltonian perspective, the Lagrange multiplier enforcing a constraint on position (in this case, the flow map) can be interpreted as the conjugate momentum. Imposing the condition $\varphi(\mathbf{X}, t_0) = \mathbf{X}$ in a weak sense guarantees that the reaction force (encoded in the multiplier $\boldsymbol{\lambda}$) enforces the initial positioning of each material point. When the fully time-stacked system is solved, these additional unknowns $\boldsymbol{\lambda}$ naturally appear in the solution vector at the final time level. In other words, the multiplier associated with enforcing the flow map acts as the momentum at the next (or final) time level [40].

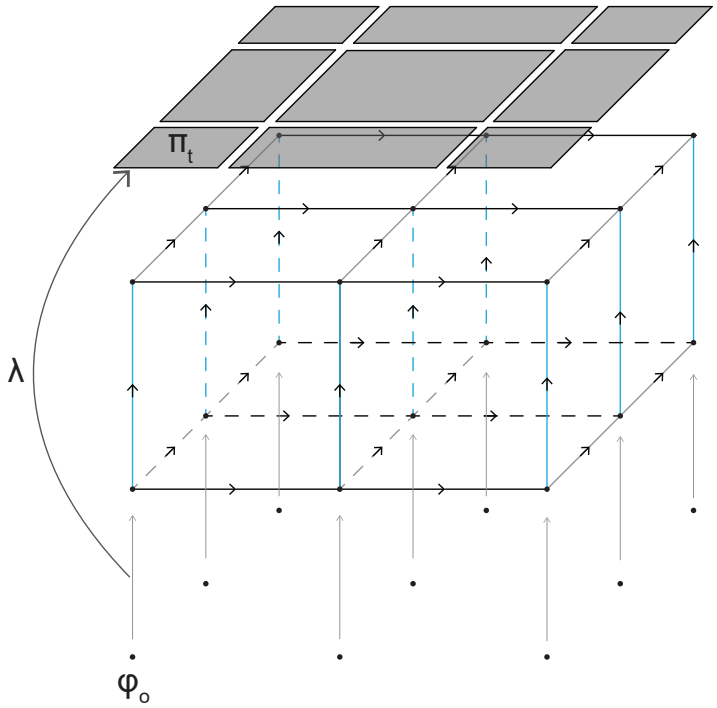

Figure 6.5: Prescription of initial flow map

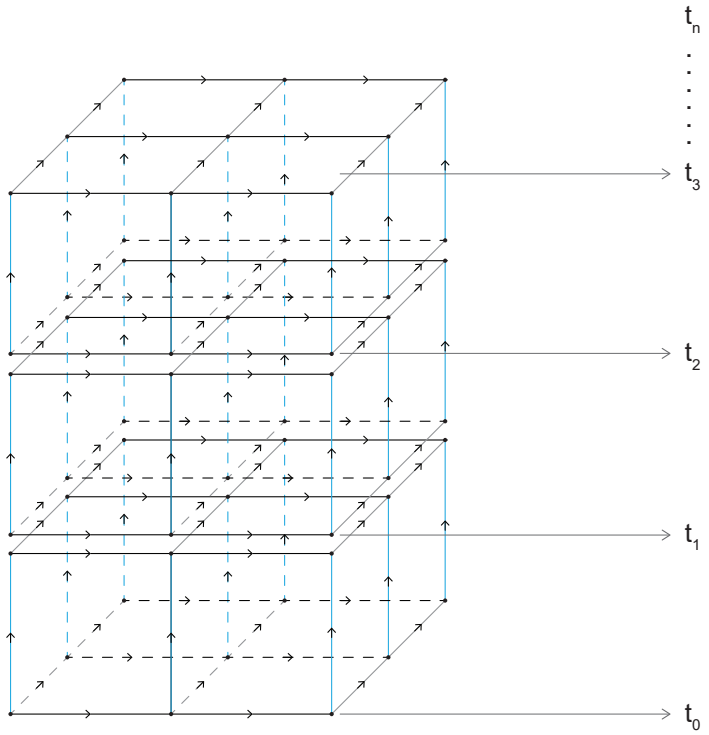

Figure 6.6: Time stacking

Next, the time stepping proceeds by stacking the space-time grids (treated as single spectral elements) sequentially in time. The computed flow map and momentum at the final time level of one element are then prescribed as the initial conditions for the subsequent time element in the same way as explained above. Thus incorporating the above discussed initial conditions results in complete square matrix form of the discrete system of equations for a single time interval spectral grid describing the Lagrangian barortropic flow as shown below.

$$\begin{bmatrix} \mathbb{H}_{\rho_0}^{-1} & 0 & -\mathbb{E}_t^{1,0} & 0 & 0 & 0 \\ 0 & \mathbb{H}_{\rho_0}^{-1} & 0 & -\mathbb{E}_t^{1,0} & 0 & 0 \\ \mathbb{E}_t^{1,0^T} & 0 & 0 & -\mathbb{D}_{PK} & -\mathbb{N}_\pi^t & 0 \\ 0 & \mathbb{E}_t^{1,0^T} & \mathbb{D}_{PK} & 0 & 0 & -\mathbb{N}_\pi^t \\ 0 & 0 & \mathbb{N}_\pi^{t_o\ T} & 0 & 0 & 0 \\ 0 & 0 & 0 & \mathbb{N}_\pi^{t_0\ T} & 0 & 0 \end{bmatrix} \begin{bmatrix} \bar{\boldsymbol{\pi}}_x \\ \bar{\boldsymbol{\pi}}_y \\ \bar{\boldsymbol{\varphi}}_x \\ \bar{\boldsymbol{\varphi}}_y \\ \hat{\boldsymbol{\pi}}_x^t \\ \hat{\boldsymbol{\pi}}_y^t \end{bmatrix} = \begin{bmatrix} 0 \\ 0 \\ -\mathbb{N}^{t_o} \hat{\boldsymbol{\pi}}_x^{t_o} \\ -\mathbb{N}^{t_o} \hat{\boldsymbol{\pi}}_y^{t_o} \\ \varphi_{x_o} \\ \varphi_{y_o} \end{bmatrix}. \tag{6.42}$$

6.5.2. Pressure Hodge Matrix Non-linearity

The weak form described of the *pressure Hodge matrix* $\mathbb{H}_{P_w}$, in the previous section yields an integral expression

$$P_w(\rho_0, J) \int_{\mathcal{B}\times T} \left(\Psi_1^\xi\right)^T \Psi_1^\eta \, d(\mathcal{B}\times T).$$

which, maps the primal (edge) degrees of freedom of the deformation gradient $\boldsymbol{F}$ to the dual (surface) degrees of freedom corresponding to the Piola–Kirchhoff stress. The term $P_w(\rho_0, J)$ serves as a spatial and temporal weight, where ρ_0 is the reference density and $J = \det(\mathbf{F})$ depends on the solution φ via $\mathbf{F} = \nabla\varphi$.

Since $P_w(\rho_0, J)$ depends on J, and thus on φ, the matrix $\mathbb{H}_{P_w}$ becomes nonlinear in the solution. This nonlinearity is handled through a **Picard** (fixed-point) iteration. The procedure begins with an initialization step, where a suitable initial guess $\varphi^{(0)}$ is chosen. A typical choice is the converged solution from the previous time step or the initial conditions at the start of the solve.

Once the iteration starts, the deformation gradient $\mathbf{F}^{(k)}$ is computed from the current estimate $\varphi^{(k)}$, and its determinant $J^{(k)}$ is evaluated. The pressure weight $P_w(\rho_0, J^{(k)})$ is then updated to reflect the current values of $J^{(k)}$. The pressure Hodge matrix $\mathbb{H}_{P_w}$ is reassembled accordingly, so that the new weight is integrated alongside the basis functions using the quadrature weights. With this updated matrix, the system is solved for a new flowmap, $\varphi^{(k+1)}$.

A convergence check is performed by comparing the trace of $\mathbf{F}^{(k+1)}$ and $J^{(k+1)}$ against those from the previous iteration. The iteration continues until these values fall below a specified tolerance, indicating that the solution has converged with the consistent dependence of P_w on J. The final φ and its corresponding $\mathbf{F}$ are then used as an initial guess for the next time step.

6.6.Conservation of Linear Momentum

To check that *total* linear momentum is conserved, a test function that represents a rigid-body *translation* of the flow map is chosen, for instance

$$\tilde{\phi}(\mathbf{x}, t) \;=\; \mathbf{c},$$

where $\mathbf{c}$ is a constant vector (e.g., $\mathbf{c} = (1,0)^T$ or $(0,1)^T$ in 2D). Substituting $\tilde{\phi} = \mathbf{c}$ into the weak form leads to

$$-\int_{\mathcal{B}\times T} \boldsymbol{\pi} \frac{\partial c}{\partial t} \;\; d(\mathcal{B}\times T) \;+\; \int_{\mathcal{B}\times \partial T} (\boldsymbol{\pi}\cdot \boldsymbol{n}_t)\, c \;\; d(\mathcal{B}\times \partial T) \;+\; \int_{\mathcal{B}\times T} \boldsymbol{P}\cdot\nabla c \;\; d(\mathcal{B}\times T) \;=\; 0. \tag{6.43}$$

Because $\mathbf{c}$ is constant, $\nabla\mathbf{c} = \mathbf{0}$ and $\frac{\partial c}{\partial t} = 0$, so the first and the third term (stress) vanishes, leading to :

$$\left(c \int_{\mathcal{B}} \boldsymbol{\pi} \, d\mathcal{B} \right)_{t=0} = \left(c \int_{\mathcal{B}} \boldsymbol{\pi} \, d\mathcal{B} \right)_{t=T} \tag{6.44}$$

The above relation shows that the linear momentum at the start of the time step is equal to the linear momentum at the end of the time step, in other words the net integral rate of change of linear momentum is zero, implying the *total* linear momentum of the system is constant in time. If no external body forces or tractions act on the domain, there is no source of net momentum gain or loss, so the integral of $\boldsymbol{\pi}$ over the domain cannot change. Hence, the system conserves linear momentum.

6.7.Conservation of Angular Momentum

To check if the angular momentum is conserved in the above discussed formulation, The weak form of the linear momentum balance equation derived in the previous sections is considered.

$$- \int_{\mathcal{B}\times T} \boldsymbol{\pi} \frac{\partial \tilde{\phi}}{\partial t} \; d(\mathcal{B}\times T) \; + \int_{\mathcal{B}\times \partial T} (\boldsymbol{\pi}\cdot \boldsymbol{n}_t)\, \tilde{\phi} \; d(\mathcal{B}\times \partial T) \; + \int_{\mathcal{B}\times T} \boldsymbol{P}\cdot \nabla \tilde{\phi} \; d(\mathcal{B}\times T) \; = \; 0. \tag{6.45}$$

Since the choice of the test function is arbitrary since the momentum equation should hold for all variations, thus choosing a test function corresponding to a rotation of the flow map.

$$\tilde{\phi} \; = \; \begin{bmatrix} \varphi_y \\ -\varphi_x \end{bmatrix}. \tag{6.46}$$

The term $\boldsymbol{P} : \nabla \tilde{\phi}$ involves the product $P_W \, J \, \mathbf{F}^{-T}$ and the gradient of $\tilde{\phi}$. When the specific rotated test function is inserted,

$$\nabla \tilde{\phi} \; = \; \begin{bmatrix} \partial(\varphi_y)/\partial x & \partial(\varphi_y)/\partial y \\ \partial(-\varphi_x)/\partial x & \partial(-\varphi_x)/\partial y \end{bmatrix},$$

substituting this in the inner the product representation,

$$\left(P_W \begin{bmatrix} F_{yy} & -F_{yx} \\ -F_{xy} & F_{xx} \end{bmatrix} : \begin{bmatrix} F_{yx} & F_{yy} \\ -F_{xx} & -F_{xy} \end{bmatrix} \right)_{\mathcal{B}\times T}$$

Further expanding the inner product components,

$$\int_{\mathcal{B}\times T} P_W \; (\cancel{F_{yy}\, F_{yx}} \; - \; \cancel{F_{yx}\, F_{yy}} \; + \; \cancel{F_{xy}\, F_{xx}} \; - \; \cancel{F_{xx}\, F_{xy}} \;) \; d(\mathcal{B}\times T) \; = \; 0 \tag{6.47}$$

By using the skew-symmetric structure imposed by $\tilde{\phi} = [\varphi_y, -\varphi_x]$, the net contribution simplifies in such a way that the integrated effect of $\nabla \cdot \boldsymbol{P}$ against the rotation of φ *vanishes* as shown above. This leads to the remaining term

$$\int_B (\pi_x \varphi_y - \pi_y \varphi_x)\big|_{t=0}^{t=T} \; d\mathcal{B} \; + \; \int_0^T \int_B \left(\pi_x \dot{\varphi}_y - \pi_y \dot{\varphi}_x\right) d\mathcal{B}\, dt \; = \; 0. \tag{6.48}$$

Further the discrete momentum-velocity relationship is given by $\pi_x = \mathbb{H}_{\rho_o}^{-1} \dot{\varphi}_x$ and $\pi_y = \mathbb{H}_{\rho_o}^{-1} \dot{\varphi}_y$, inserting this in the above expression,

$$\int_B (\pi_x \varphi_y - \pi_y \varphi_x)\big|_{t=0}^{t=T} \; d\mathcal{B} \; + \; \cancel{\dot{\varphi}_y^T \, \mathbb{H}_{\rho_o}^{-1} \, \dot{\varphi}_x} \; - \cancel{\dot{\varphi}_x^T \, \mathbb{H}_{\rho_o}^{-1} \, \dot{\varphi}_y} \; = \; 0. \tag{6.49}$$

$$\left(\int_B (\pi_x\varphi_y - \pi_y\varphi_x)\ d\mathcal{B}\right)_{t=0} = \left(\int_B (\pi_x\varphi_y - \pi_y\varphi_x)\ d\mathcal{B}\right)_{t=T} \tag{6.50}$$

The above equation shows that if the system starts with a certain amount of angular momentum, and no external torques act upon it, the angular momentum remains fixed in time.

6.8.Conservation of Energy

Conservation of energy can be shown by taking the material velocity evaluated at the primal nodes as the choice of test function $\tilde{\phi} = \frac{\partial\varphi}{\partial t} = \dot{\varphi}$, which is the time derivative of the flow map.

$$\int_{\mathcal{B}\times T} \boldsymbol{\pi}\ \frac{\partial\dot{\varphi}}{\partial t}\ d(\mathcal{B}\times T)\ -\ \int_{\mathcal{B}\times T} \big(\nabla\cdot\boldsymbol{P}\big)\cdot\dot{\varphi}\ d(\mathcal{B}\times T)\ =\ 0. \tag{6.51}$$

Since $\boldsymbol{\pi} = \rho_0\,\frac{\partial\varphi}{\partial t}$, the first integral can be written as

$$\int_{\mathcal{B}\times T} \frac{\partial}{\partial t}\Big(\frac{\partial\varphi}{\partial t}\Big)\cdot\rho_0\,\frac{\partial\varphi}{\partial t}\ d(\mathcal{B}\times T),$$

this expression simplifies to $\rho_0\ \dfrac{\partial^2\varphi}{\partial t^2}\ \cdot\ \dfrac{\partial\varphi}{\partial t}$. Further considering the scalar product and applying the product rule and rearranging,

$$\frac{\partial}{\partial t}\left(\frac{\partial\varphi}{\partial t}\ \cdot\ \frac{\partial\varphi}{\partial t}\right)\ =\ 2\left(\frac{\partial^2\varphi}{\partial t^2}\ \cdot\ \frac{\partial\varphi}{\partial t}\right),$$

$$\frac{\partial^2\varphi}{\partial t^2}\ \cdot\ \frac{\partial\varphi}{\partial t}\ =\ \tfrac{1}{2}\,\frac{\partial}{\partial t}\Big(\frac{\partial\varphi}{\partial t}\ \cdot\ \frac{\partial\varphi}{\partial t}\Big).$$

Hence, the original integral, can be rewritten as,

$$\int_{\mathcal{B}\times T} \rho_0\,\frac{1}{2}\,\frac{\partial}{\partial t}\Big(\frac{\partial\varphi}{\partial t}\ \cdot\ \frac{\partial\varphi}{\partial t}\Big)\ d(\mathcal{B}\times T)\ =\ \int_{\mathcal{B}\times T} \frac{\partial}{\partial t}\left(\frac{1}{2}\rho_o\left\|\tfrac{\partial\varphi}{\partial t}\right\|^2\right)\ d(\mathcal{B}\times T) \tag{6.52}$$

which is precisely the integral of the rate of change of the (kinetic) energy density in the material configuration (assuming that ρ_0 is constant and $\mathcal{B}$ is the reference domain).

Considering the second integral, upon transferring the derivative via integration parts and neglecting the boundary integral yields,

$$-\int_{\mathcal{B}\times T} \big(\nabla\cdot\boldsymbol{P}\big)\cdot\frac{\partial\varphi}{\partial t}\ d(\mathcal{B}\times T) = \int_{\mathcal{B}\times T} \boldsymbol{P}:\nabla\Big(\frac{\partial\varphi}{\partial t}\Big)\ d(\mathcal{B}\times T)\ =\ \int_{\mathcal{B}\times T} \boldsymbol{P}:\frac{\partial}{\partial t}\big(\nabla\varphi\big)\ d(\mathcal{B}\times T).$$

For an inviscid barotropic assumption, the first piola-kirchoff stress tensor can be written as the the derivative of the internal energy with respect to deformation gradient, this gives [22, 25]

$$\boldsymbol{P}:\dot{\boldsymbol{F}}\ =\ \frac{\partial W}{\partial\boldsymbol{F}}:\dot{\boldsymbol{F}}\ =\ \frac{\partial}{\partial t}W(\boldsymbol{F}),$$

where $W(\boldsymbol{F})$ is the internal-energy density. Combining the integrals back,

$$\int_{\mathcal{B}\times T} \frac{\partial}{\partial t}\Bigg(\underbrace{\frac{1}{2}\rho_0\Big\|\frac{\partial\varphi}{\partial t}\Big\|^2}_{\text{Kinetic Energy}} + \underbrace{W(\boldsymbol{F})}_{\text{Internal Energy}}\Bigg)\ d(\mathcal{B}\times T) = 0. \tag{6.53}$$

Hence, the sum of the kinetic and internal (potential) energies remains constant in time, demonstrating conservation of mechanical energy in the discrete Lagrangian formulation. Boundary or external force terms, if present, would appear on the right-hand side and represent energy input or output, yielding an energy balance rather than strict conservation.

Finally, in the discrete system (as described in the momentum weak form), selecting the velocity (or partial derivative of the flow map) evaluated at nodes as the test function and taking the inner product with the discrete matrices, leads to the same integral identities.

6.8.1. Relation to Noether's Theorem

The preceding discussion of Noether's theorem in the previous chapter, highlighted how continuous symmetries of the Lagrangian give rise to conserved quantities, including energy, linear momentum, and angular momentum. According to Noether's theorem, small shifts in time, space, or coordinate rotations leave the action unchanged, which translates into the conservation of energy, linear momentum, and angular momentum at the continuous level.

In the discrete or weak formulations for the barotropic fluid, these same conservations are enforced through specific choices of test functions. For angular momentum, selecting a rotational test function ensures no net torque arises from the internal stress. For linear momentum, a translational test function demonstrates the absence of net force on the domain, implying constant total momentum. For energy, multiplying the momentum equation by the velocity (or partial derivative of the flow map) isolates the kinetic and potential contributions, revealing that their sum is constant unless there is external work or boundary traction.

Verifying these properties through weak-form checks therefore mirrors the symmetries identified by Noether's theorem in the continuum theory. When the boundary conditions are properly handled and external forcing is absent, the integral forms of the momentum and energy equations confirm that no momentum or energy is lost or gained. This consistency between the continuous geometric invariants and their discrete counterparts not only validates the numerical approach but also promotes stable and accurate simulations over time.

6.9.Multisymplectic Nature of the Discretization

Symplectic geometry arises naturally in systems governed by Hamiltonian equations, where a single time variable drives the evolution of generalized coordinates . In that setting, equations of motion can be expressed using a skew-symmetric matrix, frequently denoted J, that encodes the conservation of a certain geometric "area" (or higher-dimensional volume) in phase space [4, 8].

For partial differential equations (PDEs), that is equations in which the Lagrangian (thereby the associated Hamiltonian) depends both on the derivatives in space and time, instead of conventional Hamiltonian differential equations (ODEs), multiple spatial coordinates and time typically appear [1, 2]. A direct Legendre transform that only accounts for time derivatives may obscure key structure in the spatial derivatives. Multi-symplectic theory addresses this gap by introducing several skew-symmetric operators, one for each unbounded coordinate (including time), as in [12]. In a setting with one spatial dimension x and time t, the PDE might be expressed as

$$M(z)\,\frac{\partial z}{\partial t} \;+\; K(z)\,\frac{\partial z}{\partial x} \;=\; \nabla S(z),$$

where z describes the necessary variables (such as displacement and velocity), and S plays a role similar to a Hamiltonian potential [2, 12]. The operators M and K are skew-symmetric and generalize the single-operator scenario encountered in classical Hamiltonian systems .

A multi-symplectic framework uses multiple symplectic forms, one for each independent variable, so both space and time derivatives appear symmetrically. This framework generalizes classical symplectic geometry from time-only Hamiltonian dynamics to PDEs with additional coordinates [12, 17]. The approach ensures that contributions from each spatial direction are placed on the same geometric footing as contributions from time.

In conclusion, multi-symplectic theory extends the single-time Hamiltonian idea to PDEs involving multiple coordinates. Each coordinate, including time, is accompanied by a skew-symmetric operator that generalizes the concept of symplectic geometry [12]. The resulting framework highlights geometric invariants and clarifies the interplay of space and time in conservation laws. This perspective has proven advantageous for studying dispersive equations, free-surface fluid models, and other engineering applications [1, 12].

6.9.1. Multisymplectic Formulation of the Barotropic Fluid Equations

As stated previously PDE system in two spatial dimensions is said to possess a multisymplectic structure if it can be written in the form

$$\mathbf{M}\,\frac{\partial Z}{\partial t} \;+\; \mathbf{K}\,\frac{\partial Z}{\partial X} \;+\; \mathbf{L}\,\frac{\partial Z}{\partial Y} \;=\; \nabla_Z\, H(Z), \tag{6.54}$$

where Z is a vector of state variables, and $\mathbf{M}, \mathbf{K}, \mathbf{L}$ are constant skew-symmetric matrices. The function $H(Z)$ is a Hamiltonian, and the intention here is to demonstrate that the barotropic fluid equations can indeed be expressed in this framework, allowing the equations to be obtained directly from the multi-symplectic form.

The Hamiltonian for the barotropic fluid as obtained in the previous sections (neglecting gravity) is,

$$H(Z) \;=\; \frac{1}{2\,\rho_0}\,\|\boldsymbol{\pi}\|^2 \;+\; \rho_0\,U\big(\rho_0,\; J\big) \tag{6.55}$$

where $U(\rho_0, J)$ is an internal energy function and $\Pi(\varphi)$ represents potential energy contributions from an external field and Z is vector of the associated canonical varibles,

$$Z \;=\; \begin{pmatrix} \varphi \\ \boldsymbol{\pi} \\ \boldsymbol{F}_x \\ \boldsymbol{F}_y \end{pmatrix} \;=\; \big(\varphi_x,\; \varphi_y,\; \pi_x,\; \pi_y,\; F_{xx},\; F_{yx},\; F_{xy},\; F_{yy}\big)^T,$$

Multisymplectic matrices. In two spatial dimensions, Z has eight components. As a result, $\mathbf{M}, \mathbf{K}, \mathbf{L}$ become 8×8 skew-symmetric block matrices of the form

$$\mathbf{M} = \begin{pmatrix} \mathbf{0} & -\mathbf{I} & \mathbf{0} & \mathbf{0} \\ \mathbf{I} & \mathbf{0} & \mathbf{0} & \mathbf{0} \\ \mathbf{0} & \mathbf{0} & \mathbf{0} & \mathbf{0} \\ \mathbf{0} & \mathbf{0} & \mathbf{0} & \mathbf{0} \end{pmatrix}, \quad \mathbf{K} = \begin{pmatrix} \mathbf{0} & \mathbf{0} & -\mathbf{I} & \mathbf{0} \\ \mathbf{0} & \mathbf{0} & \mathbf{0} & \mathbf{0} \\ \mathbf{I} & \mathbf{0} & \mathbf{0} & \mathbf{0} \\ \mathbf{0} & \mathbf{0} & \mathbf{0} & \mathbf{0} \end{pmatrix}, \quad \mathbf{L} = \begin{pmatrix} \mathbf{0} & \mathbf{0} & \mathbf{0} & -\mathbf{I} \\ \mathbf{0} & \mathbf{0} & \mathbf{0} & \mathbf{0} \\ \mathbf{0} & \mathbf{0} & \mathbf{0} & \mathbf{0} \\ \mathbf{I} & \mathbf{0} & \mathbf{0} & \mathbf{0} \end{pmatrix}, \tag{6.56}$$

acting on the blocks $(\varphi, \boldsymbol{\pi}, \boldsymbol{F}_x, \boldsymbol{F}_y)$ with the RHS,

$$\nabla_Z\, H(Z) \;=\; \left[\frac{\partial H}{\partial \varphi},\, \frac{\partial H}{\partial \boldsymbol{\pi}},\, \frac{\partial H}{\partial \boldsymbol{F}_x},\, \frac{\partial H}{\partial \boldsymbol{F}_y}\right]^T.$$

Now, considering each row of the matrices shown above leads to the definition of the PDEs involved in the system. In the second row-block of $\mathbf{M}$, the entry $(\mathbf{I}, \mathbf{0}, \mathbf{0}, \mathbf{0})$ acting on $\frac{\partial Z}{\partial t}$ contributes $\frac{\partial}{\partial t}(\varphi_x, \varphi_y)$ on the left-hand side of (6.54). On the right-hand side, the derivative of H with respect to (π_x, π_y) is $\frac{1}{\rho_0}(\pi_x, \pi_y)$. Equating these terms implies:

$$\frac{\partial}{\partial t}\begin{pmatrix} \varphi_x \\ \varphi_y \end{pmatrix} \;=\; \begin{pmatrix} \dfrac{\pi_x}{\rho_0} \\ \dfrac{\pi_y}{\rho_0} \end{pmatrix}, \quad \dot{\varphi}_x = \frac{\pi_x}{\rho_0}, \quad \dot{\varphi}_y = \frac{\pi_y}{\rho_0}. \tag{6.57}$$

In the third and fourth block rows of $\mathbf{K}$ and $\mathbf{L}$. The rows corresponding to (F_{xx}, F_{yx}) in $\mathbf{K}$ and (F_{xy}, F_{yy}) in $\mathbf{L}$ lead to

$$\frac{\partial}{\partial X}\begin{pmatrix} \varphi_x \\ \varphi_y \end{pmatrix} \;=\; \begin{pmatrix} \dfrac{\partial H}{\partial F_{xx}} \\ \dfrac{\partial H}{\partial F_{yx}} \end{pmatrix}, \qquad \frac{\partial}{\partial Y}\begin{pmatrix} \varphi_x \\ \varphi_y \end{pmatrix} \;=\; \begin{pmatrix} \dfrac{\partial H}{\partial F_{xy}} \\ \dfrac{\partial H}{\partial F_{yy}} \end{pmatrix}. \tag{6.58}$$

Since H depends on $\boldsymbol{F}_x$ and $\boldsymbol{F}_y$ only through $J = \det(\mathbf{F})$, computing these derivatives identifies them with components of the first Piola–Kirchhoff stress. For instance,

$$\frac{\partial H}{\partial \boldsymbol{F}_x} \;=\; \rho_0 \,\frac{\partial U}{\partial J}\,\frac{\partial J}{\partial \boldsymbol{F}_x} \;=\; -\,P_W\,\frac{\partial J}{\partial \boldsymbol{F}_x}, \quad P_W := -\,\rho_0\,\frac{\partial U}{\partial J}.$$

By using the Jacobi's formula,

$$\frac{\partial H}{\partial \boldsymbol{F}_x} \;=\; -\,P_W\,J\,(\mathbf{F}^{-T})_x, \qquad \frac{\partial H}{\partial \boldsymbol{F}_y} \;=\; -\,P_W\,J\,(\mathbf{F}^{-T})_y.$$

The top row-block in all three matrices $\mathbf{M}, \mathbf{K}, \mathbf{L}$ together produces

$$-\,\frac{\partial}{\partial t}\begin{pmatrix}\pi_x\\ \pi_y\end{pmatrix} \;-\; \frac{\partial}{\partial X}\begin{pmatrix}F_{xx}\\ F_{yx}\end{pmatrix} \;-\; \frac{\partial}{\partial Y}\begin{pmatrix}F_{xy}\\ F_{yy}\end{pmatrix} \;=\; \frac{\partial H}{\partial \varphi} \;=\; 0 \quad \big(\text{since } H \text{ has no explicit } \varphi\text{-dependence}\big).$$

Substitution of the stress derivatives from above and collecting terms yields the standard momentum equation for a barotropic fluid in Lagrangian form:

$$\rho_0\,\ddot{\varphi}_i \;+\; \frac{\partial}{\partial X_j}\Big(P_W\,J\,\mathbf{F}^{-T}\Big)_{ij} \;=\; 0.$$

Each row of (6.54) thus matches one PDE in the barotropic system, confirming that the barotropic flow equations are captured by and can be derived from the multi-symplectic formulation. Thus by choosing Z , $H(Z))$ and using the skew-symmetric block matrices in (6.56) as shown above, the Lagrangian form of the barotropic fluid equations can be organised into a multi-symplectic system (6.54). In particular, each PDE (including momentum balance) is recovered by matching a block row on the left-hand side to the corresponding functional derivative on the right-hand side.

6.10.Multi-Symplectic Structure in the Final Discrete Formulation

The fully discrete system derived in (6.40)–(6.42) has the same geometric hallmarks as a *multi-symplectic* PDE [12, 16], although large and block-structured, the system can be interpreted as the discrete multi-symplectic form of the barotropic flow equations.

$$\begin{bmatrix}
\mathbb{H}_{\rho_0}^{-1} & 0 & -\mathbb{E}_t^{1,0} & 0 & 0 & 0\\
0 & \mathbb{H}_{\rho_0}^{-1} & 0 & -\mathbb{E}_t^{1,0} & 0 & 0\\
\mathbb{E}_t^{1,0^T} & 0 & 0 & -\mathbb{D}_{PK} & \mathbb{N}_\pi & 0\\
0 & \mathbb{E}_t^{1,0^T} & \mathbb{D}_{PK} & 0 & 0 & \mathbb{N}_\pi\\
0 & 0 & \mathbb{N}_\pi^{t_o\,T} & 0 & 0 & 0\\
0 & 0 & 0 & \mathbb{N}_\pi^{t_0\,T} & 0 & 0
\end{bmatrix}
\begin{bmatrix}
\bar{\boldsymbol{\pi}}_x\\ \bar{\boldsymbol{\pi}}_y\\ \bar{\boldsymbol{\varphi}}_x\\ \bar{\boldsymbol{\varphi}}_y\\ \hat{\boldsymbol{\pi}}_x^t\\ \hat{\boldsymbol{\pi}}_y^t
\end{bmatrix}
\;=\;
\begin{bmatrix}
0\\ 0\\ -\,\mathbb{N}^{t_o}\hat{\boldsymbol{\pi}}_x^{t_o}\\ -\,\mathbb{N}^{t_o}\hat{\boldsymbol{\pi}}_y^{t_o}\\ \varphi_{x_o}\\ \varphi_{y_o}
\end{bmatrix}, \tag{6.59}$$

In particular, each partial derivative with respect to time or space appears in off-diagonal matrix blocks, paired with blocks that are the negative transpose, reminiscent of the skew-symmetric operatorsM, K, L in the continuous setting.

- The blocks $\begin{bmatrix}\mathbb{H}_{\rho_0}^{-1} & 0\\ 0 & \mathbb{H}_{\rho_0}^{-1}\end{bmatrix}$ and $\begin{bmatrix}0 & -\mathbb{E}_t^{1,0}\\ \mathbb{E}_t^{1,0^T} & 0\end{bmatrix}$ combine to mimic $\mathbf{M}\,\partial/\partial t$. The negative transpose off-diagonal structure is reminiscent of the continuous skew form $\mathbf{M}^{\mathsf{T}} = -\mathbf{M}$.
- The block $\mathbb{D}_{PK}$ is paired with $\mathbb{E}_x^{1,0}$, $\mathbb{E}_y^{1,0}$ and $-\mathbb{E}_x^{1,0^T}$, $-\mathbb{E}_y^{1,0^T}$ to encode spatial derivatives (i.e. enforcing $\mathbf{F} = \nabla\varphi$ and the divergence of the stress). This arrangement is analogous to $\mathbf{K}\,\partial/\partial x$ or $\mathbf{L}\,\partial/\partial y$ in multi-symplectic PDEs.

Thus, each partial derivative in time or space direction lives in an off-diagonal block that has a corresponding negative-transpose block. These pairwise blocks are how the discrete scheme enforces the *balance* and *definition* equations with signs that match the continuous multi-symplectic structure. Furthermore, the appearance of $\mathbb{H}_{\rho_0}^{-1}$ and $\mathbb{H}_{P_w}$ (inside

$\mathbb{D}_{PK}$) is analogous to the continuous setting where a metric-like or “Hodge” operator arises in the symplectic form. In multi-symplectic integrators, it is typical that one has a symmetric mass or metric matrix that partially modifies the perfect skew-symmetry. Nevertheless, the essential block pattern remains intact.

7

Numerical Experiments and Results

This chapter presents computational experiments designed to test the proposed discretization's handling of pressure boundary conditions under inviscid barotropic flow and low-Mach scenarios. Two specific cases are examined: one with a higher external pressure and another with a lower external pressure. The primary goal is to demonstrate that key conservation properties— of quantities such as linear momentum, angular momentum, energy, and mass.

Since benchmark solutions are unavailable for the chosen setup, validation proceeds by examining the solution's convergence as the polynomial order increases. Of particular interest is the deformation up-to a limit time for increasing polynomial order, which serves as an indicator of solution convergence in the absence of an analytical reference. These tests also explore the discretization's behavior at low Mach numbers, where the dynamics depend on the pressure gradient rather than the absolute magnitude of the pressure. The fluid is therefore initialized with relatively low-pressure values. The ensuing sections detail the computational setup and the observed outcomes for each test scenario.

7.1.Computational Setup

7.1.1. Physical Parameters and Boundary Conditions

The fluid simulated is a two-dimensional domain $\Omega = [0, L_x] \times [0, L_y]$ is used, with $L_x = L_y = 1\,\mathrm{m}$ at $t = 0$s. The fluid has density $\rho = 1.25\,\mathrm{kg/m^3}$ and specific heat ratio $\gamma = 1.4$. A reference pressure $P_{\mathsf{ref}} = 1\,\mathrm{Pa}$ is imposed, and each boundary is subjected to pressure $P_{\mathsf{env}} = \alpha \times P_{\mathsf{ref}}$ where $\alpha < 1$ causes expansion at the boundary, and $\alpha > 1$ imposes a compressive condition. In this discussion, $\alpha = 0.85$ and $\alpha = 1.15$ are considered for the mentioned two cases. The spatial discretization uses polynomial degrees $N = 2,\ 3,\ 4,\ 5$, while the time dimension employs a polynomial order $N_t = 1$. Time integration proceeds for E_t uniform steps of size $\Delta t = 0.01\,\mathrm{s}$, yielding a total simulated duration of $E_t \times \Delta t$.

7.1.2. Nonlinear Iteration and Stopping Criterion

Each time step involves a Picard (fixed-point) iteration to resolve the nonlinear dependence of the pressure Hodge matrix on the Jacobian determinant, as previously described. In brief, the deformation gradient $\mathbf{F}$ is updated from the current estimate of $\boldsymbol{\varphi}$, and its determinant J is used to evaluate the spatial weight function $P_w(\rho_0, J)$. The pressure Hodge matrix $\mathbb{H}_{P_w}$ is then reassembled using the updated weight, and the system is solved for a new flow map. This process repeats until changes in J and $\mathrm{trace}(\mathbf{F})$ lie below a set tolerance, indicating convergence. The final converged state serves as the initial guess in the next time step. A maximum of $I_{max} = 100$ iterations is allowed per time step. The iteration terminates when changes in the Jacobian determinant of the deformation (J) and the trace of the deformation gradient, fall below the set tolerance of $tol = 10^{-12}$. The table 7.1 shown belwo summarises the the simulation parameters

Parameter	Symbol	Value
Fluid density	ρ	$1.25\,\mathrm{kg\,m^{-3}}$
Specific heat ratio	γ	1.4
Reference pressure	P_{ref}	$1\,\mathrm{Pa}$
Boundary pressure ratio	α	$0.85,\ 1.15$
Spatial polynomial orders	N	$2,\ 3,\ 4,\ 5$
Temporal polynomial order	N_t	1
Maximum Iterations	I_{max}	100
Convergence tolerance	tol	10^{-12}
Time step size	Δt	$0.01\,\mathrm{s}$
Number of time steps	E_t	700
Total simulated time	$E_t \times \Delta t$	$7\ s$

Table 7.1: Summary of key simulation parameters.

7.2.Results

This section presents the evolution of key flow variables, including the Lagrangian flow map, pressure, Mach number, and discrete conservation properties. Plots are shown for polynomial degrees $N = 3$ and $N = 5$; corresponding results for other values of N appear in the appendix. Time snapshots are selected to illustrate the progression of the deformation, and a simulation video provides a continuous view of the flow's development.

Following these visualizations, the convergence of the limiting deformation with respect to increasing polynomial order is examined. The discussion first covers the case $\alpha < 1$, which leads to expansion at the boundary, and then turns to $\alpha > 1$, illustrating compressive behaviour.

7.2.1. Expansion Case: $\alpha = 0.85$, $N = 3$

For this test case, the boundary pressure is set to $P_{\text{env}} = \alpha P_{\text{ref}} = 0.85 \times 1\,\mathrm{Pa} = 0.85\,\mathrm{Pa}$, thus imposing a lower external pressure relative to the interior. The resulting outward (expansion) flow is examined at several time snapshots and through discrete conservation properties.

Flow Map Evolution Figure 7.1 shows the evolution of the flow map (i.e., deformed configuration of the fluid domain) at selected times. At $t \approx 2.34\,\mathrm{s}$, the deformation is already observable near the boundary but remains small. By $t \approx 4.67\,\mathrm{s}$, the expansion is more pronounced, and the boundary continues to move outward through $t = 7\,\mathrm{s}$. The final configuration clearly exhibits a larger domain than the unit square at $t = 0$, consistent with the lower external pressure driving fluid expansion.

Because this is in a low-Mach setting, no shocks arise. The deformation is relatively smooth and only driven by the pressure differential.

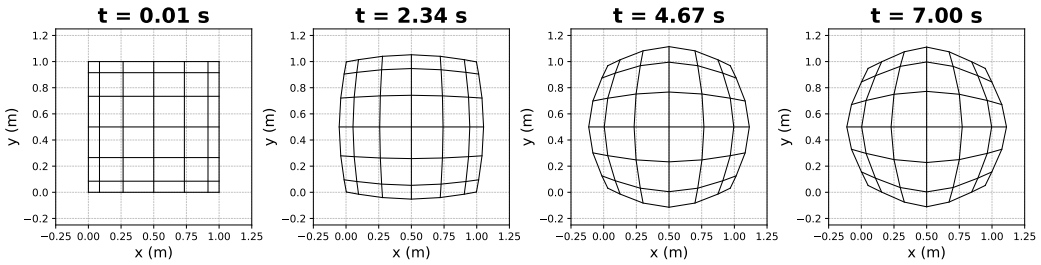

Figure 7.1: Snapshots of the flow map for $\alpha = 0.85$ and $N = 3$ at various times.

Pressure and Mach Number Fields Figures 7.2 and 7.3 show the pressure and Mach number distributions, respectively. The boundary is held at $0.85\,\mathrm{Pa}$, while the fluid interior starts at $1\,\mathrm{Pa}$. Initially, small-amplitude pressure waves (expansion) propagate from the boundary into the higher-pressure interior. Because there is no dissipation

mechanism, these waves continue to reflect at the domain boundaries, travelling back and forth and causing oscillations. Consequently, the ”square bubble” expands and once the pressure waves reflect, it contracts and this motion is repeated in time as long as the simulation is run with a net expansion compared to the initial configuration, this behaviour can be seen better in the videos of the same simulation attached in the appendix **??**. Further, the Mach number remains low (typically $\lesssim 0.2$), illustrating that the flow evolves smoothly without strong shock waves or compressible effects.

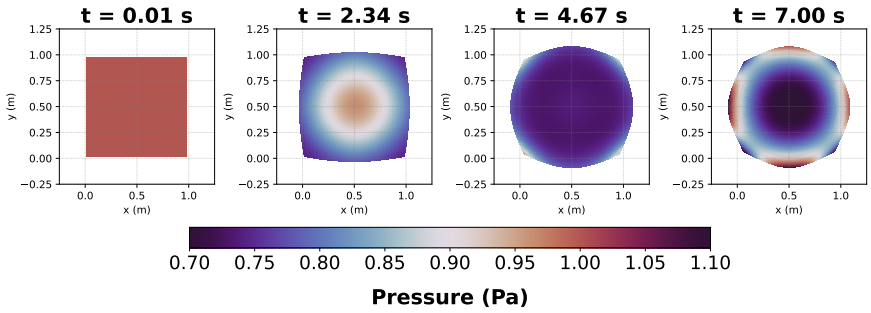

Figure 7.2: Pressure snapshots (in Pa) for $\alpha = 0.85$ and $N = 3$ at various times. The pressure field gradually relaxes toward the boundary value of $0.85\,\mathrm{Pa}$.

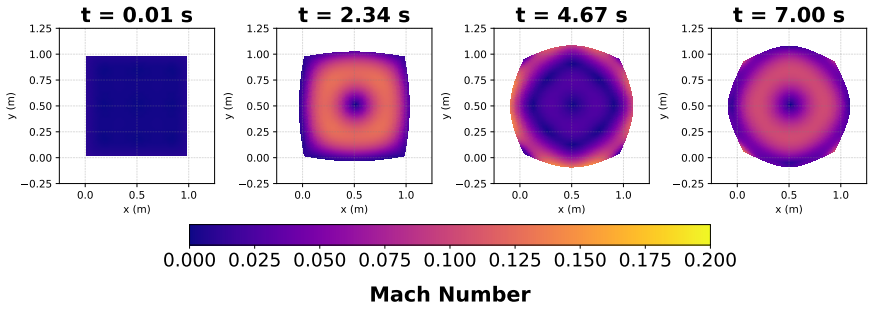

Figure 7.3: Mach number snapshots for $\alpha = 0.85$ and $N = 3$ at various times. The values remain low ($\lesssim 0.2$), confirming a subsonic regime.

Conservation of Linear Momentum Figure 7.4 plot the total linear momentum in x- and y-directions, respectively, over the entire simulation. The curves remain effectively constant at values near machine precision, indicating no artificial linear momentum creation or loss. Small round-off deviations on the order of 10^{-17} to 10^{-18} reflect numerical precision limits rather than physical phenomena.

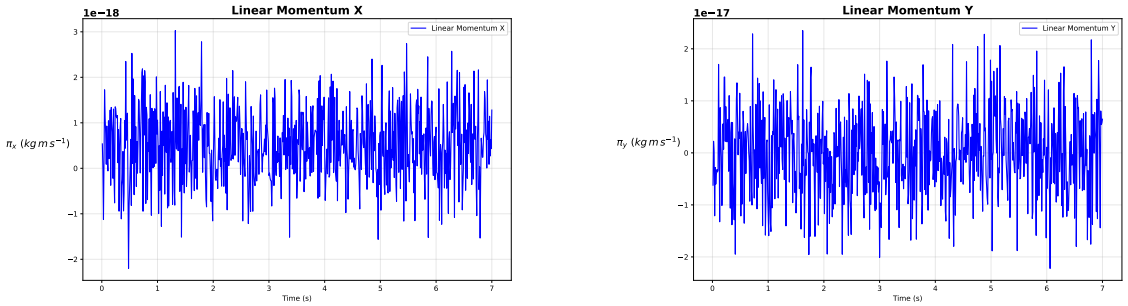

Figure 7.4: Total linear momentum in the x and y -direction for $\alpha = 0.85$, $N = 3$.

Conservation of Angular Momentum and Mass Figure 7.5a shows the evolution of total angular momentum. Much like linear momentum, angular momentum remains nearly constant, deviating only by 10^{-15} during the entire

simulation. This invariance up to the machine precision highlights the structure-preserving nature of the discretization in reproducing the rotational symmetries inherent to inviscid barotropic flow. Figure 7.5b illustrates the total mass of the system over time for. The vertical axis shows the difference between the instantaneous mass $M(t)$ and its initial value M_0, in kilograms. In an inviscid, closed system without mass sources or sinks, total mass should remain constant and this can be seen in the plot shown below.

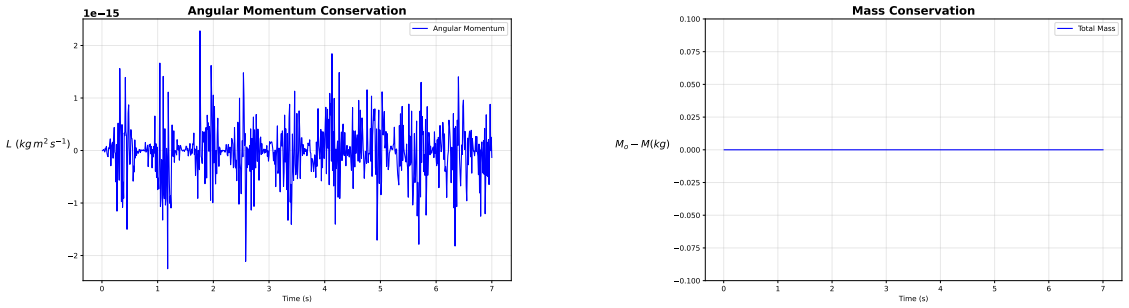

(a) Angular momentum evolution

(b) Mass conservation

Figure 7.5: Total angular momentum and change in mass for $\alpha = 0.85$, $N = 3$.

Energy Conservation Figure 7.6 shows the change in total energy over time. It remains zero again up to the order of machine precision. Since no external work or dissipative mechanisms are modelled, the total energy should remain invariant; the near-flat curve confirms the discretization does not introduce spurious energy gains or losses.

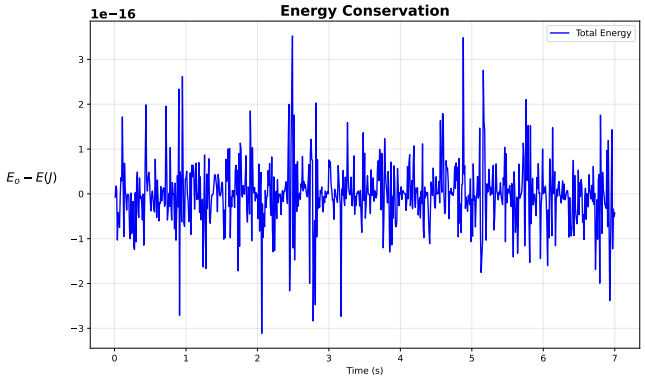

Figure 7.6: Change in total energy for $\alpha = 0.85$, $N = 3$.

For $\alpha = 0.85$, the fluid expands outward from the boundaries over $7\,\mathrm{s}$, driven by the reduced external pressure. The flow remains subsonic, as evidenced by the low Mach numbers, and the structure-preserving discretization accurately maintains momentum (both linear and angular) and total energy within machine precision. Although the results for $N = 3$ show consistent performance, the polynomial order is still relatively low, so the boundary deformation is not yet fully captured. In contrast, subsequent results at higher polynomial order ($N = 5$) reveal a smoother boundary deformation that better approximates the expansion.

7.2.2. Expansion Case: $\alpha = 0.85$, $N = 5$

This section examines the expansion scenario for a higher spatial polynomial order, $N = 5$. As before, the boundary pressure is set to $P_{\text{env}} = \alpha P_{\text{ref}} = 0.85 \times 1\,\mathrm{Pa} = 0.85\,\mathrm{Pa}$, leading to a lower external pressure relative to the interior. Increasing the polynomial degree improves the resolution of the flow map and related fields, resulting in a smoother depiction of the boundary expansion and refined flow variables.

Flow Map Evolution Figure 7.7 shows snapshots of the flow map at the same representative times used in the $N = 3$ case. With $N = 5$, the outward deformation is captured with higher accuracy, clearly visible near the boundaries.

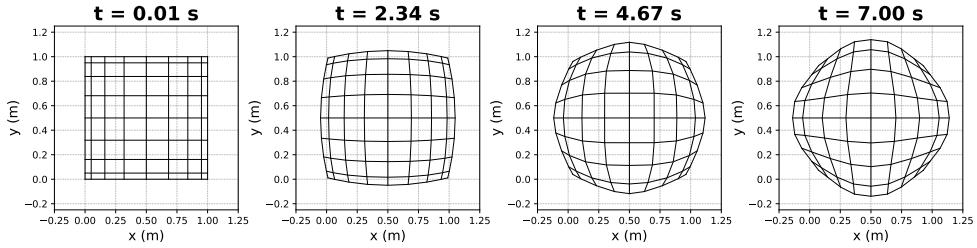

Figure 7.7: Snapshots of the flow map for $\alpha = 0.85$ and $N = 5$ at various times.

Pressure and Mach Number Fields Figures 7.8 and 7.9 depict the pressure and Mach number fields, respectively. As in the lower-order case, the boundary is maintained at $0.85\,\mathrm{Pa}$ while the interior begins at $1\,\mathrm{Pa}$. The refinement afforded by $N = 5$ reveals a slightly more uniform pressure gradient transitioning from the interior to the boundary, confirming that the higher-degree polynomial basis better resolves the flow. The Mach number still remains well below unity (i.e., $\lesssim 0.2$), reinforcing the subsonic nature of the expansion.

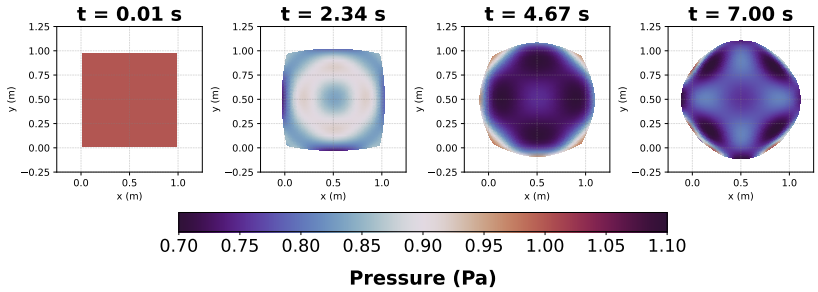

Figure 7.8: Pressure snapshots (in Pa) for $\alpha = 0.85$ and $N = 5$ at various times.

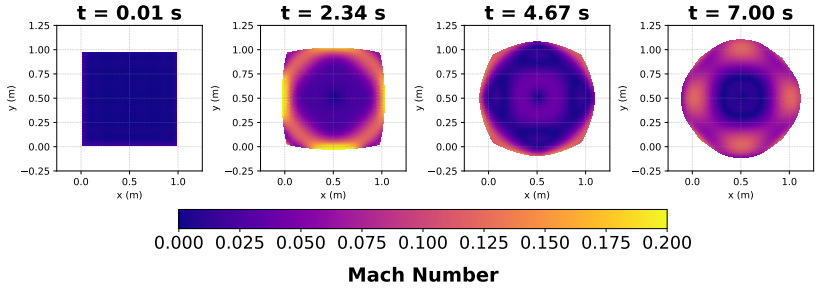

Figure 7.9: Mach number snapshots for $\alpha = 0.85$ and $N = 5$ at various times.

Conservation of Linear Momentum Figure 7.10 shows the total linear momentum in the x- and y-directions. As with $N = 3$, no net gain or loss of linear momentum is observed beyond machine-precision limits. The discretization's structure-preserving nature ensures this invariant remains valid even at higher spatial resolution.

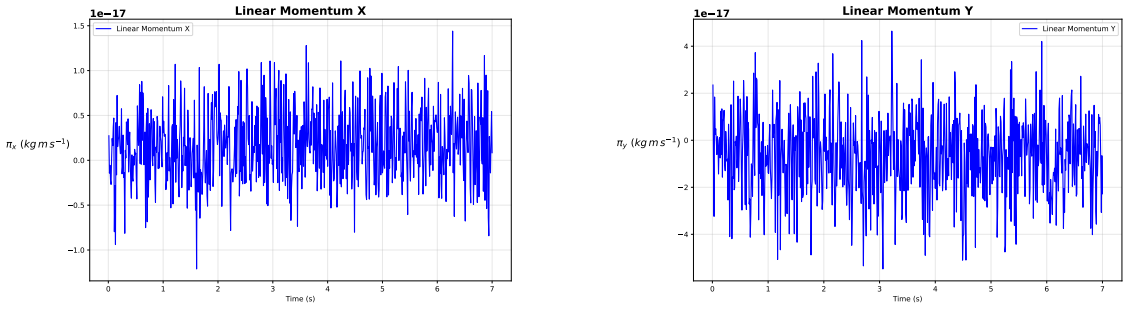

Figure 7.10: Total linear momentum in the x- (left) and y- (right) directions for $\alpha = 0.85$, $N = 5$.

Conservation of Angular Momentum and Mass Figures 7.11(a) and 7.11(b) show the evolution of total angular momentum and total mass, respectively. As with the $N = 3$ case, both quantities are conserved to within the order of 10^{-15} to 10^{-17} . The small deviations within this order are attributed to floating-point limitations and the iterative solver tolerance, rather than any physical loss or gain.

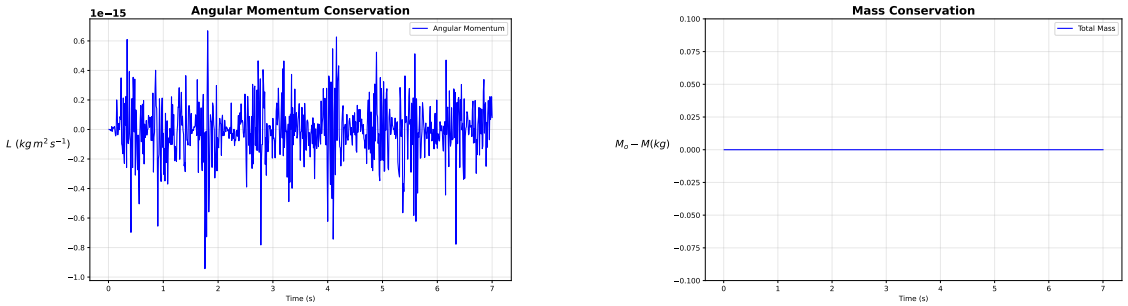

(a) Angular momentum

(b) Mass conservation

Figure 7.11: Total angular momentum and mass for $\alpha = 0.85$, $N = 5$.

Energy Conservation Figure 7.12 plots the change in total energy over the entire simulation window. Just as in the $N = 3$ case, energy remains essentially unchanged.

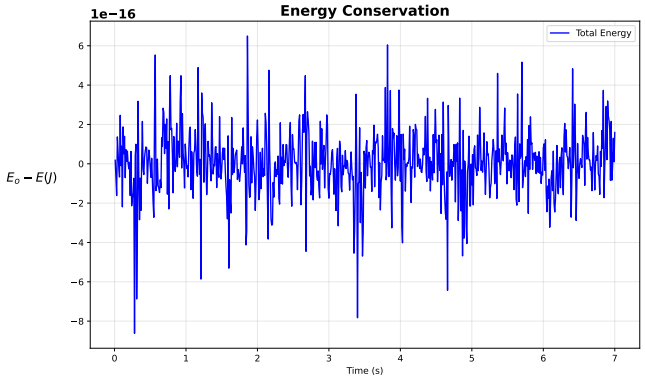

Figure 7.12: Change in total energy for $\alpha = 0.85$, $N = 5$.

In summary, increasing the polynomial order from $N = 3$ to $N = 5$ results in a more refined resolution of the boundary expansion and flow variables without compromising conservation properties. The flow remains subsonic, with low Mach numbers, and all key invariants linear momentum, angular momentum, mass, and energy are preserved to machine accuracy. These findings demonstrate that the proposed space-time spectral method not only respects the fundamental physics of inviscid barotropic flow but also continues to converge to a smoother solution at higher polynomial orders.

Deformation Convergence Figure 7.13 compares the final deformation of the fluid domain at selected times for four spatial polynomial degrees, $N = 2, 3, 4, 5$. These snapshots illustrate how the boundary shape and interior deformation change with increasing polynomial order. At early times, such as $t = 2.34\,\mathrm{s}$, the discrepancies between different N values are visible but remain small. As the simulation progresses (e.g. $t = 4.67\,\mathrm{s}$), the higher-order solutions capture a smoother, more refined expansion. By the final time $t = 7.00\,\mathrm{s}$, the domain deformations for $N = 4$ and $N = 5$ closely match, suggesting that the limiting shape has nearly been reached at higher polynomial orders.

This behavior confirms that the proposed space-time spectral method converges to a consistent deformation profile as N increases under boundary conditions causing expansion of the flow.

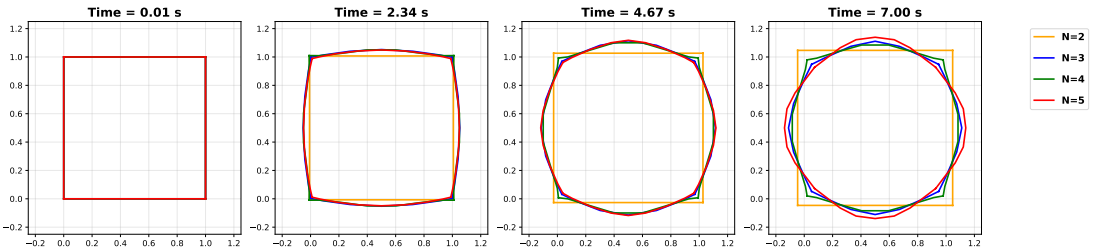

Figure 7.13: Comparison of flow-map deformations at $t = \{0.01,\ 2.34,\ 4.67,\ 7.00\}\,\mathrm{s}$ for $N = 2, 3, 4, 5$.

7.2.3. Compression Case: $\alpha = 1.15$, $N = 3$

For the compression test case, the boundary pressure is set to $P_{\text{env}} = \alpha\, P_{\text{ref}} = 1.15\,\mathrm{Pa}$, which is higher than the fluid interior's initial pressure $1.0\,\mathrm{Pa}$. Consequently, a compression wave travels inward from the boundary, reducing the domain's volume over time.

Flow Map Evolution. Figure 7.14 shows snapshots of the flow map at selected times. At $t = 0.01\,\mathrm{s}$, the boundary has just begun to move, and the domain still appears nearly unchanged. By $t = 1.40\,\mathrm{s}$, a clear compression is visible, with bulges near the midpoints of each side and corners pushed inward. This wavelike behaviour continues as the initially square bubble transitions toward a more circular shape, reducing in volume by $t = 4.67\,\mathrm{s}$ and $t = 7\,\mathrm{s}$. Throughout this process, the compression proceeds relatively smoothly due to the inward pressure gradient, resulting in a significantly smaller final configuration compared to the initial unit square.

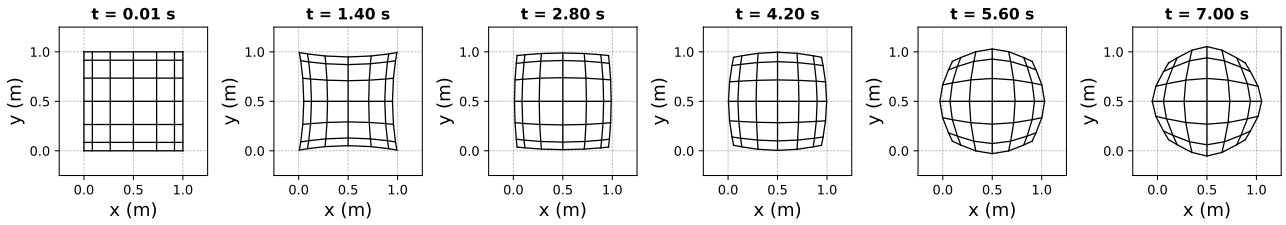

Figure 7.14: Flow map snapshots for $\alpha = 1.15$ and $N = 3$ at various times.

Pressure and Mach Number Fields. Figures 7.15 and 7.16 illustrate the corresponding pressure and Mach number fields. With a higher boundary pressure of $1.15\,\mathrm{Pa}$, the interior pressure rises and eventually settles closer to the boundary level as time advances. Small compression waves reflect within the domain and due to the lack of dissipation they keep reflecting driving oscillatory behaviour as long as the simulation is run.

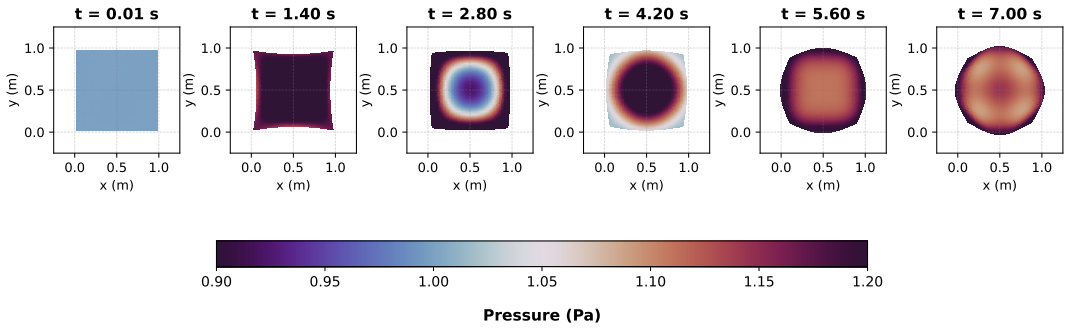

Figure 7.15: Pressure snapshots (in Pa) for $\alpha = 1.15$, $N = 3$.

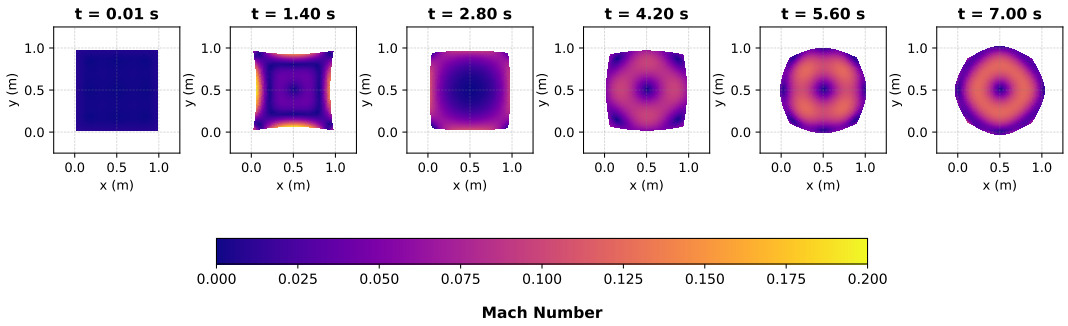

Figure 7.16: Mach number snapshots for $\alpha = 1.15$, $N = 3$.

Conservation of Linear Momentum. As shown in Figure 7.17, the total linear momentum in the x- and y-directions remains nearly constant, with variations only in the order of machine precision. Despite the boundary pushing inward, due to symmetry of the motion in both x and y direction, no net momentum is introduced or removed from the system. This is reflected in the plots, confirming that the scheme preserves linear momentum for this compressive flow.

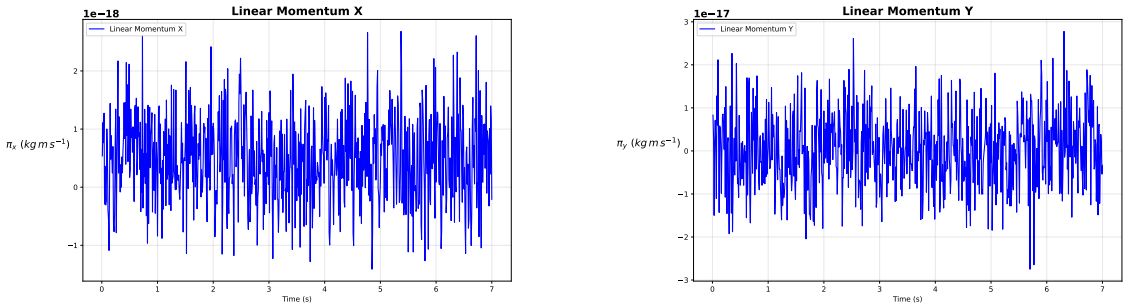

Figure 7.17: Total linear momentum in the x (left) and y (right) directions for $\alpha = 1.15$, $N = 3$.

Angular Momentum and Mass Conservation. Figure 7.18 (a) shows that angular momentum throughout the simulation, deviating only at 10^{-15} levels. Meanwhile, Figure 7.18 (b) indicates that mass remains constant to within

floating-point tolerance, consistent with an inviscid fluid model lacking sources or sinks.

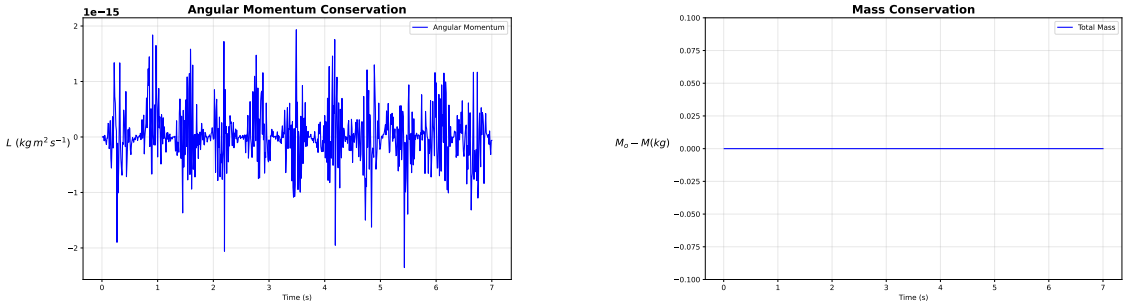

(a) Angular momentum

(b) Mass conservation

Figure 7.18: Total angular momentum and mass for $\alpha = 1.15$, $N = 3$.

Energy Conservation. Lastly, Figure 7.19 shows the change in total energy over time. Since no external work is introduced apart from maintaining a constant boundary pressure, and no dissipation mechanisms exist, the total energy thus remains unchanged. The small numerical fluctuations (on the order of 10^{-16}) validate that the method does not add or remove energy.

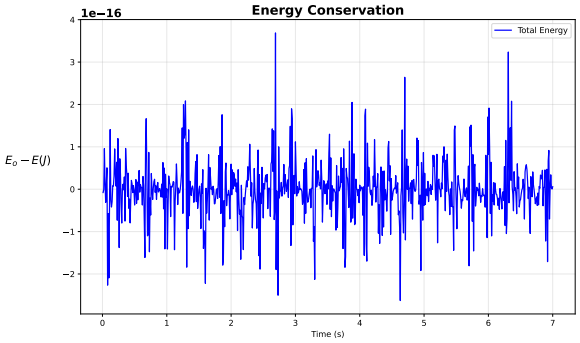

Figure 7.19: Change in total energy for $\alpha = 1.15$, $N = 3$.

7.2.4. Compression Case: $\alpha = 1.15$, $N = 5$

For this higher-order test, the boundary pressure remains $P_{\text{env}} = \alpha P_{\text{ref}} = 1.15\,\text{Pa}$, driving fluid compression from the boundaries toward the interior. Increasing the polynomial degree to $N = 5$ enhances the spatial resolution and yields a smoother representation of the inward boundary motion compared to the $N = 3$ case.

Flow Map Evolution. Figure 7.20 shows the flow map snapshots, a more sharply resolved boundary displacement can be observed for this case, with rest of the behaviour being the same as the previous case.

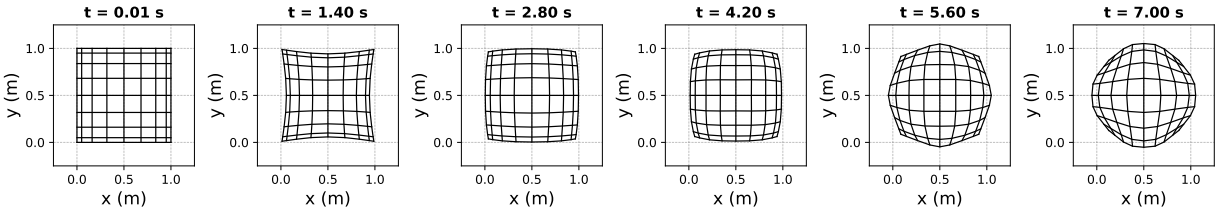

Figure 7.20: Snapshots of the flow map for $\alpha = 1.15$ and $N = 5$ at various times.

Pressure and Mach Number Fields. Figures 7.21 and 7.22 show the pressure and Mach number distributions, respectively. Similar to the $N = 3$ scenario, the boundary at $1.15\,\mathrm{Pa}$ compresses the interior from all sides. Because no dissipation is modeled, compression waves reflect throughout the domain; however, the higher polynomial order provides a more refined view of these waves as they move inward.

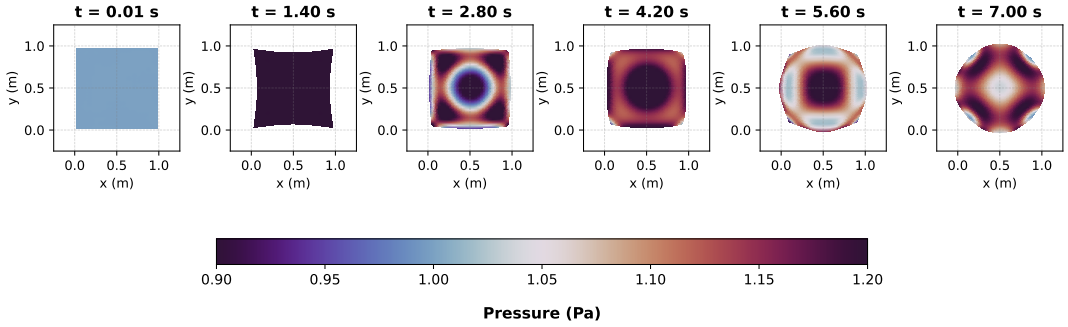

Figure 7.21: Pressure snapshots (in Pa) for $\alpha = 1.15$, $N = 5$ at various times.

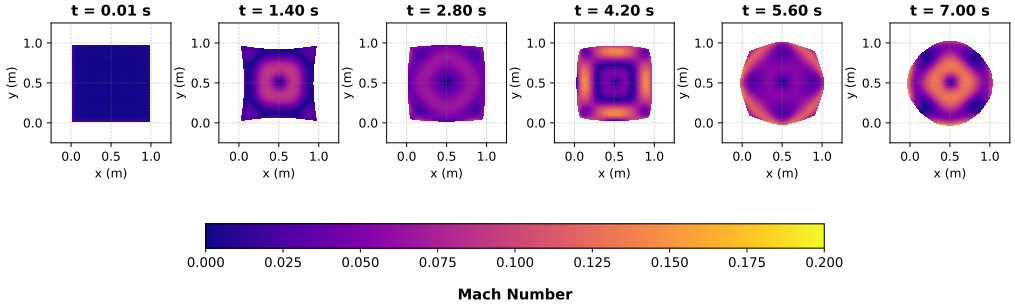

Figure 7.22: Mach number snapshots for $\alpha = 1.15$, $N = 5$.

Conservation of Linear Momentum. As shown in Figure 7.23, the total linear momentum in both the x- and y-directions remains essentially constant. This result mirrors the $N = 3$ case.

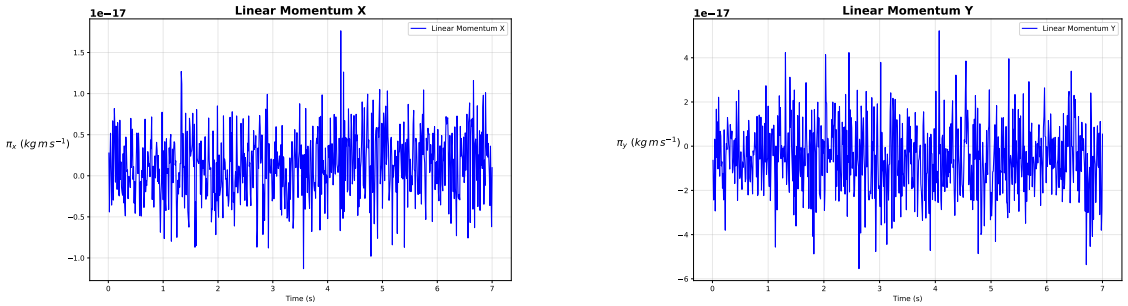

Figure 7.23: Total linear momentum in the x and y directions for $\alpha = 1.15$, $N = 5$.

Angular Momentum and Mass Conservation. Figures 7.24(a) and 7.24(b) confirm that angular momentum and mass remain constant over the simulation.

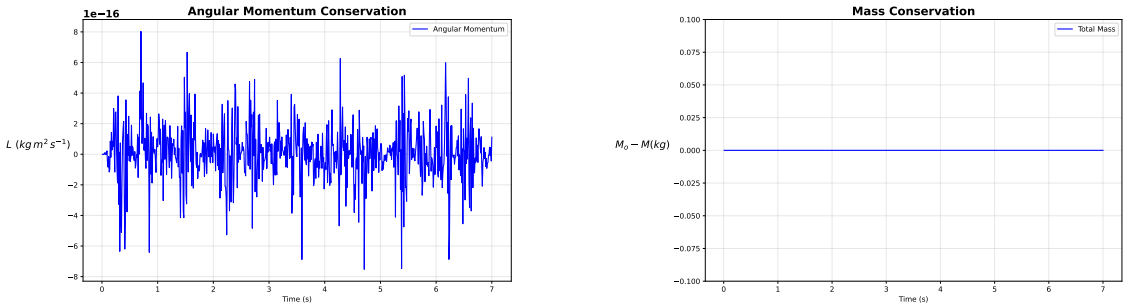

(a) Angular momentum

(b) Mass conservation

Figure 7.24: Angular momentum and mass for $\alpha = 1.15$, $N = 5$.

Energy Conservation. Finally, Figure 7.25 shows the total energy. As in previous cases, the absence of external work or dissipation leads to nearly perfect energy conservation, with only minor numerical fluctuations in the order of machine precision.

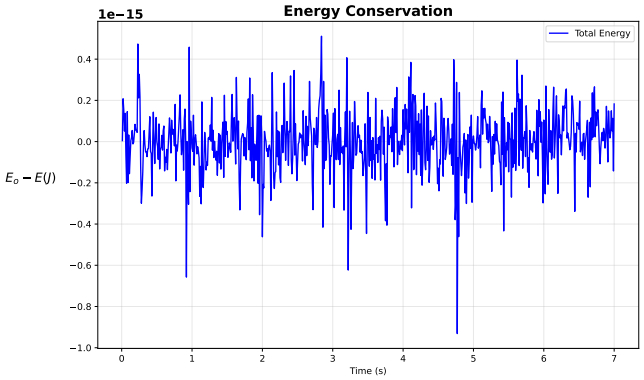

Figure 7.25: Change in otal energy for $\alpha = 1.15$, $N = 5$.

Deformation Convergence Increasing the polynomial order from $N = 3$ to $N = 5$ yields a more refined representation of the inward boundary motion and the associated compression waves. The flow remains subsonic, and the scheme continues to preserve linear momentum, angular momentum, mass, and energy. These observations confirm that the proposed space-time spectral discretization behaves robustly under compressive boundary conditions, converging to a smoothly resolved solution as the polynomial degree increases.

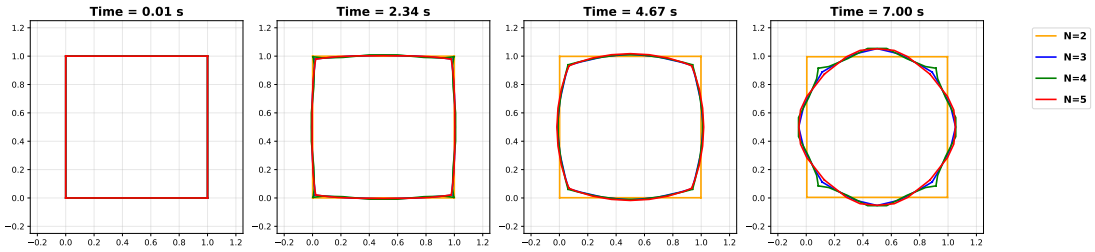

Figure 7.26: Comparison of the convergence of flow map deformations for various polynomial orders..

8

Conclusion and Future Work

8.1.Conclusion

This thesis revisits the challenges in computational fluid dynamics (CFD): representing inviscid barotropic flow in a Lagrangian perspective, while preserving key conservation properties such as mass, momentum, and energy. The motivation stems from the fact that, although many existing methods match experimental data in specific test cases, they often fail to conserve invariants over long simulation times. Another key motivation for adopting a Lagrangian perspective comes from recognizing that, in many aerospace and aeronautical applications, for example the wing is usually kept stationary in both wind tunnel setups and conventional (Eulerian) CFD analyses. This simplification is made so that the flow ”moves” past a fixed object. However, in a more realistic flight condition, the wing itself is moving (translating and/or rotating), while the flow is otherwise unbounded. Thus from a purely physical standpoint, it is more accurate to treat the moving body and the parcel-based fluid motion in a single, coherent Lagrangian framework, rather than freezing the wing and letting only the flow move.

By formulating inviscid barotropic flow in a Lagrangian perspective and employing a multisymplectic variational principle, a pathway emerges for constructing a higher-order mimetic scheme that addresses these limitations. The primary research question *whether the proposed methodology can discretize inviscid barotropic flow on a space–time grid while preserving essential symmetries and conservation laws* has guided each stage of this investigation.

The key results and observations of this thesis can be summarized as follows:

- A higher-order discretization is defined for inviscid barotropic flow using the first Piola–Kirchhoff tensor, which plays a central role in mapping stresses from the reference to the deformed domain. This approach avoids the problematic mesh distortions often encountered in purely physical-space Lagrangian methods.
- Boundary conditions, including free and pressure boundaries, are incorporated in a way that maintains stability and accuracy without relying on artificial techniques.
- The scheme is shown to preserve linear momentum, angular momentum, and energy in the order of machine precision, by leveraging multisymplectic and mimetic principles. This aligns the discrete model with the geometric and topological foundations of the continuous system.
- The method consistently captures low-Mach-number regimes without special preconditioning or artificial adjustments to the speed of sound.
- Finally, the work lays a foundation for extending the approach to multi-physics scenarios, particularly fluid–structure interaction (FSI), within a unified Lagrangian setting.

Numerical experiments confirm that pressure and free boundary conditions can be accurately imposed, leading to convergent deformations as the polynomial order is increased. In addressing the research questions, the results affirm that, *yes*, an inviscid barotropic flow governed by a multisymplectic Lagrangian formulation can indeed be discretized with a higher-order mimetic method on a space-time grid, including free and pressure boundaries while preserving essential symmetries and conservation laws.

8.2.Future Work

There are several directions for extending and refining the present framework. A first direction involves moving beyond a single-element configuration toward a *hybrid finite element formulation* that accommodates multiple elements in the same computational domain to allow for more complex simulations and geometries.

A second major step is extending the current space-time Lagrangian formulation to three-dimensional domains, an essential requirement for many engineering and scientific problems. However, because visual interaction with fully 4D (3D space + 1D time) meshes is not feasible, the necessary incidence matrices must be computed algebraically. Moreover, constructing the basis functions demands treatment of complex tensor products in four dimensions. These complications, combined with the increased dimensionality, significantly increases the computational requirements, necessitating high-performance computing strategies such as parallelization or GPU-accelerated implementations. Equally important is preserving topological consistency and the underlying symplectic structure in the 4D mesh to ensure accuracy and stability over long integration times.

Beyond purely inviscid dynamics, a third direction involves the *inclusion of dissipative terms* based on either the metriplectic 4-bracket formulation proposed by [5, 44] or the variational framework for extended irreversible thermodynamics introduced by [45]. These frameworks integrate dissipation while preserving significant parts of the system's underlying geometric structure. Incorporating such mechanisms would allow the numerical method to capture fluid behaviors such as viscosity, or thermal effects without resorting to arbitrary damping terms. This addition could lead to a balanced scheme that sustains an overall symplectic core while mimicking physically relevant energy losses.

Finally, a fourth extension is to *couple the present solver with a solid mechanics solver* to enable fluid–structure interaction (FSI) simulations. Since solid mechanics often employs a Lagrangian view of material points, the same mimetic and multisymplectic principles can be applied to both solvers, allowing fluid and structure to be tracked on an equal footing. This unified viewpoint would ensure consistent momentum and energy exchange across the fluid-structure interface, offering a more direct and faithful representation of phenomena such as aeroelastic wing deformation or biomechanical flows. Nevertheless, ensuring that each side's distinct conservation properties are retained in a combined solver remains a key challenge for future research.

References

[1] V. E. Zakharov. “Stability of periodic waves of finite amplitude on the surface of a deep fluid”. In: *Journal of Applied Mechanics and Technical Physics* 9.2 (1968), pp. 190–194.

[2] G. B. Whitham. *Linear and Nonlinear Waves*. Wiley, 1974.

[3] R. G. Rehm and H. R. Baum. “The equations of motion for thermally driven, buoyant flows”. In: *NIST Journal of Research* 83.3 (1978), pp. 297–308.

[4] H. Goldstein. *Classical Mechanics*. 2nd. Addison-Wesley, 1980.

[5] P.J. Morrison. “A paradigm for metriplectic dynamics”. In: *Physics Letters A* 117.3 (1986), pp. 89–94.

[6] E. Turkel. “Preconditioned methods for solving the incompressible and low speed compressible equations”. In: *Journal of Computational Physics* 72.2 (1987), pp. 277–298.

[7] R. Abraham, J. E. Marsden, and T. Ratiu. *Manifolds, Tensor Analysis, and Applications*. 2nd. Springer, 1988.

[8] V. I. Arnold. *Mathematical Methods of Classical Mechanics*. 2nd. Springer, 1989.

[9] Harley Flanders. *Differential Forms with Applications to the Physical Sciences*. New York: Dover Publications, 1989. ISBN: 978-0486687128. URL: `https://www.doverpublications.com/9780486687128`.

[10] Y. H. Choi and C. L. Merkle. “Application of time-derivative preconditioning”. In: *Journal of Computational Physics* 105.2 (1993), pp. 207–223.

[11] J. M. Weiss and W. A. Smith. “Preconditioning applied to variable and constant density flows”. In: *AIAA Journal* 33.11 (1995), pp. 2050–2057.

[12] T. J. Bridges. “Multi-symplectic structures and wave propagation”. In: *Math. Proc. Cambridge Philos. Soc.* 121.1 (1997), pp. 147–190.

[13] R. Hiptmair. “Discrete Hodge Operators”. In: *Numerical Methods for Partial Differential Equations* 13.3 (1997), pp. 237–256.

[14] Claudio Mattiussi. “An Analysis of Finite Volume, Finite Element, and Finite Difference Methods Using Some Concepts from Algebraic Topology”. In: *Journal of Computational Physics* 133.2 (1997), pp. 289–309. DOI: `10.1006/jcph.1997.5656`. URL: `https://doi.org/10.1006/jcph.1997.5656`.

[15] Alain Bossavit. *Computational Electromagnetism: Variational Formulations, Complementary, Edge Elements*. Academic Press, 1998.

[16] J. E. Marsden, G. W. Patrick, and S. Shkoller. “Multisymplectic geometry, variational integrators, and nonlinear PDEs”. In: *Commun. Math. Phys.* 199 (1998), pp. 351–395.

[17] J. E. Marsden and T. S. Ratiu. *Introduction to Mechanics and Symmetry*. Springer, 1999.

[18] Hassler Whitney. *Geometric Integration*. New York: Dover Publications, 2000. ISBN: 0486445836.

[19] P. G. Ciarlet. *The Finite Element Method for Elliptic Problems*. SIAM Classics, 2002.

[20] Ralf Hiptmair. “Finite elements in computational electromagnetism”. In: *Acta Numerica* 11 (2002), pp. 237–339.

[21] Alexandre Ern and Jean-Luc Guermond. *Theory and Practice of Finite Elements*. Applied Mathematical Sciences. Springer, 2004.

[22] Christian Wieners. *Foundation of Mathematical Elasticity*. Version Version of November 24, 2005. First lecture for a Short Course on Mathematical Modelling in Solid Mechanics. Nov. 2005.

[23] Pavel Bochev and James Hyman. “Principles of mimetic discretizations of differential operators”. In: *Compatible Spatial Discretizations*. Ed. by D. Arnold et al. New York: Springer, 2006, pp. 89–119.

[24] Susanne C. Brenner and Ridgway Scott. *The Mathematical Theory of Finite Element Methods*. Texts in Applied Mathematics. Springer, 2007.

[25] J. N. Reddy. *An Introduction to Continuum Mechanics*. Cambridge University Press, 2007.

[26] Douglas Arnold, Richard Falk, and Ragnar Winther. “Finite Element Exterior Calculus: From Hodge Theory to Numerical Stability”. In: *Bulletin of the American Mathematical Society* 47 (2010), pp. 281–354.

[27] Theodore Frankel. *The Geometry of Physics: An Introduction*. 3rd. New York: Cambridge University Press, 2011. ISBN: 978-0521763684. URL: https://www.cambridge.org/9780521763684.

[28] Marc Gerritsma. “Edge Functions for Spectral Element Methods”. In: *Spectral and High Order Methods for Partial Differential Equations*. Ed. by Jan Hesthaven and Einar Rønquist. Vol. 76. Lecture Notes in Computational Science and Engineering. Berlin, Heidelberg: Springer, 2011. DOI: 10.1007/978-3-642-15337-2_17. URL: https://doi.org/10.1007/978-3-642-15337-2_17.

[29] Artur Palha and Marc Gerritsma. “Mimetic Framework on Curvilinear Quadrilaterals of Arbitrary Order”. In: *ArXiv Preprint* (2011), pp. 1–69. DOI: 10.48550/arXiv.1111.4304. URL: https://arxiv.org/abs/1111.4304.

[30] Marc Gerritsma. “An Introduction to a Compatible Spectral Discretization Method”. In: *Mechanics of Advanced Materials and Structures - MECH ADV MATER STRUCT* 19 (Jan. 2012). DOI: 10.1080/15376494.2011.572237.

[31] Patrick Hamill. *A Student’s Guide to Lagrangians and Hamiltonians*. New York: Cambridge University Press, 2013. ISBN: 978-1-107-61752-0. URL: https://www.cambridge.org/9781107617520.

[32] J. M. Lee. *Introduction to Smooth Manifolds*. 2nd. Springer, 2013.

[33] Enzo Tonti. *The Mathematical Structure of Classical and Relativistic Physics: A General Classification Diagram*. Modeling and Simulation in Science, Engineering and Technology. New York, Heidelberg, Dordrecht, London: Springer, 2013. ISBN: 978-1-4614-7421-0. DOI: 10.1007/978-1-4614-7422-7. URL: https://doi.org/10.1007/978-1-4614-7422-7.

[34] Enzo Tonti. “Why starting from differential equations for computational physics?” In: *Journal of Computational Physics* 257 (2014). Physics-compatible numerical methods, pp. 1260–1290. ISSN: 0021-9991. DOI: https://doi.org/10.1016/j.jcp.2013.08.016. URL: https://www.sciencedirect.com/science/article/pii/S0021999113005548.

[35] Artur Palha. “A Mass, Vorticity and Energy Conserving (MVEC) Scheme for the Incompressible Navier–Stokes Equations in a Rotating Frame Using High Order Mimetic Spectral Elements”. PhD thesis. Delft, The Netherlands: Delft University of Technology, 2015.

[36] Artur Palha and Marc Gerritsma. “A Mass, Energy, Enstrophy and Vorticity Conserving (MEEVC) Mimetic Spectral Element Discretization for the 2D Incompressible Navier–Stokes Equations”. In: *Journal of Computational Physics* 328 (2017), pp. 200–220.

[37] Keenan Crane. *Discrete Differential Geometry: An Applied Introduction*. Lecture Notes. Pittsburgh, PA, 2021. URL: https://www.cs.cmu.edu/~kmcrane/Projects/DDG.

[38] François Demoures and François Gay-Balmaz. “Multisymplectic Variational Integrators for Barotropic and Incompressible Fluid Models with Constraints”. In: *arXiv preprint arXiv:2102.10907* (Feb. 2021). URL: https://arxiv.org/abs/2102.10907.

[39] J. K. Hunter. *Hamiltonian Fluid Mechanics*. 2021. URL: https://www.math.ucdavis.edu/~hunter/.

[40] Joey Dekker. “The Lagrangian Mimetic Spectral Element Method: Solving (non-)Linear Advection Problems with a Mimetic Method”. MA thesis. Delft University of Technology, Dec. 2022.

[41] François Demoures and François Gay-Balmaz. “Unified Discrete Multisymplectic Lagrangian Formulation for Hyperelastic Solids and Barotropic Fluids”. In: *Journal of Nonlinear Science* (2022). DOI: 10.1007/s00332-022-09849-y.

[42] Varun Jain et al. “Construction and Application of Algebraic Dual Polynomial Representations for Finite Element Methods on Quadrilateral and Hexahedral Meshes”. In: *Computers Fluids* (2022).

[43] Yi Zhang. “Mimetic Spectral Element Method and Extensions Toward Higher Computational Efficiency”. PhD thesis. Delft, The Netherlands: TU Delft, 2022. DOI: 10.4233/uuid:a87e7be3-fb08-4706-9676-a6ae43f5aa0d. URL: https://doi.org/10.4233/uuid:a87e7be3-fb08-4706-9676-a6ae43f5aa0d.

[44] Azeddine Zaidni and Philip J. Morrison. “Metriplectic 4-Bracket Algorithm for Constructing Thermodynamically Consistent Dynamical Systems”. In: *arXiv preprint arXiv:2501.00159* (2024). Submitted December 2024.

[45] François Gay-Balmaz. “A Variational Principle for Extended Irreversible Thermodynamics: Heat Conducting Viscous Fluids”. In: *arXiv preprint arXiv:2502.17079 [math-ph]* (2025). Submitted on 24 Feb 2025. DOI: 10.48550/arXiv.2502.17079.

A

Variational Analysis: Euler-Lagrange Equations

This appendix presents an introduction to the Euler–Lagrange equations via a variational argument on the action integral. For a more detailed discussion of classical variational methods, see [31].

Formulation of the Action and its Variation: Consider a Lagrangian density $\mathcal{L}(\varphi, \dot{\varphi}, \nabla\varphi)$ defined on a spatio-temporal domain $\mathcal{B} \times [0, T]$. The associated action functional is

$$\mathcal{S}[\varphi] = \int_0^T \int_{\mathcal{B}} \mathcal{L}(\varphi, \dot{\varphi}, \nabla\varphi)\, \mathrm{d}X\, \mathrm{d}t. \tag{A.1}$$

Let $\delta\varphi$ be a small perturbation of φ. The principle of stationary action requires $\delta\mathcal{S} = 0$ for all admissible variations $\delta\varphi$ that vanish at $t = 0$ and $t = T$.

Variation with respect to the time derivative $\dot{\varphi}$: The term

$$\int_0^T \int_{\mathcal{B}} \frac{\partial \mathcal{L}}{\partial \dot{\varphi}^i}\, \delta\dot{\varphi}^i\, \mathrm{d}X\, \mathrm{d}t \tag{A.2}$$

is integrated by parts in time:

$$\int_0^T \int_{\mathcal{B}} \frac{\partial \mathcal{L}}{\partial \dot{\varphi}^i}\, \delta\dot{\varphi}^i\, \mathrm{d}X\, \mathrm{d}t = -\int_0^T \int_{\mathcal{B}} \frac{\mathrm{d}}{\mathrm{d}t}\left(\frac{\partial \mathcal{L}}{\partial \dot{\varphi}^i}\right) \delta\varphi^i\, \mathrm{d}X\, \mathrm{d}t, \tag{A.3}$$

noting that $\delta\varphi$ vanishes at the initial and final times.

Variation with respect to the spatial gradient $\nabla\varphi$: The portion of the action involving $\nabla\varphi$ can be written as

$$\int_{\mathcal{B}} \frac{\partial \mathcal{L}}{\partial(\nabla_j \varphi^i)}\, \delta(\nabla_j \varphi^i)\, \mathrm{d}X. \tag{A.4}$$

Applying the divergence theorem:

$$\int_{\mathcal{B}} \frac{\partial \mathcal{L}}{\partial(\nabla_j \varphi^i)}\, \delta(\nabla_j \varphi^i)\, \mathrm{d}X = \int_{\partial\mathcal{B}} \frac{\partial \mathcal{L}}{\partial(\nabla_j \varphi^i)}\, n_j\, \delta\varphi^i\, \mathrm{d}S - \int_{\mathcal{B}} \frac{\partial}{\partial X_j}\left(\frac{\partial \mathcal{L}}{\partial(\nabla_j \varphi^i)}\right) \delta\varphi^i\, \mathrm{d}X, \tag{A.5}$$

where n_j is the outward normal on $\partial\mathcal{B}$. Collecting these contributions into $\delta\mathcal{S}$ leads to

$$\delta\mathcal{S} = \int_0^T \int_{\mathcal{B}} \left[\frac{\partial \mathcal{L}}{\partial \varphi^i} - \frac{\partial}{\partial t}\left(\frac{\partial \mathcal{L}}{\partial \dot{\varphi}^i}\right) - \frac{\partial}{\partial X_j}\left(\frac{\partial \mathcal{L}}{\partial(\nabla_j \varphi^i)}\right)\right] \delta\varphi^i\, \mathrm{d}X\, \mathrm{d}t + \int_0^T \int_{\partial\mathcal{B}} \frac{\partial \mathcal{L}}{\partial(\nabla_j \varphi^i)} n_j \delta\varphi^i\, \mathrm{d}S\, \mathrm{d}t. \tag{A.6}$$

Since $\delta\varphi$ is otherwise arbitrary (except for the requirement that it vanish at $t = 0$ and $t = T$), the stationarity condition $\delta\mathcal{S} = 0$ implies that

$$\frac{\partial \mathcal{L}}{\partial \varphi^i} - \frac{\partial}{\partial t}\left(\frac{\partial \mathcal{L}}{\partial \dot{\varphi}^i}\right) - \frac{\partial}{\partial X_j}\left(\frac{\partial \mathcal{L}}{\partial (\nabla_j \varphi^i)}\right) = 0, \tag{A.7}$$

$$\frac{\partial \mathcal{L}}{\partial (\nabla_j \varphi^i)}\, n_j = 0 \quad \text{on } \partial\mathcal{B}. \tag{A.8}$$

Equations (A.7) and (A.8) are the standard **Euler-Lagrange equation** and its associated natural boundary condition. Further conditions, such as a specified boundary traction or pressure, would adjust the boundary term accordingly.

B

Jacobi's Formula for the Derivative of the Determinant

Jacobi's formula provides a way to compute the derivative of the determinant of a matrix $A(t)$ that depends on a parameter t. It states:

$$\frac{d}{dt}\det(A(t)) = \det(A(t))\,\mathrm{tr}\left(A(t)^{-1}\frac{dA(t)}{dt}\right) \tag{B.1}$$

Here, tr denotes the trace of a matrix, which is the sum of its diagonal elements. Now consider the matrix $A(t)$ as a perturbation of A:

$$A(t) = A + tE^{ij} \tag{B.2}$$

where E^{ij} is a matrix with a 1 in the (i, j) position and 0 elsewhere. This matrix E^{ij} represents a small perturbation to the (i, j) element of A.

The derivative of $A(t)$ with respect to t and evaluated at $t = 0$ is:

$$\left.\frac{dA(t)}{dt}\right|_{t=0} = E^{ij} \tag{B.3}$$

Applying Jacobi's formula, we get:

$$\left.\frac{d}{dt}\det(A(t))\right|_{t=0} = \det(A)\,\mathrm{tr}\left(A^{-1}E^{ij}\right) \tag{B.4}$$

The trace of the product $A^{-1}E^{ij}$ is:

$$\mathrm{tr}\left(A^{-1}E^{ij}\right) = (A^{-1})_{ji} \tag{B.5}$$

This is because E^{ij} has a 1 only at the (i, j) position, so when multiplying A^{-1} with E^{ij}, the only non-zero element of the resulting matrix will be at the (j, i) position, which is $(A^{-1})_{ji}$. The trace, which is the sum of diagonal elements, will then just be this single non-zero element.

$$\left.\frac{d}{dt}\det(A(t))\right|_{t=0} = \det(A)\,(A^{-1})_{ji} \tag{B.6}$$

Therefore, the partial derivative of the determinant of A with respect to its (i, j) element is:

$$\frac{\partial \det(A)}{\partial A_{ij}} = \det(A)\,(A^{-1})_{ji} \tag{B.7}$$